

LITHIUM DRIFTED P-I-N JUNCTIONS
IN SILICON

PARTICLE IDENTIFICATION AND IRRADIATION EFFECTS

C. A. J. AMMERLAAN

LITHIUM DRIFTED P-I-N JUNCTIONS IN SILICON

PARTICLE IDENTIFICATION AND IRRADIATION EFFECTS

LITHIUM DRIFTED P-I-N JUNCTIONS IN SILICON

PARTICLE IDENTIFICATION AND IRRADIATION EFFECTS

ACADEMISCH PROEFSCHRIFT

TER VERKRIJGING VAN DE GRAAD VAN DOCTOR
IN DE WISKUNDE EN NATUURWETENSCHAPPEN
AAN DE UNIVERSITEIT VAN AMSTERDAM,
OP GEZAG VAN DE RECTOR MAGNIFICUS MR. J. VAN DER HOEVEN,
HOGLERAAR IN DE FACULTEIT DER RECHTSGELEERDHEID,
IN HET OPENBAAR TE VERDEDIGEN IN DE AULA DER UNIVERSITEIT
(TIJDELIJK IN DE LUTHERSE KERK, INGANG SINGEL 411, HOEK SPUI)
OP WOENSDAG 8 NOVEMBER 1967,
DES NAMIDDAGS TE 4 UUR

DOOR

CORNELIS ANTONIUS JOSEPHUS AMMERLAAN
GEBOREN TE AMSTERDAM

1967

N.V. DIJKSTRA'S DRUKKERIJ V/H BOEKDRUKKERIJ GEBROEDERS HOITSEMA
GRONINGEN

PROMOTOR: PROF. DR. G. DE VRIES

Aan mijn vrouw
Aan mijn ouders

CONTENTS

| | |
|---|----|
| PREFACE | 1 |
| CHAPTER 1 PREPARATION OF P-I-N JUNCTIONS | 3 |
| 1.1 Introduction | 3 |
| 1.2 Dislocation density | 4 |
| 1.3 Hall effect | 5 |
| 1.4 Resistivity | 11 |
| 1.5 Infrared absorption | 14 |
| 1.6 p-n Junction characteristics. | 18 |
| 1.6.1 Sheet resistance. | 19 |
| 1.6.2 p-n Junction capacity | 19 |
| 1.6.3 Lithium drift. | 21 |
| 1.7 Lithium-impurity reactions. | 22 |
| 1.7.1 Pure crystals | 24 |
| 1.7.2 Crystals containing much oxygen | 25 |
| 1.7.3 Crystals containing some oxygen | 26 |
| 1.7.4 Crystals containing much boron. | 28 |
| 1.8 Preparation method | 30 |
| 1.8.1 Contact to the p-type region | 31 |
| 1.8.2 The n-type layer | 31 |
| 1.8.3 The lithium drift process. | 32 |
| CHAPTER 2 PARTICLE IDENTIFICATION BY PULSE SHAPE DISCRIMINATION. | 34 |
| 2.1 Introduction | 34 |
| 2.2 Pulse shape analysis. | 35 |
| 2.3 Particle identification method. | 40 |
| 2.4 Experimental arrangement | 43 |
| 2.4.1 Beam arrangement | 43 |
| 2.4.2 Detector properties | 44 |
| 2.4.3 Electronic equipment | 45 |

| | | |
|---|--|-----|
| 2.5 | Results. | 46 |
| 2.5.1 | Experimental results. | 46 |
| 2.5.2 | Calculated results | 48 |
| 2.6 | Discussion | 50 |
| 2.6.1 | Temperature of the detector | 50 |
| 2.6.2 | Comparison of experimental and calculated results. | 52 |
| 2.6.3 | Particle identification capabilities | 52 |
| 2.6.4 | Thicker detector | 53 |
| 2.6.5 | Radiation on the n-side | 53 |
| 2.6.6 | Pulse shaping by RC-networks | 54 |
| 2.6.7 | Two detector method | 55 |
| CHAPTER 3 IRRADIATION DAMAGE IN LITHIUM DOPED SILICON | | 56 |
| 3.1 | Introduction | 56 |
| 3.2 | Irradiations. | 60 |
| 3.2.1 | Gamma irradiation | 60 |
| 3.2.2 | Electron irradiation | 63 |
| 3.3 | Gamma irradiation damage in lithium drifted p-i-n junctions. | 64 |
| 3.3.1 | Junction capacity measurements. | 64 |
| 3.3.2 | Irradiation effect on junction capacity. | 66 |
| 3.3.3 | Time dependence of defect concentration. | 70 |
| 3.3.4 | Potential probe measurements | 75 |
| 3.3.5 | Particle detection by irradiated junctions | 77 |
| 3.4 | Gamma irradiation damage in isolated lithium drifted silicon | 81 |
| 3.4.1 | Method of measurement | 81 |
| 3.4.2 | Time dependence of conductivity | 84 |
| 3.4.3 | Temperature dependence of hole concentration | 85 |
| 3.5 | Electron irradiation damage in heavily lithium doped silicon | 94 |
| 3.5.1 | Sample preparation | 94 |
| 3.5.2 | Resistivity and Hall effect | 95 |
| 3.5.3 | Electron spin resonance | 98 |
| 3.6 | Discussion of the results | 98 |
| 3.6.1 | Time constant τ_{LIR} | 98 |
| 3.6.2 | Time constant τ_C | 101 |
| 3.6.3 | Recovery behaviour of irradiation effect | 105 |

| | | |
|-------------------------------|--|-----|
| 3.6.4 | Defect level at 0.23 eV. | 107 |
| 3.6.5 | Defect R. | 110 |
| 3.7 | Application to lithium drifted junction detectors . . | 112 |
| APPENDIX | Treatment of p-n junction with complementary error function impurity distribution | 116 |
| A.1 | p-n Junction capacity | 116 |
| A.2 | Lithium drift | 119 |
| SUMMARY. | | 121 |
| SAMENVATTING. | | 124 |
| REFERENCES | | 127 |
| SLOTWOORD - ACKNOWLEDGEMENTS. | | 129 |

PREFACE

In recent years semiconductor nuclear particle detectors have found wide application in experimental nuclear physics. An extensive research has been devoted to the development of these detectors after McKay had demonstrated, in 1949, the particle detection capabilities of reverse-biased semiconductor junctions. Up to the present, three distinct types of semiconductor detectors have been in use. Among these the surface barrier and the diffused p-n junction detectors are the oldest. In 1960 Pell proposed the lithium ion drift mechanism as a means of producing detectors with enlarged sensitive volume. Following this technique junctions are made, in which a lithium compensated intrinsic layer is intermediate between p- and n-type extrinsic regions. Actually, these p-i-n structure junctions were prepared in silicon and in germanium. Because of their extremely good energy resolution all of these junctions have excellent qualifications for nuclear particle spectrometry. The tiny and rigid solid state detectors compete with huge and expensive magnetic separators. The investigations to be described in this thesis are concerned with the latter p-i-n type junctions in silicon, nowadays frequently referred to as Si(Li) detectors. This work intends to be a contribution to the understanding of radiation induced phenomena in lithium doped silicon, with emphasis on the knowledge of the underlying solid state fundamentals.

Particle detection is enabled by the ionizing power of the incident radiation. Free carriers, electrons excited into conduction band states and holes in the valence band, are collected in the depleted volume of the junction, which operates as a solid state ionization chamber. Energy and range of an incident particle determine the height and shape of the pulse response of a reverse-biased p-i-n junction. Both the theoretical and experimental aspects of a particle identification system, based on suitable pulse treatments, are presented in chapter 2.

In addition to transient ionization effects, energetic radiation causes permanent damage in the crystal structure and deteriorates detector performance. Gamma ray damage displays many of the characteristics of irradiation effects in silicon in general. Such experiments, in which lithium drifted junctions are made of service as tools for the investigation of irradiation effects in lithium doped silicon, are discussed in chapter 3. Silicon, and in particular high resistivity intrinsic silicon, is a very vulnerable material for irradiation damage. Noticeable radiation induced property changes are therefore not only brought about in extreme circumstances as existing in space or near nuclear reactors, but also in more moderate radiation environments, in which these radiation detectors find their place. Lithium drifted p-i-n junctions show very interesting self-annealing features.

In the establishment of the final stable irradiation defects, interactions between imperfections, of either chemical or physical origin, play a dominant role. To understand their behaviour under irradiation, knowledge of the impurity content of the silicon crystals is a necessary requirement. In chapter 1 all experiments performed with the purpose of determining impurity concentrations are described. In conjunction therewith the method of preparation of p-i-n junctions is given.

Silicon crystals were obtained from a variety of suppliers, including Merck, Sharp and Dome (M), Wacker (W), Texas Instruments (TI) and MonoSilicon (MS). A particular sample is indicated by a symbol which for instance reads as TI, 2, 3; this designation identifies slice 3, taken from batch 2, supplied by Texas Instruments. Slices within one batch always showed very similar properties.

CHAPTER 1

PREPARATION OF P-I-N JUNCTIONS

1.1 Introduction

Starting point for the preparation of lithium drifted p-i-n junctions are slices of silicon, which have the following approximate properties. The diameter of the disc-shaped slices is between 15 and 27 mm, the thickness is about 2.5 mm, the circular shaped surfaces are plane and parallel. The slices are single crystals; a $\langle 111 \rangle$ crystal direction is normal to the surface. Most of the silicon is doped with the acceptor impurity boron and has a p-type resistivity between 8 and 100 Ωcm . Other impurities have been removed as much as possible; the number of dislocations per unit area is below 40 000 per cm^2 , the oxygen concentration is low, the minority carrier lifetime is at least 100 μs . The material is obtained from the supplier either directly in the form of slices or as a bar. From a bar slices are cut using a diamond saw, the slices are subsequently ground and polished. The silicon obtained from Texas Instruments Inc., sold under trademark "Lopex", is not zone refined.

The proper experimental techniques followed for the preparation of lithium drifted p-i-n junctions have been reported previously¹. No fundamental modifications have been adopted as the procedure still serves its purpose very well. For reasons of completeness the present preparation method is summarized in paragraph 1.8. As mentioned in the preface a good knowledge of the properties of the base material is required. In the first place this is desirable for a reliable production of high quality junction detectors. Secondly, for a quantitative interpretation of the irradiation induced phenomena this information is certainly needed. Therefore a number of investigations have been undertaken with the aim of gaining insight into the impurity content of the silicon. These measurements include determinations of the amount of dislocations, the boron, donor and oxygen concentrations and the driftability of the silicon. These measurements are described in the following paragraphs.

1.2 Dislocation density

The dislocation density, defined as the number of dislocation lines passing through a unit area, is measured by making counts of the etch pit density, EPD. This method of observing the dislocations is a reliable one since a one to one correspondence between etch pits and dislocation lines has been demonstrated by some independent techniques^{2,3}. In our experiments etching solutions according to DASH⁴ or SIRTLE⁵ were used. The EPD was determined by averaging the counts made on five different spots on each side of a slice. Etching the surface of a crystal may also reveal other structural imperfections, such as small angle misfits between adjacent parts of a crystal. Slices showing these gross types of defects were not used for any further work. Table I lists the results of EPD-values for material of future interest; figure 1 is an illustration of the results obtained.

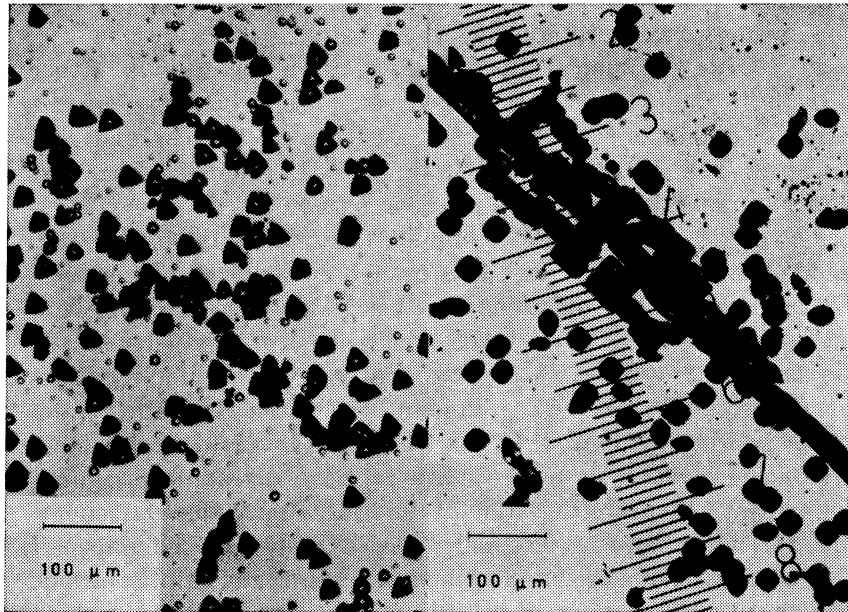


Fig. 1. Left: triangular etch pits on (111) plane, slice Wacker, 2, 6, Sirtle etch, EPD = 26 000 cm⁻². Right: square etch pits on (100) plane, batch Merck, 2, Dash etch, abandoned material.

TABLE I

Etch pit density (EPD) obtained by etch according to DASH ⁴⁾ or SIRTLE ⁵⁾ on different silicon slices.

| Batch | Etch | EPD |
|-------|--------|------------------|
| — | — | cm ⁻² |
| M, 7 | Dash | 34 000 |
| | Sirtle | 26 000 |
| TI, 1 | Sirtle | 500 |
| TI, 2 | Sirtle | 1 300 |
| W, 2 | Sirtle | 24 000 |
| MS, 1 | Sirtle | 100 |

1.3 Hall effect

For a determination of the concentrations of the electrically active impurities in the silicon the Hall effect was measured in a representative number of slices in a temperature range which extended from about 20 to 300 °K. For these measurements the method developed by VAN DER PAUW⁶ was adopted. This method requires no shaping of samples since our slices are already singly connected and homogeneous in thickness. The slices therefore remain available for subsequent experiments. Also in accordance with the prescriptions of the Van der Pauw method four small contacts were placed at the circumference of the samples. These contacts are made by evaporating four 1 mm wide strips of aluminium on the lateral faces of a sample. The aluminium is alloyed with the silicon during a 5 minutes 650 °C heat treatment, in this way providing non-rectifying low resistivity contacts. The contacts are spaced about the same distance apart around the circumference of a slice. Metal spring contacts to the alloyed spots suffice for further electrical connection of the sample. Corrections which are necessary because of the finite size of the contacts were applied, using the formula given by VAN DER PAUW⁶.

Figure 2 shows the main part of the measuring equipment. This sample holder could be inserted in a narrow dewar flask, in which liquid helium was pumped at the start of each series of measurements. The temperature may be raised above the helium temperature by two bifilar wound heaters. Two identical heaters, in a symmetrical position above and below the silicon slice, are con-

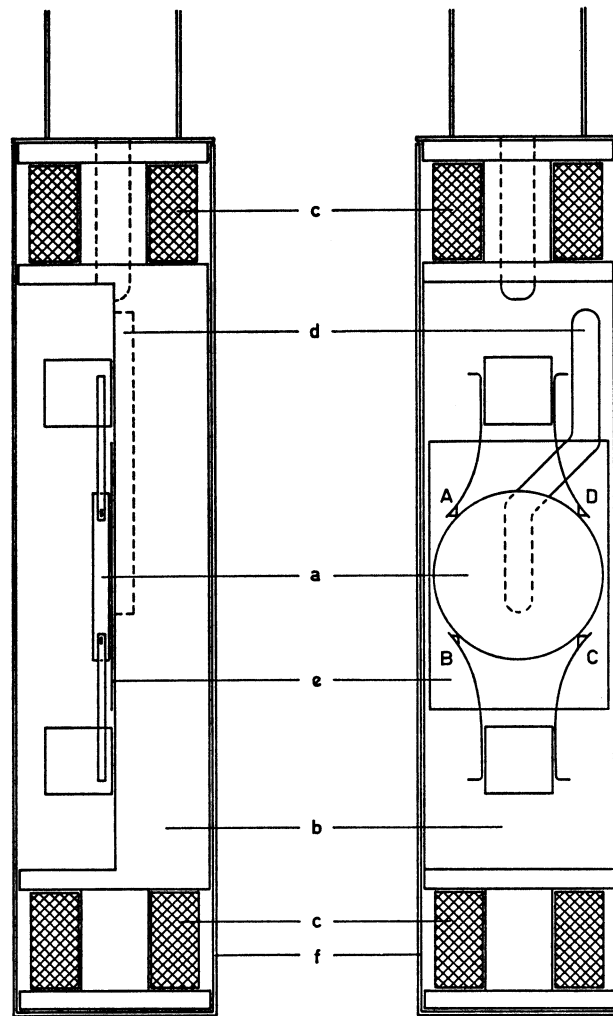


Fig. 2. Side view and view from above of the sample holder with mounted sample. Components: sample (a), contacts (A, B, C, D), copper block (b), heaters (c), thermocouple channel (d), insulating mica layer (e) and copper shield tube (f).

structured to minimize thermal gradients. Temperature differences are otherwise counteracted by the solid copper block, on which the slice is mounted in good thermal contact with it.

The Hall effect is measured with a stabilized direct current, always keeping the d.c. power dissipation in the sample below 1 mW.

An accurate digital voltmeter with high input impedance (Solartron) is used to measure the Hall voltage. The current is measured with the same instrument by the iR -drop produced across a standard resistor. The strength of the uniform magnetic field is determined with a rotating coil null-balance technique (Rawson Gaussmeter). Temperature measurements are performed using a Au+0.03 % Fe vs. Chromel thermocouple⁷ (Johnson-Matthey), calibrated at liquid nitrogen and liquid helium temperature. One junction of the thermocouple is in the near vicinity of the sample, the other junction is maintained at a temperature between 0.00 and 0.03 °C in a regulated Peltier cooled icebath (Kaye).

Spurious thermo-electric voltages and Ohmic voltages due to asymmetric placing of the contacts are eliminated by reversing both the direction of the current and the magnetic field. Besides this, the voltage and current contacts are interchanged for each measuring temperature. The Hall voltage is obtained as the average of these eight measured values.

Any measurement of the Hall effect is affected by the presence of a number of other transverse effects^{8,9} which add a contribution to the Hall voltage. A survey of the possible effects is presented schematically in figure 3. The diagram illustrates that an electric field (in the y -direction) is not only caused directly by a deflection of current carriers (in the x -direction) through a magnetic field (in

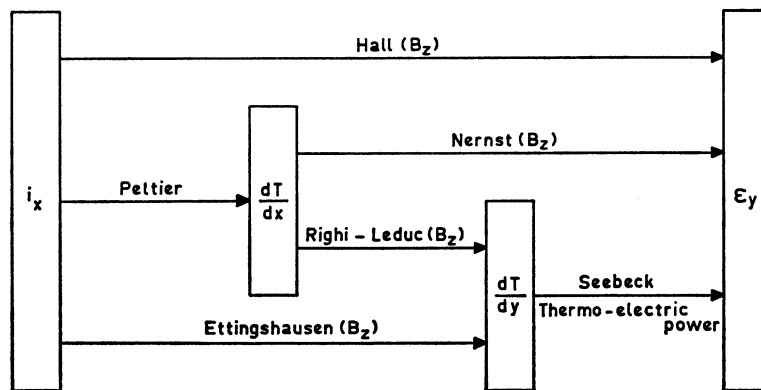


Fig. 3. Schematic representation of the Hall effect and related thermomagnetic phenomena. The effects for which a magnetic field is essential are followed by B_z in parenthesis. dT/dx represents a thermal gradient in the x -direction, dT/dy similarly in the y -direction.

the z -direction), which is the Hall effect, but also in consequence of the various thermomagnetic effects. They may be of importance since in general the thermo-electric power of semiconductors is high. Nevertheless calculations show that in our case their contribution to the Hall effect is negligibly small since the high lattice thermal conductivity of silicon restores isothermal conditions to a sufficient extent.

The hole concentration ϕ is obtained from the Hall effect using the next two equations for the Hall coefficient R_H :

$$R_H = \frac{dV_H}{iB},$$

$$R_H = \frac{r}{\phi e}.$$

The first of these equations expresses the Hall coefficient in terms of measurable quantities: V_H = Hall voltage, i = current, B = magnetic induction and d = thickness of the sample. The second equation contains the Hall factor r , the electron charge e and finally as the single unknown quantity, the hole concentration in the valence band ϕ . Of course, ϕ is obtained by equating the right hand sides of the two above equations.

The Hall factor, a quantity near unity, is given by the expression $r = \langle \tau^2 \rangle / \langle \tau \rangle^2$, where τ is the mean free time between two scattering events, and the averaging is over the various energy states of the holes. However, r may not be obtained from this expression with sufficient accuracy. From experiments it is known that for holes in 100 Ωcm silicon $r = 0.85 \pm 0.05$ at room temperature¹⁰. To account for the weak dependence of r on temperature we adopted the relationship r proportional to T^n . The value of n was chosen such that constant ϕ was obtained near room temperature. This fixed the value of n always near -0.2 , which is quite reasonable in this temperature region where lattice scattering is the most important. At lower temperatures, approximately below 100 $^\circ\text{K}$, the predominant scattering mechanism is less certain and a justified but accurate choice of r is hard to make. Fortunately at low temperatures ϕ decreases exponentially very rapidly making any slow variation of the Hall factor of less importance.

At room temperature the Hall voltage is measured for three

values of the current i , which differ by a factor 10. Also three values for the magnetic induction B are taken, the highest value being about 3 times the lowest one. In this way nine independent values for R_H are obtained, the difference between the extremes being less than 1 %. From these results it is concluded that the simple formula for R_H is applicable and that no terms in B^2 need to be considered.

The polarity of the Hall voltage is related to the conduction type of the specimen. In our case always p-type conduction was observed.

The numerical results of the Hall effect measurements, free hole concentration p versus absolute temperature T , are analysed using the following expressions derived in textbooks on semiconductors^{9, 8}:

$$p^2 + p(n_d + n'_a) - n'_a(n_a - n_d) = 0$$

$$n'_a = \frac{1}{2}n_v \exp\left(-\frac{E_a}{kT}\right)$$

$$n_v = 2\left(\frac{2\pi m_h kT}{h^2}\right)^{\frac{3}{2}}$$

In these formulae k is the Boltzmann constant, h the Planck constant; n'_a and n_v are abbreviations, of which n_v equals the density of electron states in the top of the valence band. Apart from these quantities the equations contain the parameters n_a = concentration of acceptor atoms, n_d = concentration of compensating donors, E_a = ionization energy of the relevant acceptor and m_h = density of states effective mass of holes, which may be calculated from the available experimental information. For this purpose the procedure described by VAN DAAL¹¹ was followed. The obtained results were then used as initial parameters for a least squares adjustment of a theoretical curve to the experimental points. These calculations were carried out using the X8 electronic computer of the "Mathematisch Centrum" in Amsterdam, for which a program in Algol 60 was written.

The parameters n_a , n_d , E_a and m_h , for which a best fit is obtained, are the final results of the analysis and are tabulated below. The values of n_a and n_d give the desired information about the purity of the silicon. The ionization energies as found by the experiments undoubtedly identify the acceptor with boron, for which a mean ionization energy $E_a = 0.045 \pm 0.001$ eV is reported in the literature,

markedly different from that for other acceptors considering the errors involved. The hole mass is in reasonable agreement with other reported values¹².

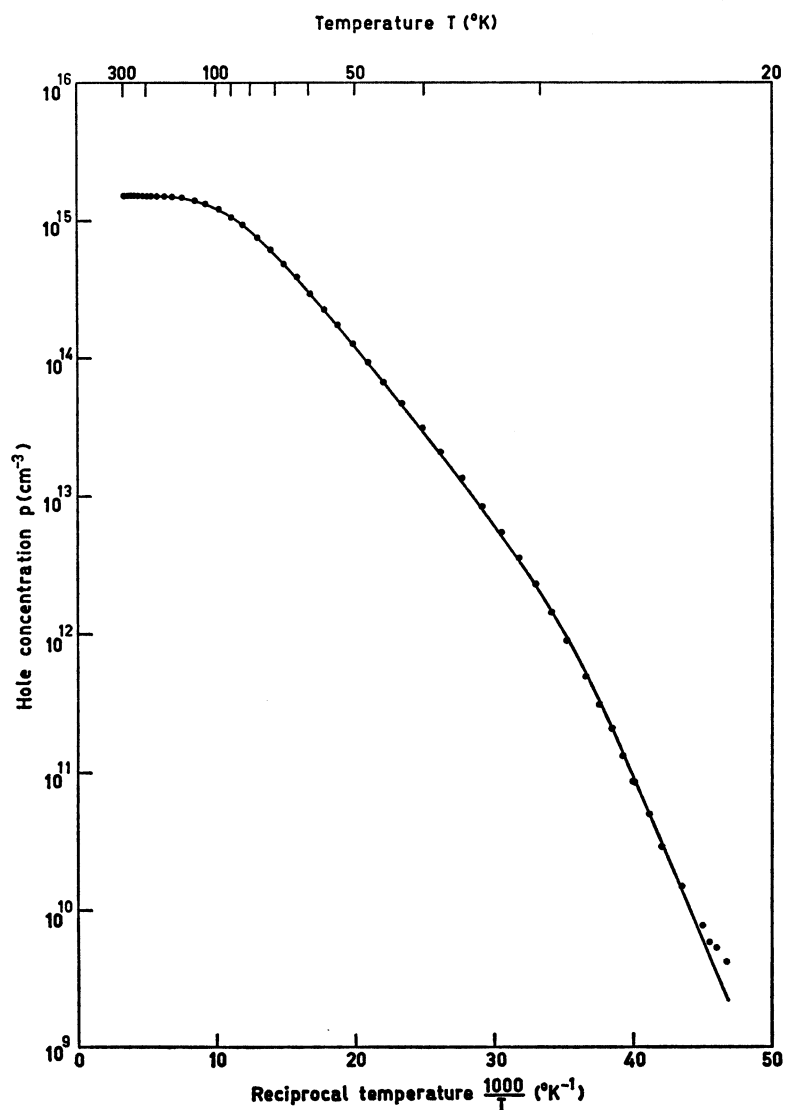


Fig. 4. Hole concentration as function of temperature obtained from the Hall effect for sample Wacker, 2, 5. Theoretical curve is adjusted to the experimental points (\bullet) by the least squares method.

In figure 4 a typical example is given of the experimental points, ρ versus $1/T$, and the fit obtained by the analysing procedure described above.

TABLE II

Concentration n_a of acceptors, concentration n_d of donors, degree of compensation n_d/n_a , electron energy level of the acceptor E_a and hole mass m_h relative to free electron mass m_e as determined for some samples by the temperature dependence of the Hall effect.

| Sample | n_a | n_d | n_d/n_a | E_a | m_h/m_e |
|-----------|---------------------------|---------------------------|-----------|-------|-----------|
| — | 10^{14} cm^{-3} | 10^{14} cm^{-3} | % | meV | — |
| M, 7, 3 | 1.62 | 0.23 | 14 | 38 | 0.33 |
| M, 7, 12 | 1.55 | 0.16 | 10 | 39 | 0.36 |
| TI, 1, 4 | 3.00 | 1.41 | 47 | 40 | 0.39 |
| TI, 1, 11 | 3.29 | 1.66 | 50 | 39 | 0.34 |
| TI, 2, 1 | 7.71 | 0.67 | 9 | 41 | 0.37 |
| W, 2, 3 | 17.6 | 0.02 | 0.1 | 44 | 0.49 |
| W, 2, 5 | 15.2 | 0.02 | 0.1 | 44 | 0.51 |

1.4 Resistivity

Some supplementary information concerning the donor and acceptor impurities in the silicon is obtained by combining measurements of the Hall effect and resistivity. For the resistivity measurements also a procedure suggested by the VAN DER PAUW⁶ theorem was adopted. Doing so, the same electrical contacts to the silicon slice and also identical other equipment, as described in the previous paragraph on the Hall effect, could be used. In the Van der Pauw method of measuring resistivity a current is passed through two adjacent contacts on the sample, for instance A and B (fig. 2), while the voltage developed across the other pair of contacts, C and D, is measured. The ratio of the voltage and current values defines a resistance V_{CD}/i_{AB} , which we call R_1 . Then an other pair of readings is taken with the current and voltage contacts all shifted in the same sense to the next contact. This measurement fixes a second resistance R_2 , for example $R_2 = V_{DA}/i_{BC}$. If in the silicon sample the conduction is the same everywhere, then the ratio R_1/R_2 is a geometrical constant. In our case the slices are nearly circular shaped and the contacts are placed around the circumference with nearly 4-fold symmetry, as viewed from the middle of

the slice. Therefore R_1 approximately equals R_2 , the difference never exceeding 3 %. For this case the expression for the resistivity ρ , given by Van der Pauw, simplifies to:

$$\rho = \frac{\pi d (R_1 + R_2)}{2 \ln 2}.$$

In our measuring procedure the current was commuted for each measurement. This not only eliminates spurious thermo-electric voltages, but also shows up any unwanted rectifying property of the metal-semiconductor contacts. Also all allowed permutations of the current and voltage contacts were taken in each measurement. Again, the proper result is obtained by averaging the eight measured values. As for the Hall coefficient, the resistivity also proved to be independent of the measuring current.

As mentioned above in a uniformly doped sample the ratio R_1/R_2 is geometrically determined, constant with respect to the temperature. In a sample however, in which the distribution of impurities is inhomogeneous, the conduction in different parts of the sample will vary with temperature in a different way. This means that the current pattern in the sample will vary with the temperature, yielding a non-constant R_1 to R_2 ratio. The constancy of this ratio as function of the temperature therefore is a measure of the macroscopic uniformity of the impurity distribution. In our samples R_1/R_2 varied less than 3 % over the temperature range 20–300 °K. Unfortunately this result is hard to interpret in terms of impurity distribution, but comparison with other investigations shows that this variation is favourably small.

More quantitative information is obtained by combining the results of the Hall effect and resistivity measurements. This is done in the usual way by computing the Hall mobility μ_H as the product of the Hall coefficient R_H and the conductivity σ :

$$\mu_H = R_H \sigma = r \mu_c,$$

since

$$\sigma = p e \mu_c.$$

It is seen that apart from the Hall factor r , already discussed, the Hall mobility equals the conductivity mobility μ_c . At high temperatures the hole mobility is determined by lattice scattering and its value is known from literature. Taking the modern value

$\mu_c = 475 \text{ cm}^2/\text{Vs}$ (at 20°C) and as before $r = 0.85$ (20°C), a Hall mobility $\mu_H = 404 \text{ cm}^2/\text{Vs}$ is calculated which is in good agreement with measured values. In other words, for the chosen values of μ_c and r , the hole concentration p obtained from the Hall effect equals p obtained from the conductivity. Since the observed mobility is typically that for holes, which differs greatly from the electron mobility, the results in this way again indicate that the investigated silicon has p-type conductivity.

For low temperatures the electron scattering by phonons is less, and the scattering by impurities becomes the predominant one. From the analysis of the Hall effect measurements (Table II) the donor and acceptor concentrations are already known. These values may be substituted in the BROOKS-HERRING¹³ equations to calculate the ionized impurity scattering. Neutral point defect scattering is taken into account with aid of the theory derived by ERGINSOY¹⁴. As is shown in figure 5 the agreement between calculated and experimentally determined mobility at low temperatures is within 50 %. The above description indicates how the presence of impurities is detected by their influence on the hole mobility. The errors involved in theory and experiment render it is impossible to obtain very accurate results by this method.

In table III the results are given for the resistivity of some samples; the net acceptor concentration $n_a - n_d$ derived from it using $\mu_c = 475 \text{ cm}^2/\text{Vs}$ and the observed Hall mobility at room temperature.

TABLE III

Results of the resistivity measurements; resistivity ρ , net acceptor concentration $n_a - n_d$ and hole Hall mobility at room temperature μ_H (293 °K).

| Sample | ρ | $n_a - n_d$ | μ_H (293 °K) |
|-----------|-------------------|---------------------------|-------------------------|
| — | Ωcm | 10^{14} cm^{-3} | cm^2/Vs |
| M, 7, 12 | 94.6 | 1.39 | 395 |
| M, 7, 13 | 96.2 | 1.37 | 398 |
| M, 7, 14 | 94.6 | 1.39 | 398 |
| TI, 1, 4 | 84.3 | 1.56 | 404 |
| TI, 1, 11 | 83.3 | 1.58 | 395 |
| TI, 2, 1 | 19.9 | 6.60 | 393 |
| TI, 2, 6 | 20.0 | 6.57 | 392 |
| W, 2, 3 | 7.94 | 16.6 | 385 |
| W, 2, 5 | 9.16 | 14.3 | 386 |

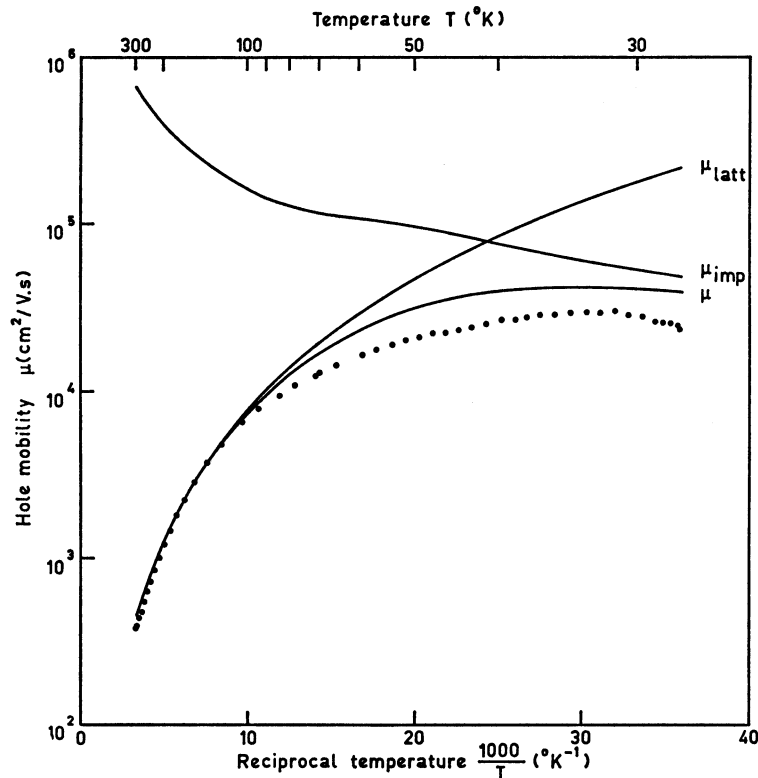


Fig. 5. Hall mobility as function of temperature for sample Texas Instruments, 1, 11. Curve labelled μ is calculated by adding lattice and impurity scattering. Experimental points: \bullet .

1.5 Infrared absorption

Another impurity, often present in silicon, is oxygen. This impurity escapes from a determination by the Hall effect and resistivity measurements, because it shows neither donor nor acceptor action. Oxygen in silicon may however be observed by its influence on the infrared transmission absorption spectrum¹⁵.

Oxygen is normally incorporated in the silicon lattice in the interstitial position which is illustrated in figure 6. A bond between two adjacent silicon atoms is broken and two new covalent Si-O bonds are formed. The interstitial site of an oxygen atom is in the perpendicular bisector plane of the two neighbouring silicon atoms, approximately 0.5×10^{-8} cm besides the axis joining them. For a

non-linear three-atomic molecule three normal modes of vibration are easily derived. Considering as a first approximation the Si-O-Si molecule formed by the oxygen atom and its two nearest neighbours as isolated from its environment, also three vibrational modes of corresponding symmetry type are expected. Since these are all optically active three fundamental frequencies are expected in the

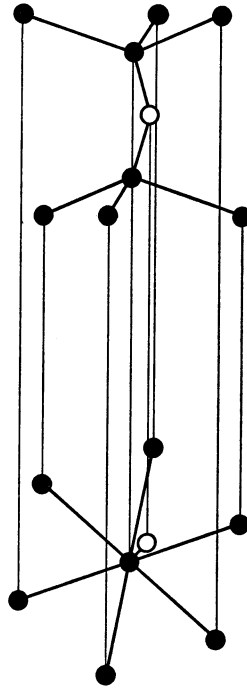


Fig. 6. Configuration of an oxygen atom (○) in a silicon (●) lattice. Nearest and second neighbours are shown projected on two mutually perpendicular planes.

infrared absorption spectrum and are indeed observed. Of them, the strongest absorption is caused by the asymmetric stretching vibration ν_3 at a wavelength of approximately $9 \mu\text{m}$, wavenumber $\sigma \approx 1100 \text{ cm}^{-1}$. At room temperature the absorption at frequency ν_3 due to oxygen is a broad peak superimposed upon another broad peak arising from excitation of a lattice vibration. On cooling the lattice absorption background decreases, as illustrated in figure 7. Also, as may be seen in figure 7, the oxygen absorption peak narrows

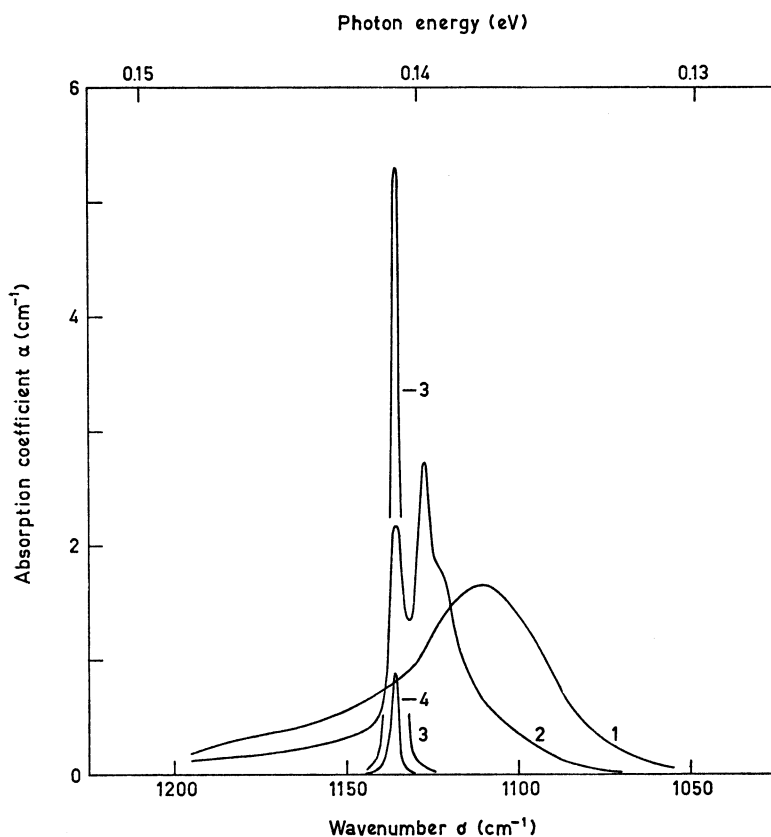


Fig. 7. Absorption spectrum of the vibrational mode ν_3 of oxygen in silicon. Curves 1, 2 and 3 are observed at 293, 77 and 4 °K respectively in quartz crucible grown sample Philips, 1,1, containing 3.2×10^{17} oxygen atoms per cm^3 . Curve 4 is measured at 4 °K on "Lopex" sample Texas Instruments, 2, 5 contaminated with about 6×10^{16} oxygen atoms per cm^3 .

and increases in height, it shifts in frequency towards higher σ and structure appears in it. This behaviour is largely explained by considering also the interaction with the six next-nearest neighbours of the oxygen atom. In this additional field of point group $\bar{3}$ (S_6) symmetry the oxygen oscillates about a particular equilibrium position. The sixfold degeneracy of the vibrational states is lifted by the tunneling motion between adjacent minima through the barrier opposing rotation. It seems likely that the observed struc-

ture arises from combination bands involving a normal mode of the Si-O-Si molecule and the ground state energy levels of the tunneling motion^{16,17}.

Using the infrared absorption for determinations of the oxygen concentration it is obvious that in order to obtain the highest sensitivity the measurements should be carried out at low temperature. In a room temperature measurement it is difficult to separate the oxygen absorption from the underlying lattice background, whereas for liquid nitrogen and liquid helium measurements this subtraction is much more easily made. The intensity of the absorption, calculated by taking $(\alpha_{\max} - \alpha_{\text{background}})$ times half-width is assumed to be proportional with the oxygen concentration. For calibration at room temperature an absorption coefficient of 1 cm^{-1} corresponding to an oxygen concentration $n_0 = 3 \times 10^{17} \text{ cm}^{-3}$ was used after KAISER¹⁸. A limit of detectability at liquid helium temperature of 10^{15} atoms oxygen per cm^3 seems to be reasonable.

Infrared absorption measurements were carried out in a low temperature optical cell. Room temperature measurements were made using a single beam (Grubb Parsons) spectrometer; more recent experiments at liquid nitrogen and liquid helium temperature were performed with a double-pass (Beckmann IR 7) spectrometer. The slices used for this work obtained optical polish on both plane parallel surfaces. Corrections for multiple internal reflections were applied if necessary. In the float-zoned silicon crystals no oxygen is detectable; the few results, which nevertheless have decisive significance, are given in table IV.

TABLE IV

Concentration of oxygen n_0 in some silicon samples as determined at liquid helium temperature by the infrared absorption of the asymmetric stretching vibration ν_3 at 1136 cm^{-1} .

| Batch | Sample | n_0 |
|-------|----------|---------------------------|
| — | — | 10^{14} cm^{-3} |
| M7 | | < 10 |
| W2 | | < 10 |
| | TI, 1, 5 | 70 |
| | TI, 1, 7 | 80 |
| | TI, 2, 5 | 620 |

1.6 p-n Junction characteristics

As an intermediate stage in the preparation of lithium drifted p-i-n junctions, fully dealt with in paragraph 1.8, a p-n junction is at one's disposal. Valuable information is obtained by measuring the lithium ion drift rate in the reverse-biased p-n junction. This information not only concerns the impurities present in the silicon, but also the time constant with which the completed p-i-n junction recovers after being damaged by an irradiation. In this paragraph, in the next one, and on a mathematically more thorough basis in the Appendix, we discuss the results obtained by carrying out these measurements.

A p-n junction is formed in the originally uniformly doped p-type slices by diffusing lithium into one side of the slices for some well defined time at constant temperature from an "infinite" source. During the diffusion time the lithium concentration at the surface of the slice, $n_{\text{Li}}(0)$, is constant and equal to the solubility of lithium in silicon, as determined by the temperature and external phase. Under these diffusion conditions the lithium concentration profile is given by

$$n_{\text{Li}}(x) = n_{\text{Li}}(0) \operatorname{erfc} \frac{x}{2(D_{\text{Li}}t)^{\frac{1}{2}}},$$

where erfc is an abbreviation for complementary error function, D_{Li} is the diffusion constant of lithium ions in silicon, t is diffusion time, and x is position in the slice relative to the surface $x = 0$, where the diffusion started. At some position c the lithium concentration has dropped to a value $n_{\text{Li}}(c)$ which is equal to the net acceptor concentration $n_{\text{a}} - n_{\text{d}}$ of the original silicon, known from the Hall effect and resistivity measurements (1.3 and 1.4). The value of c marks the depth of the p-n junction below the diffused surface, or, in other words the thickness of the n-type counterdoped region. The depth c is obtained by solving the equation:

$$n_{\text{a}} - n_{\text{d}} = n_{\text{Li}}(c) = n_{\text{Li}}(0) \operatorname{erfc} \frac{c}{2(D_{\text{Li}}t)^{\frac{1}{2}}}.$$

In all our experimental work we adopted the following standard conditions for the diffusion process: diffusion time $t = 300$ s, diffusion temperature 450 °C; consequently: diffusion constant

$D_{\text{Li}} = 6.8 \times 10^{-8} \text{ cm}^2/\text{s}$ and solubility $n_{\text{Li}}(0) = 2 \times 10^{18} \text{ cm}^{-3}$. As a result a p-n junction depth of 200 to 250 μm , depending on the resistivity of the silicon, is obtained.

1.6.1 Sheet resistance

As a first check on the diffusion procedure the sheet resistance of the n-type layer is determined using a four-point probe technique. Our measuring unit (Fell) consists of four collinear probes equally spaced exactly 1 mm apart. While pressing the probes firmly on the n-type side of the slice a current i is passed through the two outer pins. Then the voltage developed across the two inner pins is read. From these measurements the sheet resistance is calculated as:

$$R_s = \frac{\pi V}{\ln 2 i}.$$

Corrections have to be applied to the calculated value if the measurements are not taken in the centre of the slice¹⁹, or else if the diameter of the slice is not much larger than the distance between probes²⁰. In our case no correction for the finite thickness of the n-type region is necessary²⁰. The sheet resistance of the n-layer may not only be measured by the above-mentioned technique, but also be calculated from the diffusion parameters²¹. Since each lithium atom contributes one electron to the conduction process the surface resistance is wholly determined by the known total amount of introduced lithium atoms. For our standard diffusion conditions a sheet resistance of 2.1 Ohm is calculated. This value is always reproduced within 15 % by the four-point probe measurements.

1.6.2 p-n Junction capacity

A second check on the p-n junction, formed by the lithium diffusion, is provided by the capacity-voltage curve of the reverse-biased junction. We first derive an expression relating capacity and reverse voltage. Following PELL²² a power series expansion of the lithium concentration $n_{\text{Li}}(x)$ is made around the point $x = c$. Neglecting second and higher order terms, thereby restricting ourselves to thin junctions, the result is

$$n_{\text{Li}}(x) = n_{\text{Li}}(c) \left(1 - \frac{x-c}{L} \right),$$

in which the quantity L , of dimension length, is introduced by $L = 2D_{\text{Li}}t/c$. The assumption is moreover made that $c \gg (D_{\text{Li}}t)^{\frac{1}{2}}$. Subtracting the constant amount $n_{\text{a}} - n_{\text{d}} = n_{\text{Li}}(c)$ of negatively charged acceptors the space charge ρ around $x = c$ is given by

$$\rho = -en_{\text{Li}}(c) \frac{x-c}{L}.$$

Substitution into the Poisson equation yields:

$$\frac{d^2\varphi}{dx^2} = -\frac{dE}{dx} = \frac{en_{\text{Li}}(c)(x-c)}{\varepsilon L},$$

where φ is potential, E is electric field and $\varepsilon = \varepsilon_0\varepsilon_r$ is dielectric constant. Integrating this equation two times, subject to the condition that the electric field is zero at the boundaries of the junction, results in the following relationship between depleted junction width W and voltage V :

$$W = \left(\frac{12 \varepsilon L V}{en_{\text{Li}}(c)} \right)^{\frac{1}{3}}.$$

The capacity C of a reverse-biased junction of area A , defined by and measured as $C = dQ/dV$, is closely related to the junction width, since $C = \varepsilon A/W$. Therefore our final result reads:

$$C = A \left(\frac{en_{\text{Li}}(c)\varepsilon^2}{12 LV} \right)^{\frac{1}{3}}.$$

A plot of $\log C$ versus $\log V$ gives a straight line of slope $-\frac{1}{3}$; from its position L is easily determined. Some remarks concerning the validity of the results are however to be made.

Comment 1. Already before the capacity measurements are performed some drift motion may have occurred in the junction. This drift is due to the electric field of the built-in diffusion potential, which develops, in the cooling stage after diffusion, as soon as the material becomes extrinsic. The effect is especially important for the lower-resistivity silicon which becomes extrinsic at higher temperature where the lithium mobility is still large. As a consequence the impurity distribution in the middle of the junction is affected by the ion drift and deviates from the assumed linear dependence. In particular for low reverse voltage the junction width is substantially

increased, the capacity is decreased. Measurements of the lithium ion drift rate in such junctions yield erroneous results. This undesired effect is remedied as much as possible by rapid quenching of the samples after diffusion.

Comment 2. For high values of the reverse bias the linear junction approximation is invalid, since W is no longer small compared to L . In practice W may be even a few times larger than L . This leaves us with the unpleasant situation that our capacity formula may not be applicable both for high and for low V . Therefore exact calculations have been made for the complementary error function distribution. This lifts the restrictions for the high bias region. Since the formulae for the complementary error function distribution are rather lengthy, they are presented separately in the Appendix.

Comment 3. Even in the limit $W \rightarrow 0$, or $V \rightarrow 0$, where the series expansion of the complementary error function is allowed, the above-mentioned formulae after Pell do not give an exactly true result. Responsible for this disagreement is the assumption $c \gg (D_{Li}t)^{\frac{1}{2}}$, which in reality is not fully obeyed. In the Appendix it is shown that this is an unnecessary assumption, which may be removed by replacing L by a slightly modified characteristic length L^* . Calculation of L^* requires no more information about the junction, hardly more work is needed for it, and it makes the formulae exactly valid in the low bias limit.

At this stage it is possible to compare the measured capacity curve with the calculated one. The predicted $V^{-\frac{1}{2}}$ dependence is always found at least for intermediate values of the reverse bias. Also absolute agreement between measured and calculated capacity is always within 10 %. Experimental details concerning the measurements of junction capacity are given in section 3.3.1.

1.6.3 Lithium drift

Having established a thorough knowledge of the parameters characterizing the p-n junction, we may now proceed to describe the process of ion drift in the reverse-biased junction. Application of a reverse bias across the junction sets up an electric field in the depleted region. The force exerted by this electric field on the rather mobile lithium ions causes them to drift in the p-type direction. This results in space charge compensation and increase in junction

width. Experimentally this may be monitored by watching the decrease of junction capacitance as function of time. A more detailed description of the lithium ion drift mechanism, introduced by Pell, is found in several papers^{22, 23, 24}.

Again based on the linear junction approximation Pell showed that the following expression for the initial rate of capacity variation holds:

$$\left(\frac{d \ln C}{dt}\right)_{t=0} = -\frac{n_{\text{Li}}(c)e\mu_{\text{Li}}}{3 \varepsilon}.$$

We prefer to write this as:

$$\left(\frac{d \ln C}{dt}\right)_{t=0} = -\frac{1}{3 \tau_{\text{C}}},$$

by introducing the ionic relaxation time τ_{C} , given by:

$$\tau_{\text{C}} = \frac{\varepsilon}{n_{\text{Li}}(c)e\mu_{\text{Li}}}.$$

It is clear that a measurement of the decrease of the junction capacity as function of time, enables us to determine the ionic relaxation time τ_{C} . Since $n_{\text{Li}}(c)$ is known (paragraphs 1.3 and 1.4), also μ_{Li} , the mobility of lithium ions in a silicon lattice, may be calculated. By making use of the Einstein relation $eD_{\text{Li}} = \mu_{\text{Li}} kT$ the diffusion constant D_{Li} is then also known.

In the Appendix the modifications of the above formula, properly taking account of the complementary error function distribution, are discussed.

1.7 Lithium-impurity reactions

In this paragraph we continue the discussion about the use of the lithium ion drift process to obtain information on some impurities possibly present in the silicon crystals. With the relationships established in the previous paragraph or in the Appendix, we are able to derive the lithium ion mobility from a measurement of the decrease of capacity of a reverse-biased p-n junction. The lithium ion drift rate will be slowed down if impurities are present which interact with the lithium ions. For example all our samples are doped with the acceptor impurity boron. The positively charged lithium

ion may be captured by a negative boron ion in the reaction $\text{Li}^+ + \text{B}^- \rightleftharpoons \text{LiB}$. A relatively stable and immobile ion pair is formed. As an other example the lithium ions may be trapped by oxygen impurities: $\text{Li}^+ + \text{O} \rightleftharpoons \text{LiO}^+$. Also in this way the lithium ion is bound into an immobile complex defect. Carrying out lithium ion drift in a sample where such impurity pair formation has occurred results in a reduced drift rate. Only the fraction α of unpaired lithium ions is able to migrate in the electric field of the junction region. In the following cases we restrict our considerations to the impurities boron and oxygen. These are the only two which are likely to be present in the silicon in sufficient concentration, and both of them interact with the lithium ions via the above-mentioned reactions. A measurement of α provides a sensitive method of determining the presence of these impurities, that is very small amounts of them are detectable. The information is however not specific as regards the identity of the impurity.

The formula which relates the capacity variation of the junction with the lithium ion mobility is strictly valid only at time zero. Continuing ion drift at a constant junction bias for some time leads to a slower capacity decrease per unit time. On a merely experimental basis we found that an improved linear dependence upon time is obtained by considering $1/C^2$. Plotting $1/C^2$ as function of time, the experimental points fall along a straight line within experimental error for some prolonged initial length of time. The positive slope of this line determines the lithium ion mobility. The initial period extends from time zero to about $0.3 \tau_c$, where τ_c is the ionic relaxation time introduced in the previous paragraph. In other words, in the initial time period the capacity decreases from the p-n junction value at time zero $C(0)$ to about $0.9 C(0)$. To increase the amount of data obtainable from the ion drift measurements the allowed range of 10 % capacity variation is split into five parts. In each of these parts the capacity is allowed to decrease by 2 %. In this way it is possible to measure the lithium ion mobility in a number of circumstances. For instance the lithium mobility may be determined at five different temperatures. Alternatively the drift rate may be studied as function of time for constant temperature in cases where time dependence due to ion pairing is noticeable. In each of the 2 % parts ten or more capacity measurements are made. As a consequence the difference between two successive readings

amounts to only 0.2 %. In the original p-n junction the capacity is inversely proportional to the cube root of the junction bias. During the whole drift procedure this voltage dependence is not appreciably altered. Therefore, to prevent capacity changes due to reverse bias changes, the latter is kept constant within 0.05 %, monitored by a suitable voltmeter (DM 2006, Solartron). Also the temperature of the junction is maintained accurately at the chosen value, never deviating more than 0.5 °C from it. Straight lines given by $C(t)^{-2} = a_i t + b_i$, $i = 1, \dots, 5$, are adjusted to the values C^{-2} obtained from the measurements by least squares fitting. By this procedure a_i and b_i are fixed. The ionic relaxation time τ_c is then calculated from:

$$\tau_{c,i} = \frac{2P}{3a_i C(0)^2},$$

where $C(0)$ is the capacity of the undrifted p-n junction, also equal to the constant b_1 in the straight line equation adjusted to the first 2 % capacity variation, and P is the drift rate factor derived in the Appendix.

As regards the results obtained by the lithium ion drift measurements it is useful to distinguish between four cases, which we now proceed to do.

1.7.1 *Pure crystals*

Only small amounts of the impurities boron and oxygen are present in the silicon crystals. Therefore no interactions of the $\text{Li}^+\text{-O}$ or $\text{Li}^+\text{-B}^-$ type need to be considered and all the lithium ions are free to take part in the drift motion. Measurements are performed at five different temperatures, usually in this case at -10 , 0 , $+10$, $+20$ and $+30$ °C. Using the formula given above the ionic relaxation time is computed. This relaxation time is also calculated from its defining equation given in section 1.6.3. From the Hall effect and resistivity measurements the lithium concentration $n_{\text{Li}}(c)$ is known, the lithium mobility μ_{Li} is taken from PELL^{26,27}; in all calculations we substituted $\epsilon_r = 11.8$ for the relative permittivity. Division of the two results yields the fraction α of unpaired lithium ions, in the case of pure crystals considered here near unity. From the mobility the diffusion constant D_{Li} is calculated by use of the

Einstein relation. Adjustment of the results to the theoretical expression $D_{\text{Li}}(T) = D_0 \exp(-E_A/kT)$ by a least squares method yields the constants D_0 and E_A .

Slices taken from the batches Merck, 7 and Wacker, 1 belong to this category of pure crystals, although in these 100 Ωcm samples some $\text{Li}^+\text{-B}^-$ ion pairing is still observable. Results obtained on these materials are listed in table V.

TABLE V
Lithium ion drift results for some pure silicon crystals.

| Sample Merck, 7, 12 | | | | Sample Wacker, 1, 2 | | | |
|---|----------------------|----------------------|----------|---|----------------------|----------------------|----------|
| temp | τ_{meas} | τ_{calc} | α | temp | τ_{meas} | τ_{calc} | α |
| $^{\circ}\text{C}$ | hour | hour | — | $^{\circ}\text{C}$ | hour | hour | — |
| -10 | 501 | 401 | 0.80 | -10 | 432 | 372 | 0.86 |
| 0 | 186 | 144 | 0.78 | 0 | 165 | 134 | 0.81 |
| +10 | 74 | 56 | 0.76 | +10 | 63 | 52 | 0.83 |
| +20 | 30.4 | 23.2 | 0.76 | +20 | 27.0 | 21.5 | 0.80 |
| +30 | 12.2 | 10.2 | 0.84 | +30 | 11.2 | 9.5 | 0.84 |
| $D_0 = 2.18 \times 10^{-3} \text{ cm}^2/\text{s}$ | | | | $D_0 = 1.84 \times 10^{-3} \text{ cm}^2/\text{s}$ | | | |
| $E_A = 0.66 \text{ eV}$ | | | | $E_A = 0.65 \text{ eV}$ | | | |
| R.M.S.-error = 3.6 % | | | | R.M.S.-error = 0.9 % | | | |

1.7.2 Crystals containing much oxygen

The crystals contain no appreciable amount of boron, but are rather strongly contaminated with oxygen. This situation holds for slices from Texas Instruments, batch 2. Oxygen was detectable in these crystals by the associated infrared absorption at wavelength 9 μm as described in paragraph 1.5 and was found to be present in a concentration near 6×10^{16} atoms per cm^3 (Table IV). This amount is so large that the time constant to reach equilibrium in the reaction $\text{Li}^+ + \text{O} \rightleftharpoons \text{LiO}^+$ is small compared to the time of the measurements. Again therefore the ion drift measurements are done at some different temperatures in each of which a drift rate corresponding to equilibrium conditions is found. In table VI the fraction of unpaired lithium ions derived from these measurements (α_{meas}) is given at the relevant temperature. A reaction constant K is defined by $K = n_{\text{Li}^+} n_{\text{O}} / n_{\text{LiO}^+}$, where equilibrium concentrations are to be substituted. Using for this reaction constant the values obtained by PELL²⁸

the amount of oxygen is calculated from the observed α_{meas} . The average of these results is taken as the most probable value for the concentration of oxygen and is given in the table. Working back from this oxygen concentration α is calculated (α_{calc}) and compares then quite nicely with the observed values.

TABLE VI
Lithium ion drift results for crystals containing much oxygen.

| Sample Texas Instruments, 2, 1 | | | Sample Texas Instruments, 2, 6 | | |
|--|------------------------|------------------------|--|------------------------|------------------------|
| temp | α_{meas} | α_{calc} | temp | α_{meas} | α_{calc} |
| °C | — | — | °C | — | — |
| +10 | 0.013 | 0.014 | +10 | 0.017 | 0.016 |
| +20 | 0.029 | 0.026 | +20 | 0.032 | 0.029 |
| +30 | 0.042 | 0.044 | +30 | 0.047 | 0.050 |
| | | | +40 | 0.081 | 0.080 |
| | | | +50 | 0.123 | 0.123 |
| | | | +60 | 0.171 | 0.180 |
| $n_0 = 480 \times 10^{14} \text{ cm}^{-3}$ | | | $n_0 = 420 \times 10^{14} \text{ cm}^{-3}$ | | |

1.7.3 Crystals containing some oxygen

Again the concentration of boron is assumed to be so low that no interactions involving boron are of importance. Oxygen is however present in the silicon but in such a small amount that this case is intermediate between the cases 1.7.1 and 1.7.2 considered before. The time constant for reaching equilibrium in the LiO^+ -complex forming reaction is now comparable to the time needed to perform a lithium ion drift experiment. This situation is believed to hold for Texas Instruments, batch 1, crystals.

To exploit the specific possibilities offered by this situation the following measuring procedure was adopted. Before starting the measurements the junction was kept for a sufficient time at $T_1 = 20^\circ\text{C}$ to allow the defect interactions to equilibrate at this temperature. Then the first drift rate measurement was performed yielding a result proportional to $\alpha(20^\circ\text{C})\mu_{\text{Li}}(20^\circ\text{C})$. Following this the temperature of the junction is suddenly raised to $T_e = 40^\circ\text{C}$. After having stabilized this new temperature the capacity measurements are immediately continued. Initially the drift rate is proportional to $\alpha(20^\circ\text{C})\mu_{\text{Li}}(40^\circ\text{C})$ but gradually it increases as more

lithium becomes unpaired at higher temperature. Finally the drift rate is determined by $\alpha(40^\circ\text{C})\mu_{\text{Li}}(40^\circ\text{C})$. The time to reach these equilibrium conditions is somewhat smaller than the time still available to cover the remaining allowed 8 % capacity variation. From the first drift rate measurement and the final slope of the second series the fraction of unpaired lithium ions in equilibrium at respectively 20 °C and 40 °C is known. In the same way as described in case 1.7.2 the oxygen concentration is calculated from these data.

The first part of the second series of measurements demonstrates the variation of α with time at 40 °C and determines the time constant τ_{LiO^+} involved in the LiO^+ -formation. A theoretical expression for this time constant reads as²⁹:

$$\tau_{\text{LiO}^+} = \frac{1}{4\pi\{(n_{\text{Li}} + n_0 + K)^2 - 4n_{\text{Li}}n_0\}^{\frac{1}{2}} D_{\text{Li}} R}$$

In this expression n_{Li} is the total concentration of lithium ions, either present as Li^+ itself or as LiO^+ . The oxygen concentration n_0 is also known as explained above. In case 2 of this paragraph the reaction constant K was already introduced. D_{Li} , the diffusion constant for lithium ions in a silicon lattice, was the result of the measurements discussed as case 1. Therefore R , the capture radius within which a diffusing lithium ion is trapped by an oxygen atom, may be calculated. Two experiments of this kind were performed in junctions with different value of reverse bias V . In two other experiments the LiO^+ -pairs were nearly completely dissociated during some minutes at $T_1 = 80^\circ\text{C}$, whereafter the return to equilibrium at lower temperature was studied. They all yield as result a capture radius of more than 10×10^{-8} cm. For a capture process lacking the long range attracting forces of electrostatic nature this is a surprisingly large value. In our view it is however reasonable to assume that the higher values for the oxygen concentration as determined by infrared absorption (table IV) are correct. Substituting these concentrations into the formula for τ_{LiO^+} reduces all results for the capture radius to the more probable value of about 5×10^{-8} cm. The discrepancy in the determination of oxygen concentrations by the infrared absorption and the lithium ion drift rate measurements is attributed to the use of a wrong value for the reaction constant K in the analysis of the latter experiments. Some data pertinent to the measurements are collected in table VII.

TABLE VII

Lithium ion drift results for crystals containing some oxygen.

| Sample TI, 1, 11 | | Sample TI, 1, 8 | | Sample TI, 1, 3 | |
|--|-------------------|--|----------------------------|--|----------------------------|
| $T_1 = 20\text{ }^\circ\text{C}$ | $\alpha_1 = 0.28$ | $T_1 = 80\text{ }^\circ\text{C}$ | $\alpha_1 = (0.9 \pm 0.1)$ | $T_1 = 80\text{ }^\circ\text{C}$ | $\alpha_1 = (0.9 \pm 0.1)$ |
| $T_e = 40\text{ }^\circ\text{C}$ | $\alpha_e = 0.48$ | $T_e = 30\text{ }^\circ\text{C}$ | $\alpha_e = 0.35$ | $T_e = 20\text{ }^\circ\text{C}$ | $\alpha_e = 0.31$ |
| $n_0 = 36 \times 10^{14}\text{ cm}^{-3}$ | | $n_0 = 41 \times 10^{14}\text{ cm}^{-3}$ | | $n_0 = 29 \times 10^{14}\text{ cm}^{-3}$ | |
| $\tau_{\text{Li}0+}(40\text{ }^\circ\text{C}) = 1\ 400\text{ s}$ | | $\tau_{\text{Li}0+}(30\text{ }^\circ\text{C}) = 3\ 900\text{ s}$ | | $\tau_{\text{Li}0+}(20\text{ }^\circ\text{C}) = 7\ 800\text{ s}$ | |
| $R = 11 \times 10^{-8}\text{ cm}$ | | $R = 10 \times 10^{-8}\text{ cm}$ | | $R = 18 \times 10^{-8}\text{ cm}$ | |
| $V = 90\text{ V}$ | | $V = 9\text{ V}$ | | $V = 9\text{ V}$ | |
| $W = 42\ \mu\text{m}$ | | $W = 18\ \mu\text{m}$ | | $W = 18\ \mu\text{m}$ | |
| $E_{\text{max}} = 32\ 000\text{ V/cm}$ | | $E_{\text{max}} = 8\ 000\text{ V/cm}$ | | $E_{\text{max}} = 8\ 000\text{ V/cm}$ | |

1.7.4 Crystals containing much boron

A considerable amount of boron is present in the crystals. Slices from Wacker, batch 2, with a resistivity of $8\ \Omega\text{cm}$ and accordingly a boron concentration of $16 \times 10^{14}\text{ atoms/cm}^3$ are probably in this category. Concerning this type of interaction there should be no uncertainty at all since lithium and boron concentrations are accurately known from the Hall effect and resistivity measurements and the equilibrium constant of the reaction may be taken from literature. However, as regards the latter quantity contradicting evidence exists.

The first data on this subject were published by KRÖGER³⁰ and were obtained from an analysis of PELL'S³¹ lithium ion drift measurements in a heavily boron doped junction. Using these results we calculate for our samples of Wacker, batch 2, a fraction α of unpaired lithium ions of 0.42 at $20\text{ }^\circ\text{C}$. Experimentally we find at this temperature $\alpha = 0.24$. Therefore we conclude that at least the greater part of pairing is due to LiB-formation. Some additional pairing due to oxygen may still be present and account for the difference between observed and calculated pairing fraction. This however is not necessarily so since considering all the errors involved in analysing the data the difference may be insignificant.

On the other hand, more recently, SPITZER and WALDNER³² derived values for the reaction constant from an infrared study of the intensity of some vibrational modes of boron and the LiB-

complex in a silicon lattice. Their values are about a hundred times larger than the former results. According to Spitzer and Waldner's results only one percent of the lithium ions in our Wacker, batch 2, samples will be trapped in a LiB-complex. In this case the observed pairing is entirely to be ascribed to LiO⁺ formation. To enable this the crystals should contain 5×10^{15} oxygen atoms per cm³. This amount of oxygen, which was not detected by infrared absorption (table IV) although being above the detection limit, is probably not present in these float-zoned crystals.

To obtain some more information concerning this problem we performed an experiment in which the time constant to reach equilibrium in the pairing reaction was measured. Such an experiment may provide useful information since the capture radii of the two possible reactions are quite different. In case 1.7.3 we found for the Li⁺-O reaction a capture radius of about 5×10^{-8} cm. Substituting the present values in the formula for τ_{LiO^+} , already mentioned in case 3, a time constant of 5.8 hours is predicted at a temperature of 20 °C. For the Li⁺-B⁻ reaction the capture radius is much larger owing to the long range electrostatic attraction between these oppositely charged ions. The value of this Coulomb capture radius is known from theory³³ to be 48×10^{-8} cm at 20 °C in silicon. Using a similar expression as before we expect the time constant τ_{LiB} to be 1.7 hours at 20 °C.

A decisive choice between these two possibilities was obtained by carrying out the following experiment. A junction was heated to 80 °C for nearly 10 minutes. After this heat treatment, during which all pairs have become dissociated, the junction was rapidly cooled to 20 °C. The ion drift rate was then measured as function of time. It was found, as illustrated in figure 8, that the fraction α of free lithium ions dropped from an initial value of 0.77 to a final value of $\alpha = 0.24$. In a second experiment the initial high and final lower equilibration temperature were chosen to be 70 and 10 °C respectively. The curves of α versus time were analysed to obtain values for the time constant. Some complication is added to these analyses by the fact that the deviations from equilibrium are not small. Therefore no simple exponential decay to equilibrium occurs, but instead also initial concentrations are involved. Carrying out the analyses for the two possible cases we find our data much more consistent assuming the Li⁺-B⁻ pairing to play the dominant role.

We therefore arrive at the conclusion that the observed ion pairing is well accounted for by the presence of the boron impurities and that the oxygen concentration will be much less than 5×10^{15} atoms/cm³. The equilibrium constant of the reaction $\text{Li}^+ + \text{B}^- \rightleftharpoons \text{LiB}$ as published by KRÖGER³⁰ and PELL³¹ explains our experimental results rather well, the value obtained by SPITZER and WALDNER³² does not seem to be applicable.

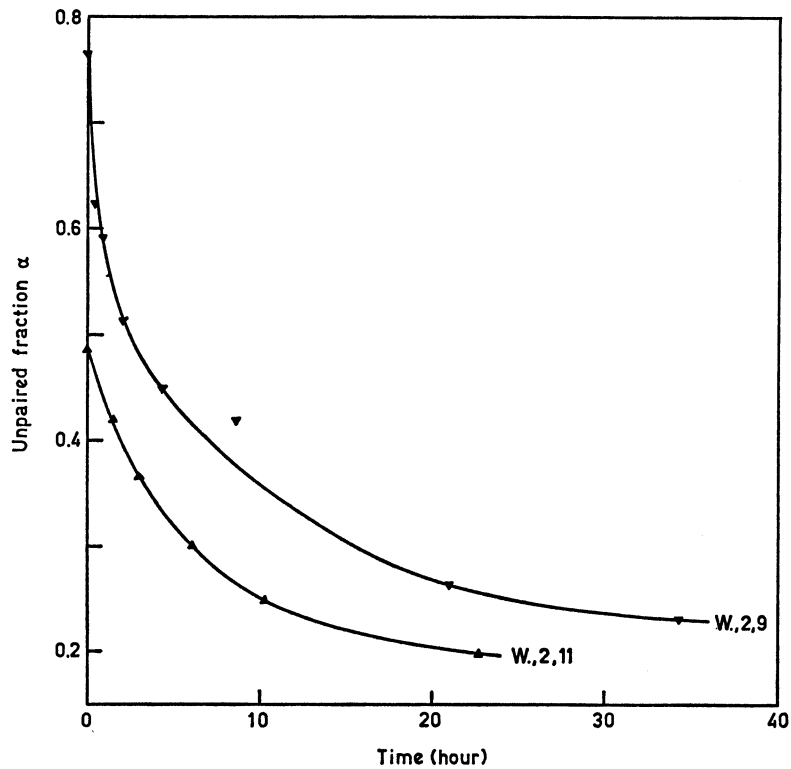


Fig. 8. Fraction α of unpaired lithium ions changing with time due to lithium-impurity complex formation. Sample Wacker, 2, 9 is equilibrated at 20 °C after being heated for 10 minutes to 80 °C; sample Wacker, 2, 11 is heated to 70 °C during 3 minutes and equilibrated at 10 °C.

1.8 Preparation method

In the previous paragraphs it was described how some studies were made concerning the impurity concentrations in silicon crystals. The method for preparing lithium drifted p-i-n junctions starting

from this basic silicon is given in this paragraph in conclusion of this chapter. Mainly the experimental aspects of the preparation techniques are described, which is easiest done by dealing separately with the three distinguished regions of the junction.

1.8.1 *Contact to the p-type region*

A silicon slice with the dimensions and general properties as given before is first washed to remove surface contamination in a synthetic detergent, water, methanol, trichloroethylene, methanol and water successively. All chemicals are of pa-grade; the water is deionized and doubly distilled in quartz apparatus (Heraeus) and has a conductivity less than $0.8 \mu\text{S}$. To remove surface damage due to foregoing mechanical treatments like sawing and grinding, the slice is subsequently etched. This is done in an etch liquid of composition $\text{HF}(40\%) : \text{HNO}_3$ (fumans) = 1 : 10 during 5 minutes. After having added the same amount of HNO_3 the etching is continued for another 10 minutes. During the etching the liquid is kept in continuous movement by shaking or stirring. The etch is prepared about 30 minutes before use and cooled by surrounding the polypropylene etch beaker with ice cubes. Etching is stopped by pouring water into the beaker.

Aluminium is deposited onto one of the circular sides of the slice by evaporation in a vacuum. The dimensions of the aluminium covered area are defined by a lucite mask. A thickness of the aluminium layer around $1 \mu\text{m}$ gives satisfactory results. The amount of aluminium to be evaporated is easily calculated from the geometry of the experimental setup.

To produce a low resistance non-rectifying contact the aluminium is alloyed with the silicon during 5 minutes at 650°C . The slice lies down on a graphite strip inserted in the quartz tube resistance heated oven. About 1 l/min of pure nitrogen is led through the oven during the alloying treatment.

A check on the behaviour of the contact is afforded by the four-point probe measuring technique. A low sheet resistance, $R_s \approx 0.03 \Omega$, is then always found in agreement with the value to be expected.

1.8.2 *The n-type layer*

Lithium is introduced into the other side of the slice by diffusion.

A thin layer of a lithium in oil suspension (Lithium Corporation of America) is painted on this side. This layer is dried by driving off the oil at a temperature of 250 °C during 20–40 minutes in an argon atmosphere. For that purpose the slice is brought into a quartz tube laying on a graphite strip. Around the quartz tube a SnO₂ resistance coated pyrex tube is slid by which this section of the oven is heated. Through this transparent construction the drying of the suspension is easily observed. After a dry looking surface is obtained the slice is shifted further into a second section of the quartz tube which is kept at 450 °C by a conventional wire wound heater. Here an n-type layer is created in the silicon by a 5 minutes diffusion. Immediately after diffusion the slice is quickly cooled down, quenched sometimes, to room temperature. Remaining rests of lithium are washed off in methanol and water. The diode is now ready for measurements of the sheet resistance of the lithium doped layer, the junction capacity and drift rate as fully described in the paragraphs 1.6 and 1.7. To improve the electrical contact to be made with the n-type region sometimes an aluminium layer is evaporated on top of the lithium area.

1.8.3 *The lithium drift process*

Before starting the lithium ion drift process the diode is washed according to the earlier mentioned standard procedure. The whole aluminium contact and the central part of the lithium doped region are covered with Apiezon wax (black wax), which is dried for at least three hours but by preference overnight. In an etch liquid of composition HF (40 %) : HNO₃ (fumans) : CH₃COOH (100 %) = 2 : 2 : 5 the edges of the diode are then etched during 15 minutes. After etching is finished the Apiezon wax is removed by solution in toluol and the slice is further washed in methanol and water. Then the slice is mounted in a steel holder with a spring contact pressing on the n-type surface. Lithium ion drift is carried out in a rapidly stirred bath containing silicon oil MS 200, viscosity 100 cS. The temperature of the oil is measured and controlled by a switching thermometer at 100–120 °C. Thermal contact between sample and oil bath is improved by mounting the sample with its p-type surface on a larger metal disc. To avoid thermal runaway the power dissipation in the diode is kept below 2 W by suitably choosing

drift temperature and reverse bias. A reverse bias between 100 and 500 Volt is used. The achieved thickness W of the intrinsic region is calculated from the known drift temperature and bias V by the formula:

$$W_2^2 - W_1^2 = 2\alpha\mu_{\text{Li}}V(t_2 - t_1).$$

(W_1 is initial thickness of the intrinsic region, W_2 is final thickness, α is fraction of free lithium ions at the drift temperature, μ_{Li} is lithium mobility at the drift temperature, V is drift voltage, $t_2 - t_1$ is drift time). For intrinsic regions of the usual thickness no appreciable errors are introduced by applying this formula also for the early stages of the drift process. An independent determination of junction width is obtained by capacity measurement and use of the relation $W = \epsilon A/C$. Junctions for irradiation studies were usually made with an intrinsic thickness of 1 mm. For this purpose the above-mentioned methods of thickness determination were adequate. These methods were however insufficiently accurate for junctions to be used as particle detectors. In general these junctions had to be made with a very thin remaining p-type layer. The thickness of this window is best determined by probing the surface with α -particles from a radioactive source. Some details of this method are given in section 3.3.5.

CHAPTER 2

PARTICLE IDENTIFICATION BY PULSE SHAPE DISCRIMINATION

2.1 Introduction

Lithium drifted p-i-n junctions have been developed in recent years with the prime aim of using them as nuclear particle detectors. Because of the large junction width they have a large sensitive volume and are capable of stopping high energy particles such as 50 MeV protons. In this chapter some work is presented which illustrates the application of lithium drifted p-i-n junctions in silicon as nuclear particle detectors. A method is described by which not only the energy is determined of the particle incident upon the detector, but also its nature. In the case considered the identification is between protons, deuterons and α -particles in the energy range 5–50 MeV.

A lithium drifted p-i-n junction essentially consists of three parts, which are:

- a) a low resistivity p-type, boron doped, region;
- b) a highly compensated region, which is intrinsic at room temperature;
- c) a low resistivity n-type, heavily lithium doped, region.

In a reverse-biased p-i-n junction the entire voltage is developed across the high resistivity intrinsic material, which thereby is the sensitive part of the detector. The p- and n-type boundary layers have the mere function of providing low resistance contacts. A p-i-n structure counter is the solid state analogon of the gasfilled ionization chamber; they both act on the principle of collecting charge created by ionization. A few important differences between these two detectors are the energy needed for the creation of a charge pair, the mobilities of the free carriers and the density of the stopping medium.

An ionizing particle, incident on the semiconductor detector, creates electrons and holes in the detector material. These free

carriers are separated by the external field, inducing by this a voltage pulse on the electrodes. The rise time of this signal will depend on the time needed for charge collection. This in turn depends on the distance to be traversed by the free charges, as determined by the initial charge carrier distribution. This means that the range of the incident particle will determine the pulse rise time. Some quantity indicative for the particle range may therefore be derived from the voltage pulse.

On the other hand the final pulse height is proportional to the energy lost by the particle in the detector. In the voltage pulse therefore information is contained about both the energy and the range of the particle. Since the nature of a particle is uniquely determined by these two quantities, an adequate pulse treatment may reveal the particle type.

The next paragraph gives a theoretical pulse shape analysis; the result shows the dependence of signal height on time and range or energy (fig. 9). In paragraph 2.3 the method used for particle identification is discussed. Beam arrangement, detector properties and electronic equipment are described in paragraph 2.4. The next paragraph gives the experimental and calculated results, while a discussion of these and some supplementary results concludes the chapter.

2.2 Pulse shape analysis

A list of symbols used in this paragraph is given with their definitions:

- x : position coordinate along the detector axis, $x = 0$ at the detector surface (fig. 12);
- W : thickness of the intrinsic region of the detector;
- R : range of the incident particle in the detector, i.e. range in silicon;
- ρ : reduced range, $\rho = R/W$;
- a, b : constants appearing in the range-energy relation;
- V : reverse bias of the detector;
- F : electric field in the sensitive detector region, $F = V/W$;
- μ_e : mobility of electrons in silicon;
- μ_h : mobility of holes in silicon;
- v_e : drift velocity of the electrons during their collection, $v_e = \mu_e F$;

- v_h : drift velocity of the holes during their collection, $v_h = \mu_h F$;
- t : time;
- $t_{t,e}$: transit time of electrons through the detector, $t_{t,e} = W^2/\mu_e V$;
- τ : reduced time, $\tau = t/t_{t,e}$;
- E_1 : energy of the incident particle;
- E_d : energy loss of the particle in the detector;
- E_e : pulse height due to the motion of electrons;
- E_h : pulse height due to the motion of holes;
- ε_e : reduced pulse height due to the motion of electrons,
 $\varepsilon_e = E_e/E_1$;
- ε_h : reduced pulse height due to the motion of holes, $\varepsilon_h = E_h/E_1$;
- ε : reduced total pulse height, $\varepsilon = \varepsilon_e + \varepsilon_h$.

It may be noticed that the same symbol E is used for pulse height and energy. This is justified by the fact that pulse heights represent an energy and occur only properly normalized to the energy scale.

In the derivation of the pulse shape formulae several assumptions have to be made, which delimit the validity of the results. Preceding the actual derivation of the formulae these assumptions are given below:

- a. The mobilities of electrons and holes are independent of the electric field.
- b. The electric field is constant over the whole intrinsic region. By this assumption, and also by the range-energy dependence which we will use, the present analysis differs from those given by TOVE and FALK³⁴ for the p-n junction detector.
- c. Particles are incident upon the detector on the p-side. This is the electrically negative side of the reverse-biased junction, towards which the created holes will move (fig. 12).
- d. All incident particles are directed perpendicular to the detector surface. The particle trajectories inside the detector are parallel to the electric field. This situation is usually not met with in the work with the ionization chamber.
- e. A contribution to the signal, arising from holes, which have diffused from the insensitive n-type region at the back of the detector to the intrinsic region, can be neglected.
- f. There is only a very thin insensitive p-type layer, window layer, in front of the detector. No contribution to the signal from diffused electrons is taken into account.

g. During the collection process no charge is lost by recombination or trapping.

h. The original charge distribution is not disturbed by diffusion.

i. An empirical range-energy relation $R = aE_i^b$ holds sufficiently.

j. $\mu_e = 3 \mu_h$.

The derivation of the pulse shape formulae proceeds along the following lines. A charged particle entering a semiconductor detector loses its energy mainly by the creation of electron-hole pairs. The mean energy spent for the creation of such a pair, is independent of the particle energy. This implies that the density of the charge distribution along the particle track will be proportional to the energy loss of the particle per unit length.

The energy loss per unit length dE/dx is derived from the range-energy relation of the particle in silicon. In this analysis an empirical relationship of the type $R = aE_i^b$ is used, which leads to the following expression for dE/dx :

$$\frac{dE}{dx} = - \frac{1}{a^{1/b} b (R-x)^{(b-1)/b}}.$$

The value of b may be determined from the slope of measured range-energy curves plotted on log-log paper. In the actual calculations for protons, deuterons and α -particles with energies between 5 and 50 MeV the value $b = 1.73$ was considered to be the best. The constant a was then found to have the value $a = 12$ for protons, $a = 7.23$ for deuterons and $a = 1.09$ for α -particles. This yields the following range-energy relations:

$$\begin{aligned} \text{protons: } R &= 12 E_i^{1.73}, \\ \text{deuterons: } R &= 7.23 E_i^{1.73}, \\ \alpha\text{-particles: } R &= 1.09 E_i^{1.73}. \end{aligned}$$

The electron-hole pairs are all created, within a very short time, at $t = 0$, when the particle is stopped in the detector. Because of the external field F , the holes created in the intrinsic region acquire a constant drift velocity $v_h = \mu_h F = \mu_h V/W$ in the direction of the negative p-type front layer. The holes created at $x = 0$ are the first to reach the front electrode at $t = 0$; the last ones, which are created at the end of the particle track $x = R$, arrive at the electrode at $t = RW/\mu_h V$. All electrons will move with constant drift velocity $v_e = \mu_e F = \mu_e V/W$ towards the positive back contact. The first

electrons reach this electrode at the time $t = W(W-R)/\mu_e V$. The last electrons which arrive at the electrode, are created at the position $x = 0$. These electrons have to traverse the entire detector thickness W , which requires the electron transit time $t_{t,e} = W^2/\mu_e V$.

In course of their collection process the electrons and holes are separated, causing a change in space charge distribution. A sudden decrease of detector bias will be the result. This decrease will be of transient character since ultimately the created charge is taken up by the detector voltage supply. In other words, by the separation of electrons and holes charge is induced on the detector electrodes. The amount of charge induced by one electron-hole pair, expressed in units of electronic charge, is equal to the separation of the electron-hole pair, expressed as fraction of the junction thickness W . The total pulse height at time t is obtained by integrating from $t = 0$ to that time the contributions from all electrons and holes.

Results of these calculations are given below. Although the preceding text is restricted to the case of particles which are stopped in the detector, calculations have also been made for more energetic particles which pass through the detector, losing only part of their energy in the detector volume.

For the case $R \leq W$ the results are:

Signal from the electrons:

$$0 \leq t \leq \frac{W(W-R)}{\mu_e V} : E_e = E_1 \frac{\mu_e V t}{W^2}$$

$$\frac{W(W-R)}{\mu_e V} \leq t \leq \frac{W^2}{\mu_e V} : E_e = E_1 \left\{ \frac{\mu_e V t}{W^2} - \frac{b}{b+1} \frac{R}{W} \left(1 - \frac{W}{R} + \frac{\mu_e V t}{RW} \right)^{(b+1)/b} \right\}$$

$$\frac{W^2}{\mu_e V} \leq t : E_e = E_1 \left(1 - \frac{b}{b+1} \frac{R}{W} \right).$$

Signal from the holes:

$$0 \leq t \leq \frac{RW}{\mu_h V} : E_h = E_1 \frac{b}{b+1} \frac{R}{W} \left\{ 1 - \left(1 - \frac{\mu_h V t}{RW} \right)^{(b+1)/b} \right\}$$

$$\frac{RW}{\mu_h V} \leq t : E_h = E_1 \frac{b}{b+1} \frac{R}{W}.$$

These formulae can be presented more concisely after the introduction of appropriate scales for the variables time, range and pulse height. The time t , relative to the electron transit time $W^2/\mu_e V$, is denoted by τ and called reduced time. Assuming $\mu_e = 3\mu_h$, the hole transit time $W^2/\mu_h V$ is given by the reduced time $\tau = 3$. A reduced range is defined by $\rho = R/W$. Reduced pulse heights for electrons and holes respectively are given by $\varepsilon_e = E_e/E_1$ and $\varepsilon_h = E_h/E_1$. Also for particles penetrating through the detector they represent the pulse height relative to the pulse height corresponding with the incident particle energy. In the general case ε is a function of τ and ρ .

For the case $\rho \leq 1$ the results are then:
Signal from the electrons:

$$\begin{aligned} 0 \leq \tau \leq 1 - \rho & : \quad \varepsilon_e = \tau \\ 1 - \rho \leq \tau \leq 1 & : \quad \varepsilon_e = \tau - \frac{b}{b+1} \rho \left(1 - \frac{1-\tau}{\rho}\right)^{(b+1)/b} \\ 1 \leq \tau & : \quad \varepsilon_e = 1 - \frac{b}{b+1} \rho. \end{aligned}$$

Signal from the holes:

$$\begin{aligned} 0 \leq \tau \leq 3\rho & : \quad \varepsilon_h = \frac{b}{b+1} \rho \left\{1 - \left(1 - \frac{\tau}{3\rho}\right)^{(b+1)/b}\right\} \\ 3\rho \leq \tau & : \quad \varepsilon_h = \frac{b}{b+1} \rho. \end{aligned}$$

The pulse shapes of particles which pass through the detector are calculated by the same method. For this case, where $\rho \geq 1$, the results are:

Signal from the electrons:

$$\begin{aligned} 0 \leq \tau \leq 1 & : \quad \varepsilon_e = \tau - \frac{b}{b+1} \rho \left\{ \left(1 - \frac{1-\tau}{\rho}\right)^{(b+1)/b} - \left(1 - \frac{1}{\rho}\right)^{(b+1)/b} \right\} \\ 1 \leq \tau & : \quad \varepsilon_e = 1 - \frac{b}{b+1} \rho \left\{1 - \left(1 - \frac{1}{\rho}\right)^{(b+1)/b}\right\}. \end{aligned}$$

Signal from the holes:

$$0 \leq \tau \leq 3 : \quad \varepsilon_h = -\frac{\tau}{3} \left(1 - \frac{1}{\rho}\right)^{1/b} + \frac{b}{b+1} \rho \left\{ 1 - \left(1 - \frac{\tau}{3\rho}\right)^{(b+1)/b} \right\}$$

$$3 \leq \tau : \quad \varepsilon_h = \rho \left\{ \frac{b}{b+1} + \frac{1}{b+1} \left(1 - \frac{1}{\rho}\right)^{(b+1)/b} - \left(1 - \frac{1}{\rho}\right)^{1/b} \right\}.$$

Since the boundary values for the validity of the latter formulae do not depend on the particle range, in contrast with the case $\rho < 1$, the formulae for ε_e and ε_h may be added to give the total pulse height. Some simplification arises therefrom; for instance when $\tau \geq 3$ the result becomes:

$$\rho \geq 1, \quad \tau \geq 3 : \quad \varepsilon = 1 - \left(1 - \frac{1}{\rho}\right)^{1/b},$$

which implies:

$$E_d = E_1 \left\{ 1 - \left(1 - \frac{1}{\rho}\right)^{1/b} \right\}.$$

In the actual calculations the value $b = 1.73$ was substituted in the formulae. Only the variables τ and ρ are then left; τ defines the time, while the pulse shape is determined by ρ exclusively. The results, as presented graphically in figure 9, were obtained by means of the computer X1 of the "Mathematisch Centrum", which was programmed in Algol 60.

In the figures 10 and 11 some pulses experimentally recorded as oscilloscope traces are reproduced. Unfortunately these had to be touched up because of lack of contrast in the original pictures. A set of five pulses, originating in deuterons with energies between 4 and 25 MeV, is shown in figure 10. Figure 11 gives a few pulses from α -particles with energies between 25 and 50 MeV. The behaviour of the pulse shape verifies the predictions based on the ρ -values and the curves presented in figure 9. A comparison between the deuteron and α -particle pulses at 25 MeV demonstrates clearly that different pulse shapes belong to particles of the same energy but of different range.

2.3 Particle identification method

The nature of a particle is determined by specifying its range and its energy. Particle identification is therefore possible in principle,

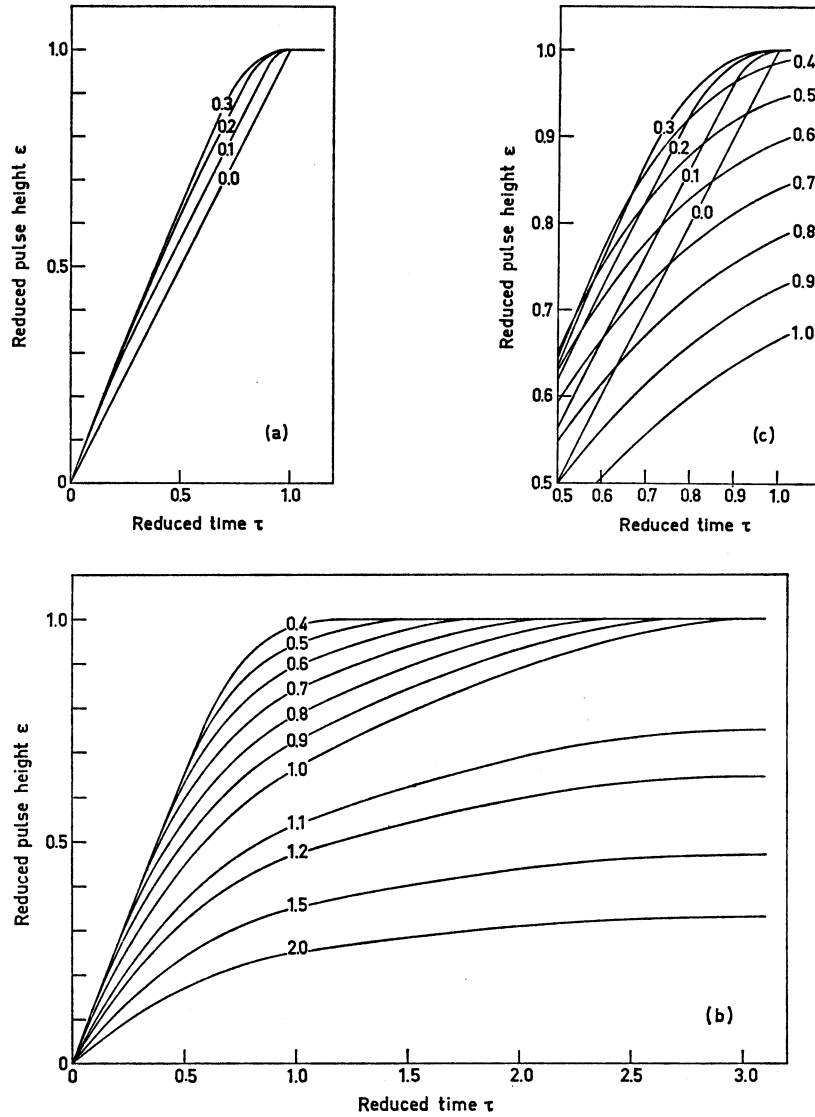


Fig. 9. Calculated pulse shapes for radiation incident normally on the p-side of a p-i-n detector. The curves are labelled with the relevant value of the reduced range.

since the voltage pulse, produced by the particle in the detector, contains information about both these quantities. The final pulse height, always reached at $\tau = 3$, is proportional to the energy lost

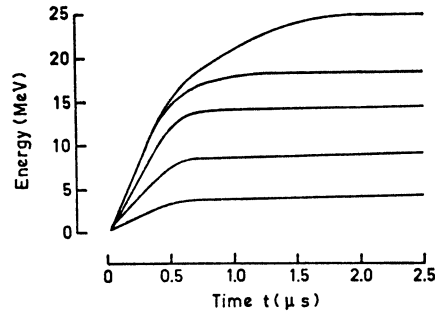


Fig. 10. Oscilloscope pictures of deuteron pulses. Particles are incident normally on the p-side of the p-i-n detector. $W = 2250 \mu\text{m}$, $V = 42 \text{ V}$, $t_{t,e} = 0.72 \mu\text{s}$. Deuteron energies: 4, 9, 14, 18 and 25 MeV; corresponding ρ -values: 0.04, 0.14, 0.32, 0.49 and 0.86.

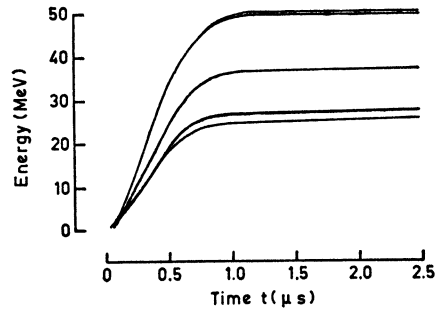


Fig. 11. Oscilloscope pictures of α -particle pulses. Particles are incident normally on the p-side of the p-i-n detector. $W = 2250 \mu\text{m}$, $V = 42 \text{ V}$, $t_{t,e} = 0.72 \mu\text{s}$. α -Particle energies: 25, 27, 36, 50 and 51 MeV; corresponding ρ -values: 0.13, 0.15, 0.25, 0.43 and 0.44.

in the detector, while, as is shown in the preceding paragraph, the pulse shape depends on the range. In the particle identification method which we adopted, the pulse height at a fixed time during the pulse rise time, is used as the range dependent quantity. Some considerations concerning the choice of this fixed time, called t_{c1} , are:

- a. The pulse height for any $\tau \geq 1$ is not able to discriminate between ρ -values in the range $0 \leq \rho \leq \frac{1}{3}$ (fig. 9a).
- b. For all times $0 < \tau < 1$ the pulse height depends on ρ .
- c. At the time $\tau = 0$ the slope of the pulse shape curves, $(d\varepsilon/d\tau)_{\tau=0}$,

is equal to $\frac{4}{3}$, for all $\rho \neq 0$. For τ near zero, the pulse height variations with ρ are consequently small.

For the purpose of particle identification the region of primary interest centres around $\tau = \frac{3}{4}$, where the pulse height is most sensitive to the reduced range ρ . This region is drawn on enlarged scale in figure 9c. One arrives at the same conclusion by examination of figure 19, which gives the dependence of ε on ρ , for various values of τ .

The particle identification depends on the pulse height at the time t_{c1} , abbreviated to E_{c1} . A two-dimensional display of E_{c1} versus the measured energy E_d shows the particle identification by giving separate curves for the different particle types. However, the differences obtained in this way are relatively small. The following procedure yields some improvement. If the dependence of ε on ρ is neglected for the moment by taking as an approximate average the curve for $\rho = 0$, the relation $E_{c1} = \tau_{c1} E_d$ is valid in the time period $0 \leq \tau \leq 1$ which is of our interest. Thus subtracting αE_d from E_{c1} , the quantity $E_{c1} - \alpha E_d$ is introduced. By choosing $\alpha = \tau_{c1}$ this quantity is exactly zero for $\rho = 0$, but also in the real situation $\rho \neq 0$ it tends to zero. Since the differences for the various particle types are unaffected by the subtraction, the relative differences are increased. In the experimental work this method was followed.

2.4 Experimental arrangement

2.4.1 Beam arrangement

The experiments were performed with the synchrocyclotron of the "Instituut voor Kernfysisch Onderzoek", which at the time of this research was able to accelerate deuterons to 26 MeV and α -particles to 52 MeV. Most experiments were done with a beam made up of deuterons and α -particles simultaneously. High energy protons were produced in the reaction $^{12}\text{C}(d, p)^{13}\text{C}$ which yields protons of nearly 29 MeV at small scattering angles, since the energy release Q of the reaction is +2.72 MeV. An absorber with a step by step varying thickness, drawn schematically in figure 12, is placed in front of the detector. The various groups of degraded energies, obtained in this way, can be observed in the figures 14 to 18.

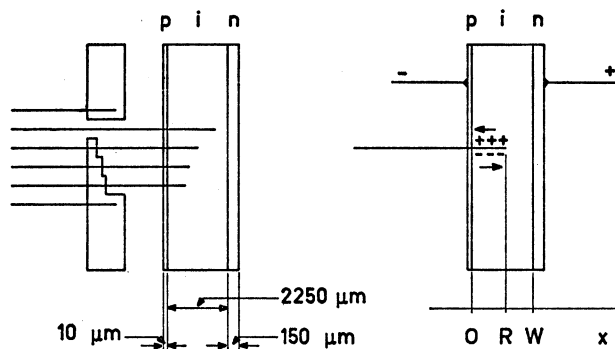


Fig. 12. Schematic representation of the collimator, absorber and detector arrangement. Some quantities related to the detector are also illustrated.

2.4.2 Detector properties

The detector is made from a Merck, batch 1, silicon slice according to the recipe described in reference 1 and paragraph 1.8. Some particular data concerning the detector used are:

a. It has a circular sensitive area of about 3 cm^2 . The beam is collimated by the absorber on a square area of $5 \times 5 \text{ mm}^2$ in the centre of this circle.

b. The thickness of the window in front of the detector is determined by measurements with the 6.06 and 8.78 MeV α -particles emitted by a ^{212}Pb -source. After applying a correction for the diffusion contribution to the pulse height the window thickness was found to be $(10 \pm 5) \mu\text{m}$.

c. At all reverse voltages used in the experiments the intrinsic thickness of the detector is $(2250 \pm 50) \mu\text{m}$. Deuterons and α -particles are stopped in the sensitive volume, while protons with energy above 20.5 MeV pass through it.

d. The thickness of the insensitive n-type region at the back of the detector is $(150 \pm 50) \mu\text{m}$.

e. During the experiments the detector was cooled to a temperature given by $(-20 \pm 20) ^\circ\text{C}$. The temperature was not kept constant very well. Typical values for the current of the cooled detector are 0.015, 0.03 and $0.06 \mu\text{A}$ at reverse voltages of 42, 84, and 126 V respectively. The noise generated in the detector is small compared to the electronic contributions to the noise.

2.4.3 Electronic equipment

A block diagram of the electronic arrangement is given in figure 13. Of course, the functional units included in this scheme follow closely the method set out in paragraph 2.3.

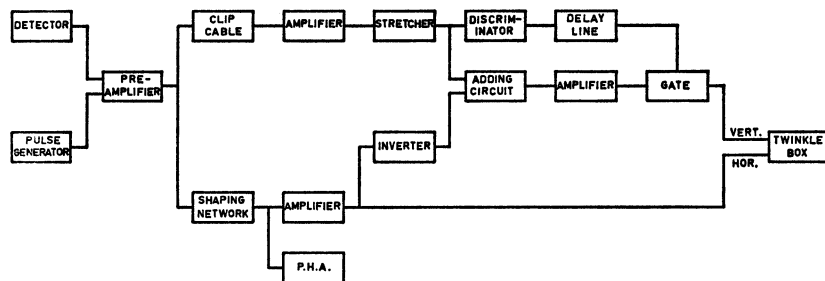


Fig. 13. Block diagram of the electronic equipment.

The voltage signal, originating in the detector, is led to a pre-amplifier, which has a linear characteristic up to high frequencies to avoid distortion of the pulse shape. The first stage, a cascode amplifier consisting of two E810F tubes, is made charge sensitive by feedback through a small capacitance. Further amplification is obtained in a second stage in which transistors of the type 2N769 are used. The preamplifier in whole has a rise time of less than 6 ns.

In the lower line of the block diagram the treatment of the energy loss pulse E_d is represented. The shaping network symbolizes a single differentiating network with a time constant of 10 μ s, which improves the energy resolution by suppressing the low frequency noise. The signal E_d provides the horizontal bending of the twinkle-box beam.

In the upper line of the diagram the signal E_{c1} is formed by delay-line clipping of the preamplifier output pulse at the time t_{c1} . In this way the signal E_{c1} is made equal to the pulse height at $t = t_{c1}$, in accordance with its definition.

In the adding circuit the pulses E_{c1} and inverted E_d are mixed to form the signal $E_{c1} - \alpha_{exp} E_d$. The parameter α_{exp} , determining the relative weight of the two mixed signals, is continuously variable over the required range. The signal E_{c1} acquires its correct value at an earlier point of time than E_d . Thus in order to make a subtraction of the right pulse heights the signal E_{c1} is stretched. A differentiating

network causes the tail of the stretched signal to drop off with a characteristic time of $10 \mu\text{s}$, the same as for E_d . Also the identification signal $E_{c1} - \alpha_{\text{exp}} E_d$ does not assume its correct value before the pulse rise time has elapsed. Only this value passes the gate circuit at a time somewhat larger than the maximal pulse rise time. It is led to the twinkle-box where it determines the vertical position of the spot. The gate is triggered by the delayed discriminator output pulse.

2.5 Results

2.5.1 Experimental results

As mentioned in the preceding discussion the experimental results have the shape of twinkle-box pictures. Some of the pictures are reproduced in the figures 14 to 18. These figures give the identification quantity $E_{c1} - \alpha_{\text{exp}} E_d$ as function of the detected energy E_d . The α -particles are represented by the curves extending from 0 to 52 MeV (figs. 14, 15, 16, 18), deuteron curves are confined between 0 and 26 MeV (figs. 14 to 18). Protons which are stopped in the detector give the curves between 0 and 20.5 MeV; protons with higher energy than this penetration value lose less energy in the detector and are responsible for the lower part of the proton curve, which goes down to about 10 MeV (figs. 17, 18). The vertical axis, representing $E_{c1} - \alpha_{\text{exp}} E_d$, was not calibrated. The parameter α_{exp} was adjusted so as to give a clear picture, with about horizontal α -particle curve. In this way α_{exp} was made approximately equal to τ_{c1} ; the exact value of α_{exp} is however unknown.

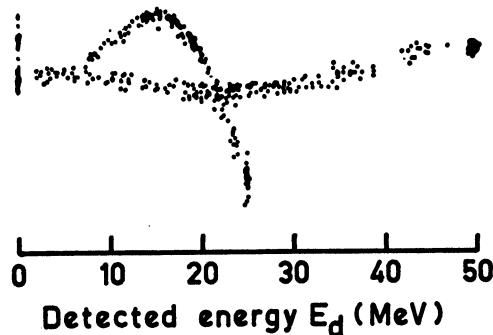


Fig. 14. The separation between deuterons and α -particles. $W = 2250 \mu\text{m}$, $V = 84 \text{ V}$,
 $t_{t,e} = 0.36 \mu\text{s}$, $t_{c1} = 0.2 \mu\text{s}$, $\tau_{c1} = 0.56$.

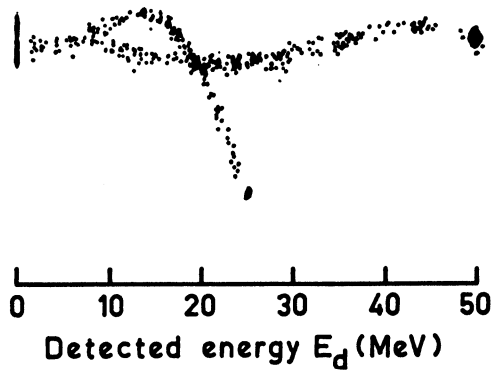


Fig. 15. The separation between deuterons and α -particles. $W=2250 \mu\text{m}$, $V=42 \text{ V}$,
 $t_{t,e} = 0.72 \mu\text{s}$, $t_{c1} = 0.6 \mu\text{s}$, $\tau_{c1} = 0.83$.

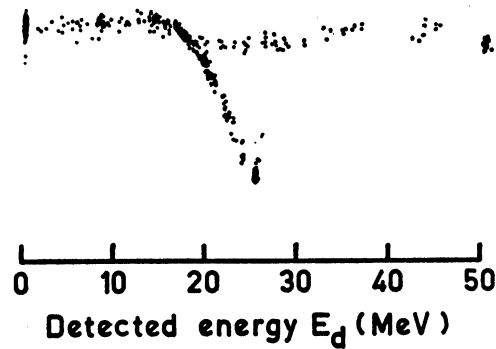


Fig. 16. The separation between deuterons and α -particles. $W=2250 \mu\text{m}$, $V=84 \text{ V}$,
 $t_{t,e} = 0.36 \mu\text{s}$, $t_{c1} = 0.4 \mu\text{s}$, $\tau_{c1} = 1.11$.

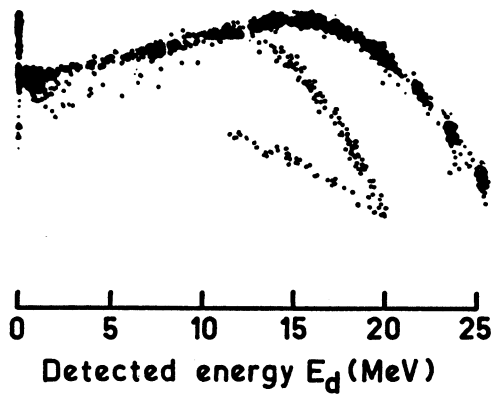


Fig. 17. The separation between protons and deuterons. $W = 2250 \mu\text{m}$, $V = 84 \text{ V}$,
 $t_{t,e} = 0.36 \mu\text{s}$, $t_{c1} = 0.3 \mu\text{s}$, $\tau_{c1} = 0.83$.

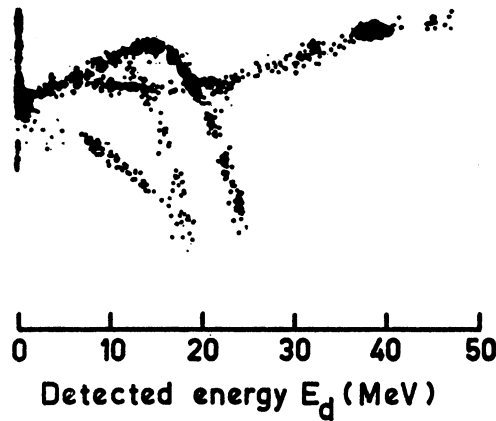


Fig. 18. The separation between protons, deuterons and α -particles. $W = 2250 \mu\text{m}$, $V = 84 \text{ V}$, $t_{t,e} = 0.36 \mu\text{s}$, $t_{cl} = 0.3 \mu\text{s}$, $\tau_{cl} = 0.83$.

In the figures 14, 15 and 16 the separation between deuterons and α -particles is shown. The figures 14 and 16 refer to the detector at a reverse bias of 84 V and pulse clip times of 0.2 and 0.4 μs respectively. The picture for the condition $V = 84 \text{ V}$, $t_{cl} = 0.3 \mu\text{s}$, also available, fits between the figures 14 and 16, but its publication would have meant a duplication of figure 18. For this reason the result for the equivalent condition $V = 42 \text{ V}$, $t_{cl} = 0.6 \mu\text{s}$, having the same τ_{cl} , is given as figure 15. Although not reproduced, twinkle-box pictures were taken both at higher and at lower values of the pulse clip time. Similar sets of photographs were also obtained for reverse detector voltages of 42 and 126 Volt; they yielded equivalent results.

The separation of protons and deuterons is demonstrated by figure 17, and in figure 18 all types of particles are shown together.

2.5.2 Calculated results

All the basic information required for calculations to check the observed phenomena, is contained in the results of the pulse shape analysis given in paragraph 2.2. The same data as presented in figure 9 are used to compose figure 19. This figure shows the dependence of the reduced pulse height on the reduced range at some points of time with $0 \leq \tau \leq 1$, which are of interest in our particle identification method.

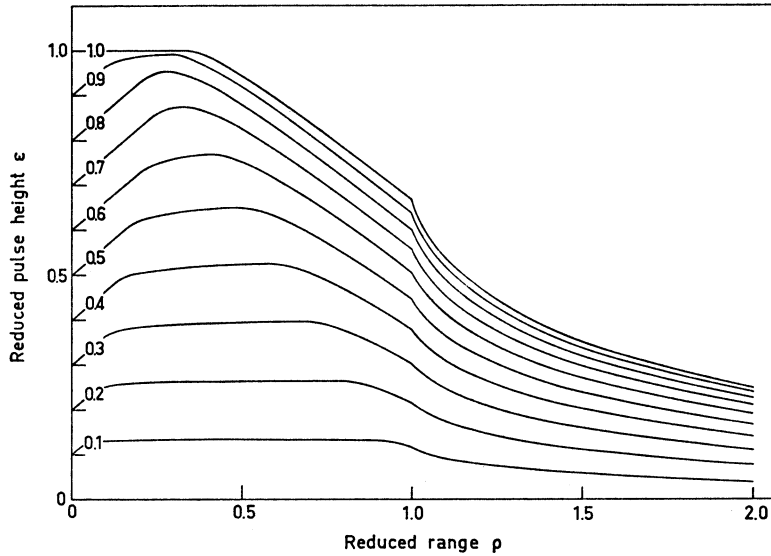


Fig. 19. Analysis showing the dependence of the reduced pulse height on the reduced range for various times during the pulse rise time. The parameter reduced time is indicated on the curves.

For the present detector thickness $W = 2250 \mu\text{m}$ actual calculations of the identification quantities were made as follows. For each particle type the range R is calculated as function of the incident energy E_1 using the relation $R = aE_1^b$ and the parameter values given in paragraph 2.2. Then, by division through W , the reduced range ρ is determined. The detected energy E_d , plotted on the horizontal axis, equals E_1 in the case $\rho \leq 1$, but for $\rho \geq 1$ it is given by the expression $E_1\{1 - (1 - 1/\rho)^{1/1.73}\}$. For the chosen pulse clip time the value of E_{c1}/E_1 is read from figure 19, whereupon E_{c1} and E_d then both are known. The quantity exactly corresponding to the experimental identification signal $E_{c1} - \alpha_{\text{exp}} E_d$ cannot be calculated, since α_{exp} was not measured. No large errors are made however by approximating α_{exp} with τ_{c1} . Consequently the quantity $E_{c1} - \alpha_{\text{calc}} E_d$ is introduced in the present calculations, where α_{calc} is defined by $\alpha_{\text{calc}} = \tau_{c1}$. In the curves, drawn for comparison with the experimental results, $E_{c1} - \alpha_{\text{calc}} E_d$ is plotted vertically. The figures 20, 21 and 22 show the final results calculated for $\tau_{c1} = 0.6, 0.8$ and 1.0 respectively. The upper horizontal axis refers to protons with

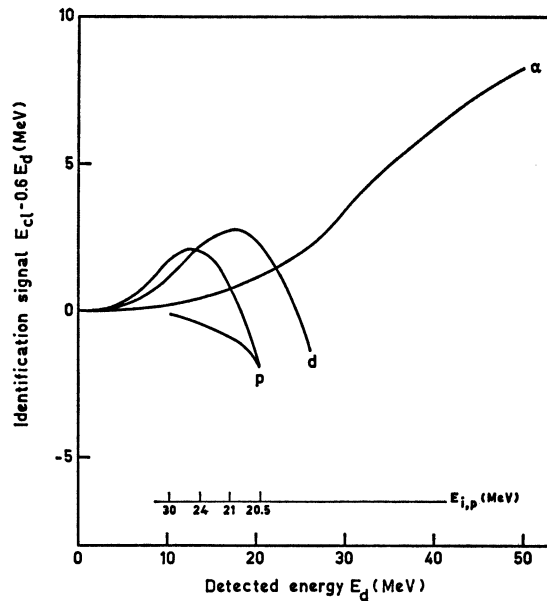


Fig. 20. Analysis of the separation between protons (p), deuterons (d) and α -particles (α) for the reduced clip time $\tau_{cl} = 0.6$; $\alpha_{calc} = 0.6$.

energy above the penetration value of 20.5 MeV and gives their incident energy $E_{i,p}$.

2.6 Discussion

2.6.1 Temperature of the detector

It was established experimentally that the noise level of the detector was reduced by cooling. The noise, as function of temperature, detector current or frequency, could not be understood in terms of shot noise due to space charge generated current. Probably the edge effects are dominant.

The mobility of electrons and holes in silicon is temperature dependent, and consequently the pulse rise time will be too. For the conditions $W = 2250 \mu\text{m}$, $V = 84 \text{ V}$, $T = 293 \text{ }^\circ\text{K}$ the electron transit time is calculated to be $0.45 \mu\text{s}$, substituting the room temperature value $\mu_e = 1350 \text{ cm}^2/\text{V s}$. Taking a $T^{-2.5}$ temperature

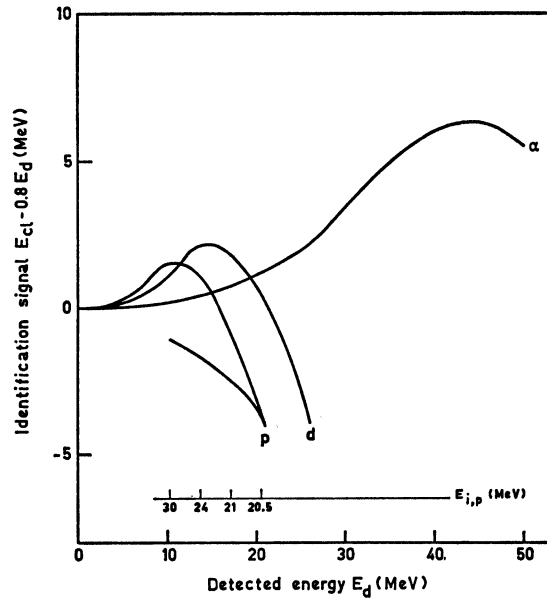


Fig. 21. Analysis of the separation between protons (p), deuterons (d) and α -particles (α) for the reduced clip time $\tau_{cl} = 0.8$; $\alpha_{calc} = 0.8$.

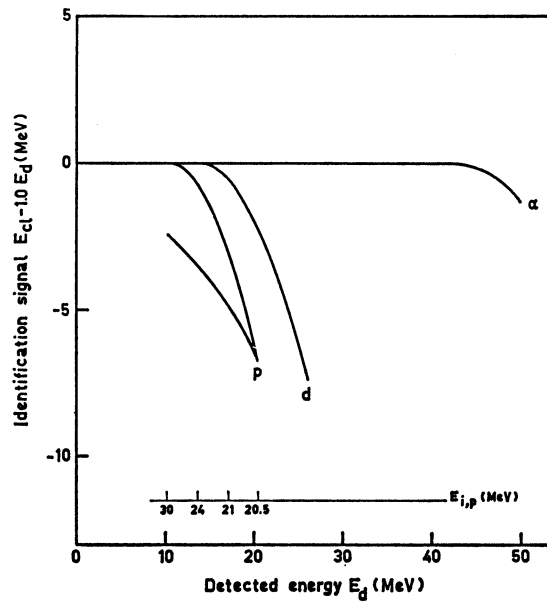


Fig. 22. Analysis of the separation between protons (p), deuterons (d) and α -particles (α) for the reduced clip time $\tau_{cl} = 1.0$; $\alpha_{calc} = 1.0$.

dependence for the electron drift mobility⁹, assuming lattice scattering being the predominant scattering mechanism, the electron transit time is decreased to 0.31 μs at -20°C . Examination of the figures 10 and 11 suggests that a slightly higher value near 0.4 μs was realized in practice. Therefore an average value $t_{t,e} = 0.36 \mu\text{s}$ was used in the calculations of the reduced pulse clip times for the experimental situations represented in the figures 14, 16, 17 and 18. For the situation of figure 15, $V = 42 \text{ V}$, the value $t_{t,e} = 0.72 \mu\text{s}$ is taken. On cooling the detector, faster pulses were observed, confirming the increased charge carrier mobility at lower temperature.

2.6.2 Comparison of experimental and calculated results

The results obtained experimentally are in good agreement with the results of the calculations. This conclusion can be drawn from a comparison of the corresponding figures: 14 and 20; 15, 17, 18 and 21; 16 and 22. A few of the most noteworthy features which demonstrate the similarity are:

- a. The general shape of proton, deuteron and α -particle curves and their relative positions.
- b. The value of E_d at the point of intersection between proton and α -particle curves (figures 18, 21).
- c. The E_d -values at the intersections of deuteron and α -particle curves as function of τ_{e1} (figures 14, 15, 16, 20, 21, 22).
- d. The energy above which protons and deuterons are separated.
- e. The equal values of $E_{e1} - \alpha E_d$ for protons at their penetration energy ($E_d = 20.5 \text{ MeV}$) and deuterons of maximum energy (figures 17, 18, 21).

The conformity between the experimental and calculated results proves that these aspects of the operation of the p-i-n junction detector are quite well understood. Apparently all assumptions made in the derivation of the formulae are reasonably valid.

In addition it may be noted that the values of τ_{e1} and α_{exp} in the experimental case are not exactly equal to the values of τ_{e1} and α_{calc} on which the calculations are based. Some slight deviations are explained by these facts.

2.6.3 Particle identification capabilities

Optimal separation of deuterons and α -particles is demonstrated by

figure 14 for $\tau_{c1} = 0.56$. With exception of the energies around the point of intersection at 22 MeV, separation is achieved above 8 MeV. The intersection point energy can be shifted upwards by taking a shorter pulse clip time, but only at the cost of the discrimination at lower energies.

At low energies the separation is bad in all cases. This is to be expected since the particle identification depends on differences in $E_{c1} = \varepsilon(\tau_{c1}, \rho)E_1$. For low values of ρ no large differences in $\varepsilon(\tau_{c1}, \rho)$ will be found, which means that even the relative effect is small. Moreover at low energies the influence of the window-layer of the detector becomes important. The stated value of 10 μm is the range of a 3.5 MeV α -particle.

The width of the curves is not sensitive to the detector bias and may be caused by the noise. In this respect no serious attempts have been made to improve the separation.

2.6.4 Thicker detector

Some experiments, with deuterons and α -particles, were carried out with a thicker p-i-n detector, $W = 4400 \mu\text{m}$. Since the largest range, that of 26 MeV deuterons, is about 2000 μm , only the first half of the detector is made good use of. The main differences with the results for the detector with $W = 2250 \mu\text{m}$ are:

a. The separation at the lower energies is somewhat less. This is explained by the fact that the same differences in range R result in differences in the reduced range ρ which are half as great, since W is twice as large.

b. The curves for reduced clip times around $\tau = \frac{3}{4}$ do not intersect. The points of intersection, obtained by extrapolation of the deuteron curves above 26 MeV, agree with the results of the calculations made for this detector.

2.6.5 Radiation on the n-side

It was expected that better separation could be obtained if particles were incident on the n-type side of the detector. The advantage is that after this detector reversal the less mobile holes generally have to traverse the longer distance. This implies that the pulse rises faster monotonously when the range increases. This is in contrast with the situation for radiation incident on the p-side of the detec-

tor. In this case, as shown in figure 19, ε_{c1} first increases as function of ρ up to about $\rho = \frac{1}{3}$, and then decreases. This bad property causes the intersection of the curves.

Consequently the case of radiation incident on the n-type side of the detector has been considered theoretically too. A pulse shape analysis, analogous to that given in paragraph 2.2 was made, and graphs like those given in the figures 20 to 22 were composed. These graphs indeed show that better separation is obtained. The phenomenon of the intersecting curves has disappeared almost completely and can be avoided easily.

Unfortunately no experiments could be carried out with particles incident on the n-side of the detector. At the time of this research no detector was available with a window-layer on this side of less than 150 μm .

2.6.6 Pulse shaping by RC-networks

In many practical applications the shaping of detector pulses is performed by using a band pass filter, consisting of an integrating RC-network followed by a differentiating RC-network. These filters have the advantage of being simply adjustable and they have good properties as regards optimization of the signal to noise ratio. To minimize noise with a $1/f^2$ power characteristic, as will be caused by shot noise, networks with short time constants are preferred.

Non-linear distortion will be introduced, however, if time constants comparable to the detector pulse rise time are chosen. In this case the input pulse may not be considered as being a step function, and the output pulse height will also be affected by its shape. Calculations, using the X1 computer of the "Mathematisch Centrum" in Amsterdam, were carried out on this effect. As in the preceding text shaping network time constants t_{RC} are expressed in reduced units τ_{RC} , by division through the electron transit time $t_{t,e}$. A non-linear distortion parameter is introduced as the maximal difference in output pulse height to input pulse height ratio for all types of input pulse shapes, i.e. for all ranges of particles. Results are: a non-linear distortion factor 1.31 for $\tau_{RC} = 1$; 1.10 for $\tau_{RC} = 1.8$; 1.01 for $\tau_{RC} = 5.5$. More details are given elsewhere³⁵.

2.6.7 *Two detector method*

A well developed method for the identification of charged particles at the energies considered in this chapter is the system in which the energy and the energy loss per unit length dE/dx are measured in two separate detectors. Using these quantities in suitable analog computations an output pulse is obtained, which almost independent of the particle energy, is characteristic for the particle type³⁶. The particle separation obtained by this system is superior to the first results of the one detector method. An advantage of the method based on pulse shape discrimination is that there is no need for a thin dE/dx detector and that its noise is consequently eliminated.

CHAPTER 3

IRRADIATION DAMAGE IN LITHIUM DOPED SILICON

3.1 Introduction

So far we have been concerned only with one mechanism of energy loss of an energetic particle passing through a silicon crystal. This was the process of ionization, that is the excitation of electrons from bound states in the valence band to free states in the conduction band. Although this process is the prominent form of energy loss, it is not the only one, others being atomic displacements and nuclear transmutations. In contrast to the ionization effects the latter processes effectuate permanent changes in the crystal structure. This radiation damage will not anneal out completely as long as the crystal remains at ordinary temperatures. Atomic displacements arise from the collision of the incident energetic particle with a silicon atom constituting the lattice. If in the collision process enough energy is transferred to the silicon atom it will be ejected from its regular lattice site. Eventually, particularly at low temperature, the displaced atom will come to rest in an interstitial position somewhere near its vacated site, the lattice vacancy. The pair of lattice defects which has been created, lattice vacancy plus silicon atom in an interstitial position, is called a Frenkel pair. It is the simplest form of a primary irradiation defect. More complex primary defect structures, such as divacancies or larger clusters, may also be produced if enough energy is available. These defects are all called primary, because they are produced rather directly by the incident particle along its track, within the very short passage or stopping time of about 10^{-12} seconds. Most of the primary damage will consist of Frenkel pairs after irradiation with light particles, electrons for instance. Also after gamma irradiation this will be the case, since gamma rays interact indirectly with the lattice via electrons. Heavier particles, such as protons, α -particles, fission fragments, and also neutrons, will produce the larger size defects. In our experimental work only gamma ray and electron

irradiations were carried out. Therefore any explanation of the results will be based on the Frenkel pair as the primary defect structure. It is felt that understanding of this simplest case constitutes the basis for gaining an insight into the more complicated situations.

The distance of separation between vacancy and interstitial of a Frenkel pair depends on the kinetic energy transferred to the displaced atom. Various types of close pairs, separated by a few atomic distances, may exist, but also isolated vacancies and interstitials, separated beyond their mutual interacting forces, may be generated. These latter isolated types of defects are unstable in silicon near room temperature. In n-type silicon the negatively charged vacancy disappears in a 15-minute isochronal anneal at 60 °K, whereas in p-type silicon the probably neutral vacancy anneals at 160–180 °K, also in a 15-minute isochronal annealing procedure^{37, 38, 39}. Although less well established the interstitial atom is believed to disappear already at liquid helium temperature^{38, 39}. At these low temperatures the primary point defects have sufficiently high mobility to diffuse over large distances through the lattice. Finally they are trapped by other impurities, already present in the lattice, with which stable defect configurations may be formed. For example, in one of the few reactions which at present is known with certainty, the vacancy, symbolized by V, is captured by an interstitial oxygen atom. Following the reaction: $O_{\text{int}} + V \rightarrow O_{\text{subst}}$, a substitutional oxygen atom is formed, which during the many years preceding its identification was called the A-centre. This example illustrates the role of chemical and other crystal imperfections in the creation of new defect types. In order to be able to understand these phenomena one needs to know the amount of dominant impurities present in the silicon crystals. For this reason the rather extensive investigations as reported in chapter 1 were undertaken. As a result the lithium concentration, the boron concentration, the concentration of compensating donors, presumably phosphorus, the (interstitial) oxygen concentration and the number of dislocations is known in the crystals, which were used for irradiation damage studies. As demonstrated by the pairing reactions described in paragraph 1.7 the mobility of lithium ions is high near room temperature. Therefore lithium ions will not only behave as a possible trap for diffusing primary defects, but also as an active diffusant. Lithium ions may precipitate on other defects. By all these processes various new

types of composite defect structures may be created; these are called secondary defects.

Analogous to the more chemical impurities, the irradiation produced imperfections may affect the properties of the semiconductor. For instance a defect showing donor or acceptor action, a defect which is an effective recombination centre or manifests itself otherwise, may be produced. In the earlier mentioned example an interstitial oxygen atom, which is an electrically inactive impurity, is converted into a substitutional oxygen atom. With this latter defect an acceptor level, located 0.17 eV below the conduction band, is associated. Therefore, when this defect is introduced by irradiation of n-type oxygen containing silicon, the conductivity will be decreased because electrons will be taken from the conduction band states to fill the lower lying acceptor levels. At present silicon single crystals containing very small amounts of impurities, in the order of one impurity per 10^{10} silicon atoms, are manufactured by advanced purification techniques. Nevertheless in these crystals the impurity content is the controlling factor for many properties. Since comparable amounts of imperfections are introduced by relatively small irradiation doses, silicon is, and semiconductors in general are, very sensitive to irradiation. Many properties, like conductivity, Hall effect, optical absorption, photoconductivity, electron spin resonance, recombination lifetime, are easily affected by irradiation. In turn all these properties may be used to study the effects of irradiation on semiconductors.

It has been the purpose of the work described in this chapter to investigate the effects of irradiation on lithium drifted p-i-n junctions in silicon. More specifically, the kinetics of defect interactions and the identification of the defects involved in these interactions are the subjects of the research to be reported on.

In our first experimental approach the effect of gamma irradiation on lithium drifted p-i-n junctions was studied. It was found that by the irradiation space charge is produced in the depleted region of the reverse-biased junction. This space charge is due to some irradiation produced ionized impurity. Before the irradiation the intrinsic region of the p-i-n junction is very well compensated, the net concentration of the electrically active impurities being less than 10^{10} atoms/cm³, or less than 2×10^{-18} expressed in lattice site fraction. Although the semiconductor silicon in general is already a

sensitive material for irradiation effects, the compensated intrinsic regions existing in p-i-n junctions, are still more sensitive. Small amounts of donor-like or acceptor-like ionized impurities may be detected by their effect on junction behaviour. At these low concentration levels the defects will be separated far apart and behave as individuals. This has the advantage that the interaction of defects, for instance complex formation, will follow simple first order kinetics.

Among the junction parameters which are affected by the gamma irradiations are the potential distribution in a reverse-biased junction region, the junction width and junction capacity. These quantities were used as experimental tools for our study of irradiation effects in lithium drifted p-i-n junctions. Details of the methods of measurement and the results of these experiments are described in paragraph 3.3.

It was soon realized that defect behaviour was too complicated to be understood on the basis of the results of the junction experiments alone. Therefore, additional experiments, closely related to our subject-matter, were started. In one of these, lithium compensated intrinsic silicon, made by the lithium ion drift process, was isolated by removing the p- and n-type layers of the p-i-n junction. Resistivity and Hall effect measurements were performed on these homogeneous samples, in which typical device effects are absent. Before irradiation a high resistivity near the intrinsic value is measured. After gamma irradiation the sample is converted to extrinsic silicon by the production of irradiation defects. Carrier concentration measurements as function of temperature by the Hall effect then yield the electronic levels associated with the defects. These experiments, analogous to those discussed in paragraph 1.3, but more complicated, are very useful by supplying more information characteristic for the defects. A description of the sample preparation, the method of measurement, and the results of this second type of experiments, using uniformly lithium compensated silicon, is given in paragraph 3.4.

In the existing literature on radiation defect interactions the impurities boron and oxygen are often dealt with. Much less literature data are however available concerning the more uncommon impurity lithium. It was therefore considered worthwhile to make a special study of the role of lithium in the irradiation behaviour of

silicon. For this purpose heavily lithium doped silicon samples were prepared. In these samples the concentration of lithium is at least about two orders of magnitude larger than that of any other chemical impurity. It may then be expected that the lithium impurities will have a dominant influence on the formation of secondary irradiation defects. The irradiation effects in this simple system should be relatively easy to be understood. Because of the increased amount of impurities present in these crystals a matched irradiation dose has to be correspondingly larger. Since the required dose may not be obtained from gamma ray sources these samples are irradiated with accelerated electrons. As made clear in the next paragraph electrons are rather similar to gamma's as far as defect production is concerned. Our third type of experiments was carried out using these strongly lithium doped samples. These measurements included resistivity, Hall effect and electron spin resonant absorption. Details on sample preparation and results of the experiments are communicated in paragraph 3.5.

3.2 Irradiations

3.2.1 Gamma irradiation

In all our gamma irradiations, except one, the gamma rays of a ^{60}Co source were employed. In one dominant process the radioactive ^{60}Co nucleus decays, with a half life of 5.27 years, by emission of a 313 keV electron. This process forms the ^{60}Ni nucleus in an excited state, which by a cascade transition of two E2 gamma's of 1.332 and 1.173 MeV respectively reaches the stable groundstate. The emitted electron is of no importance for creation of irradiation effects since it is readily absorbed in the source itself or its container. Only the energetic penetrating gamma's will create damage in a remote sample. Gamma rays interact with matter mainly by three types of processes, namely the photoelectric effect, Compton scattering and pair production. In the case considered here, the interaction of the 1.173 and 1.332 MeV ^{60}Co gamma's with silicon, the cross section for the Compton process is by far the highest. The intensity I of the beam in the silicon sample is given by $I(x) = I(0) \exp(-\alpha x)$. In this expression α is the absorption coefficient; for gamma ray energies near 1.25 MeV in silicon about equal to 0.15 cm^{-1} . Since the thickness of the irradiated samples is 0.25 cm only nearly 4 % of

the photons is scattered out of the beam and a beam of almost constant intensity passes through the sample. To improve the uniformity of the integrated gamma flux and of irradiation defect production the sample is turned over right in the middle of the irradiation time. In the Compton process, which is an elastic scattering event between a photon and an electron, kinetic energy is transferred to the electron. A continuous spectrum of energies is produced. Recoil electrons have the maximal energy if the photon is backscattered. This maximal energy of the electrons, the Compton edge, is given by:

$$E_{e, \max} = \frac{2E_{\gamma}^2}{m_e c^2 + 2E_{\gamma}},$$

where $m_e c^2$ is the rest mass energy of the electron, equal to 511 keV. In the present case the Compton edges lie at 1.11 and 0.96 MeV for highest and lowest ^{60}Co gamma ray energy respectively. Because of the anisotropy in the angular distribution of Compton electron energies, the most energetic electrons are scattered forward, in the beam direction. These energetic electrons will be more efficient in damage production. Therefore, if no precautions were taken, the skin layer of the sample would be relatively spared and non-uniform damage will be produced. To avoid this the sample is enclosed into an aluminium box. Aluminium, the neighbour element of silicon in the periodic table, has nearly equal stopping power and cross section for the Compton process. The box has a wall thickness of 2.5 mm, a little larger than the range of the most energetic Compton electron. This ensures a uniform density and energy distribution of electrons inside the box.

Primary defect production will be brought about by collisions between Compton electrons and silicon atoms of the crystal lattice. A maximum of recoil energy is imparted to a silicon atom in a head-on collision. It is given by the relativistic equation

$$E_{\text{Si}, \max} = \frac{2(E_e + 2m_e c^2)E_e}{m_{\text{Si}} c^2},$$

in which m_e and m_{Si} are the masses of the electron and silicon nucleus respectively. A certain minimum amount of energy has to be transferred to the silicon atom to produce the Frenkel defect. This threshold, about 13 eV in silicon, represents an average over easy

$\langle 110 \rangle$ and $\langle 111 \rangle$, and difficult $\langle 100 \rangle$ lattice directions for the displacement process^{40,41}. According to the formula electrons with energy below 150 keV are incapable to create the Frenkel defect. Only the part in the Compton spectrum between 150 keV and the Compton edge is active in damage production. A calculation of the cross section for the atomic displacement process has been made by CAHN⁴². These calculations involve integrations over the partial cross section for all electron energies in the Compton spectrum, for the energy variation of the Compton electron along its range, and also take into account the possible production of other atomic displacements by an energetic primary recoil. For silicon, assuming a displacement threshold of 13 eV, a total cross section of 0.5×10^{-24} cm²/atom is calculated, which means that an incident fluence of 1 γ /cm² produces a primary defect concentration of about 2.5×10^{-2} defects per cm³. These values are one order of magnitude larger than those observed in experiments. The discrepancy is probably associated with extensive relaxation of the defect configurations.

Some details on the irradiations actually carried out are now given. In the first experiment use was made of the 8 Curie ⁶⁰Co source of the "Instituut voor Kernfysisch Onderzoek". For all subsequent ⁶⁰Co irradiations the stronger source of the "Antoni van Leeuwenhoekhuis" was placed at our disposal. Its strength is not very accurately known, but was estimated once and for all to be 1200 Curie at 1-1-1965. Using a ⁶⁰Co lifetime of 2777 days the source strength was calculated at each irradiation date. In a source with the unit strength 1 Curie 3.7×10^{10} ⁶⁰Co nuclei disintegrate per second. Irradiations were carried out with the silicon sample at liquid nitrogen temperature or near room temperature. The distance from source to sample was between 8 and 12 cm, while the time of exposure varied from 1 to 15 hours. In this way samples received a total dose in the range between 3 and 25×10^{14} γ /cm². Also one irradiation was performed in which the 662 keV gamma from radioactive ¹³⁷Cs was employed. In this irradiation by means of the 2500 Curie source of the "Instituut voor Toepassing van Atoomenergie in de Landbouw" a total dose of 140×10^{14} γ /cm² was given. This was effected by a 12 hour exposure with a distance between sample and source of 5 cm.

3.2.2 *Electron irradiation*

As made clear in the previous section, electrons play an intermediate role in the mechanism of defect production by gamma rays. Very similar effects may therefore be brought about by electron irradiations. Provided the energy of the electrons is high enough, that is above the threshold value of 150 keV for silicon, primary defects of the Frenkel type may be created directly. CAHN⁴² has calculated the cross section for this displacement process by electron-nucleus collisions. For thin samples his results indicate a damage production of 4 to 5 defects/cm³ for an incident fluence of 1 electron/cm² of 1.7 MeV. As compared with gamma's, the defect concentrations which may be realized in electron irradiations, are very much increased. In many experiments, for example our experiments with strongly lithium doped samples, this higher defect production rate is required in order to make the damage observable. In contrast to this advantage, it is impossible to create uniform damage by electron irradiation in samples of large size. Electrons of 1.7 MeV, as used in our experiments, have a range in silicon of 3 mm. To assure a uniform damage distribution throughout the sample its thickness must be kept considerably smaller than this range. Our electron irradiated specimens varied in thickness between 0.18 and 0.22 mm.

Actual electron irradiations were performed at the "Instituut voor Toepassing van Atoomenergie in de Landbouw", using the Van de Graaff accelerator. The beam current density, as measured in a Faraday cup with a defining aperture of exactly 1 cm², was periodically read. The beam has a short term stability better than 10 %, and is readjusted to the set current value from time to time. A sufficiently accurate determination of the dose is obtained by current integration, that is by averaging the measured current values. A scanning device improves the uniformity of the integrated beam intensity. Some heating of the samples occurs due to power dissipation of the beam in the samples. This is kept to a minimum by mounting the samples on a copper plate, which is cooled by running water. In this way the temperature rise is limited to about 10 °C above room temperature. Beam current densities from 3 to 10 $\mu\text{A}/\text{cm}^2$ were used in the irradiations, which were continued from 10 to 150 minutes. Doses varying between 10^{16} and 5×10^{17} electrons/cm² were the result of such irradiations.

3.3 Gamma irradiation damage in lithium drifted p-i-n junctions

3.3.1 Junction capacity measurements

One of the methods employed for determination of the irradiation produced defect density is the measurement of the capacity of reverse-biased junctions. A capacity bridge (E.S.I. 291B) forms the central part of the measuring system which is shown in figure 23.

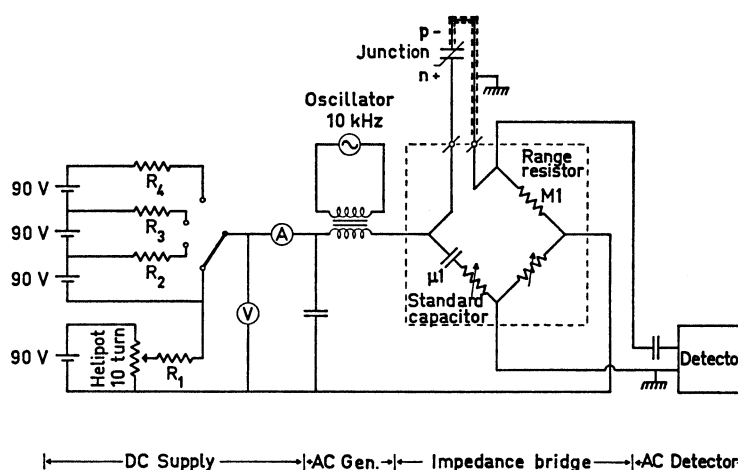


Fig. 23. Circuit diagram showing principal features of the capacity measurement method.

An insulated isolated battery is preferred as the d.c. voltage source, since most line operated power supplies have too high leakage capacitance and enough d.c. current leakage to be objectionable. For protection of the bridge elements series resistors R limit the maximum output power to one Watt. To avoid overloading of the standard capacitor the d.c. voltage may not exceed 300 Volt. For low leakage capacitors the voltage across the capacitor will be equal to the applied voltage as read on the voltmeter V. For junction capacitors corrections are often necessary for the voltage drop across the range resistor of $0.1 \text{ M}\Omega$, which is in series with the capacitor to be measured. As an other correction the diffusion potential is added to the externally applied bias. We used a fixed value 0.5 V for p-n, and 0.8 V for p-i-n junctions as a best estimate of the difference of Fermi level on both sides of the junction.

The junctions, of which the capacity has to be measured, are mounted in a cryostat. Their connection to the measuring system is necessarily made by rather extended leads. By careful shielding of the negative voltage lead, as indicated in figure 23, the parallel capacity of the wiring is kept below 0.05 pF. Corrections for stray capacitance of the junction were applied using a formula due to Kirchhoff. Although this formula is strictly not valid in our case, since the relative permittivity of silicon is different from that of the atmosphere surrounding the junction, the correction was considered to be a good approximation. This was verified by measurements on some control capacitors.

An equivalent circuit adequately representing a reverse-biased junction is rather complicated. It has to include a capacitor C representing the junction capacity, a series resistor accounting for the resistance of the undepleted silicon and possibly of contacts, a parallel resistor to allow for the reverse current either generated in the bulk, or surface leakage current. Also a distributed resistance-capacity chain should be included to represent the effect of surface channels⁴³. By all these disturbing effects the accurate determination of the capacity C belonging to the depleted junction with planar geometry is seriously impeded. Therefore a number of countermeasures were taken. Junction capacities were always measured at lowered temperature, 0 °C or -20 °C. This reduces the reverse junction current appreciably and thus eliminates the parallel resistance. Contributions to the capacity arising from surface inversion layers are minimized by storing the junction in a dry oxygen atmosphere. This was found to decrease the junction capacity and dissipation factor, and to stabilize it⁴⁴. The surface is made slightly p-type by this treatment. Furthermore the surface capacity is reduced by operating the bridge on 10 kHz, which is the highest possible frequency. This shortcuts part of the distributed channel capacity, since the RC-chain essentially acts as a low pass filter. To take the maximum profit of this frequency dependence a still higher frequency, 100 kHz, is to be preferred⁴³. In our case this was unfortunately not possible.

As illustrated in the wiring diagram the 10 kHz oscillator voltage is applied in series with the d.c. bias. Since in general the junction capacity depends on the reverse bias, the oscillator amplitude has to be kept small. Above a reverse bias value of 5 V the oscillator

voltage was set to 0.1 V; below a d.c. bias of 5 V an oscillator voltage of 0.02 V was used. The independency of measured capacity on oscillator amplitude was the criterion for this particular choice.

3.3.2 Irradiation effect on junction capacity

An illustration of the electrical conditions in a reverse-biased p-i-n junction before irradiation is presented in figure 24. Only one dimension x is of interest because of the planar geometry of the junction. In the compensated intrinsic region i no net space charge exists.

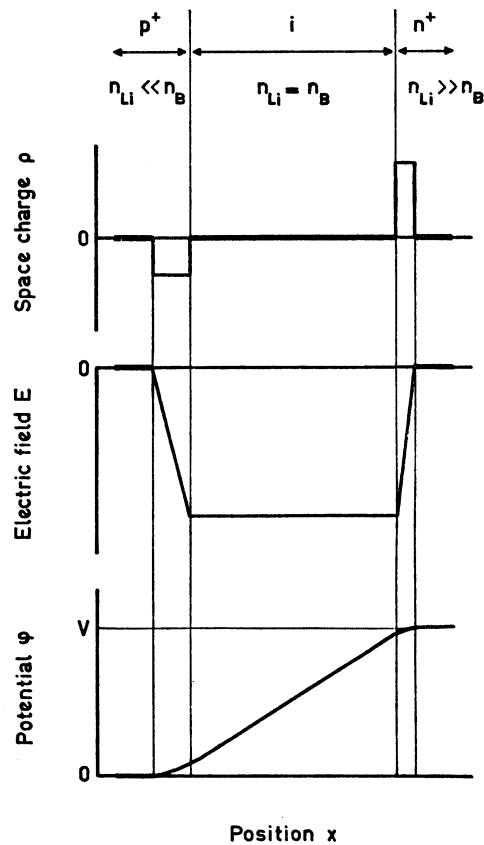


Fig. 24. Schematic of space charge ρ , electric field E and potential ϕ against position x in a p⁺-i-n⁺ junction with reverse bias V ; n_{Li} = lithium concentration, n_B = boron concentration.

As a consequence of the Poisson equation:

$$\frac{d^2\varphi}{dx^2} = -\frac{dE}{dx} = -\frac{\rho}{\epsilon},$$

the electric field is uniform in this region and the potential is a linear function of position. The intrinsic region, whose width is usually 1 or 2 mm, is bounded by two depleted space charge zones, containing equal but opposite charge. These regions are extremely thin; their width increases with the applied reverse bias, but remains less than 1 μm in actual situations. In these circumstances the total junction width is only slightly dependent upon reverse bias. Also the p-i-n junction capacity, given by $C_m = \epsilon A/W_m$, is therefore a constant within experimental error. By measuring the area A of the junction, knowing its thickness W_m from the lithium drift process parameters (section 1.8.3), the capacity may be calculated. In figure 26 this value, constant with respect to reverse bias, is represented by the drawn line a. Typical experimental results are also shown.

By a gamma irradiation electrically active defects are produced, which manifest themselves most markedly by destroying the high degree of compensation in the intrinsic region. After irradiation the p⁺-i-n⁺ junction is converted into a p⁺-p-n⁺ or p⁺-n-n⁺ junction. A new notation p⁺ and n⁺ is introduced to emphasize the much stronger doping of the outer p- and n-type layers in regard to the intermediate former i-region. Since all experimental conditions were adapted in such a way a uniform irradiation doping of the intermediate junction region is expected. Like the common 3- and 5-valent chemical impurities the irradiation produced defects give rise to space charge in a depleted junction zone. Acceptors with levels in the lower half of the gap between valence and conduction band will be ionized and set up a negative space charge. Parallel herewith, donors in the upper half of the forbidden gap give positive space charge⁴⁵. Supposing that negative space charge is created by the irradiation, the electrical conditions in the junction have changed as illustrated in figure 25. A distinction has now to be made between low and high values of the reverse bias. For high values, above a certain marginal value V_m , the p-region of the junction is fully depleted. Still a junction width equal to the intrinsic width of the original p⁺-i-n⁺ junction is realized, again almost independent

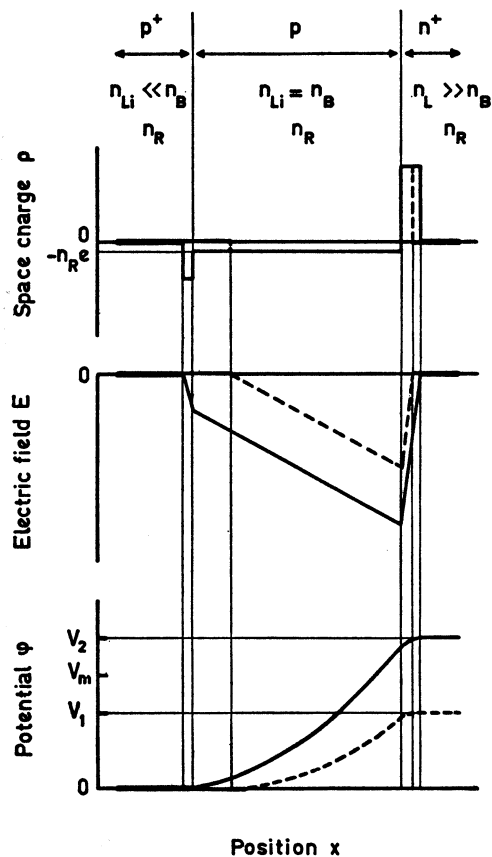


Fig. 25. Schematic of space charge ρ , electric field E and potential ϕ against position x in a p^+-p-n^+ junction with reverse bias $V_1 < V_m$ (dashed lines) and $V_2 > V_m$ (drawn lines); n_R = irradiation defect density.

of reverse bias as long as V remains high enough. For $V > V_m$ the same constant capacity C_m as before the irradiation is measured. At lower reverse bias, $V < V_m$, the p -region is only partly depleted. Because of the uniform doping in the p -region the junction width is expected to increase with the square root of the reverse bias. A capacity dependence C proportional to $V^{-\frac{1}{2}}$ corresponds with this in the voltage range $V < V_m$. A plot of $\log C$ versus $\log V$, as given in figure 26, curves b1 to b4, therefore is a straight line, whose predicted slope $-\frac{1}{2}$ provides a check on the uniformity of space charge. At $V = V_m$ the two branches of the capacity curve join

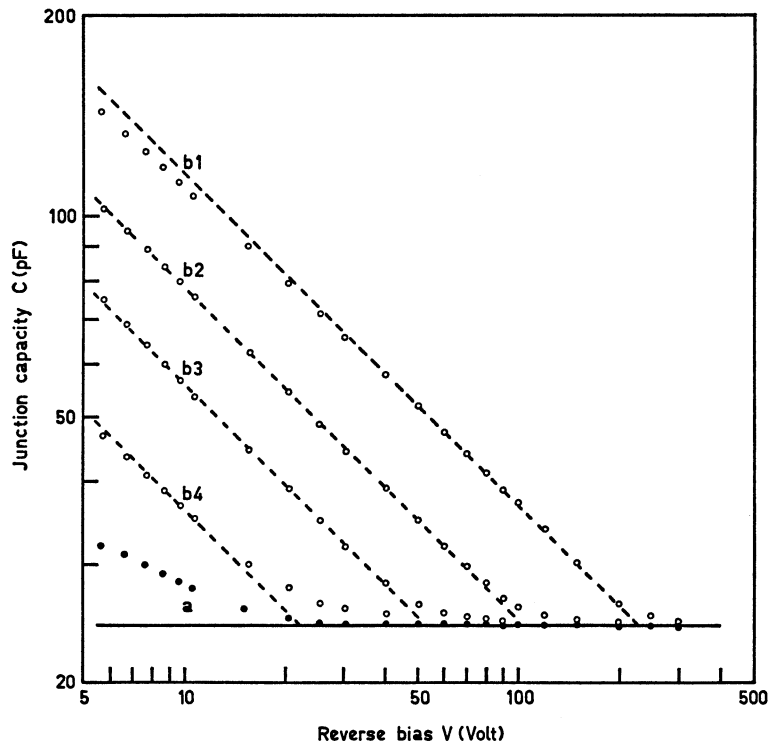


Fig. 26. The capacity C as function of reverse bias V for: a: p⁺-i-n⁺ junction, before irradiation (•), b1 to b4: junction after irradiation (◦). Horizontal drawn line is calculated; dashed lines are drawn with slope $-\frac{1}{2}$ for comparison of experimental results with theory.

with an abrupt change of slope. From the low reverse voltage curve the ionized defect density may be deduced. An expression for this concentration n_R is derived using a Schottky junction model and Poisson's equation. Assuming only singly charged defects the result, valid for $V \leq V_m$, is:

$$n_R = \frac{2C^2V}{e\epsilon A^2}.$$

Since for the low voltage branch of the capacity curve C^2V is a constant this relation also holds for the particular values C_m and V_m . Therefore:

$$n_R = \frac{2C_m^2 V_m}{e\epsilon A^2}.$$

As mentioned before, in section 3.3.1, the junction capacity may be increased by surface channel effects. This will introduce errors in the calculation of n_R , the more while C^2 is involved. Surface channel contributions are present if the junction capacity is not nicely constant for $V > V_m$. In this case always also deviation from the slope $-\frac{1}{2}$ for low reverse bias is observed. We adopted a practical procedure which eliminated surface effects to a large extent. Following this method straight lines were drawn through the experimental points belonging to upper and to lower branches of the capacity curve. The voltage V_m , determined by the intersection of the two lines, proved to be fairly insensitive to the surface conditions. The philosophy behind this procedure was, that, although the capacity may be increased by surface inversion layers, the voltage where the sudden change of slope occurs will not be obscured very much.

A decision whether a p⁺-p-n⁺ or a p⁺-n-n⁺ junction is formed by the irradiation may not be made on the basis of capacity measurements. Only the junction width, not the junction position, is determined by these measurements.

3.3.3 *Time dependence of defect concentration*

The concentration of defects as introduced by the irradiation is not constant. Instead, as the result of defect interactions new types of defects will be created and concentrations will change. By carrying the junction through a recovery procedure the kinetics of such processes were studied. In this procedure the junction was kept at the constant recovery temperature mostly for one hour, or, when required, for exact multiples of hours. Capacity measurements in between the recovery treatments to determine the recovery effect are always performed at a temperature at least 30 °C lower. Corrections were applied to the recovery time for the time spent on cooling or heating the samples.

In the samples irradiated at liquid nitrogen temperature, recovery stages occurring below room temperature could be observed. For instance in the Merck, batch 7, crystals a pronounced interaction process, by which acceptor-like defects are produced, takes place around -40 °C. At this temperature a time constant of 12 hours is associated with this process, and the activation energy was deter-

mined as (0.73 ± 0.05) eV. Also in Merck, batch 7, samples, after ^{137}Cs gamma irradiation, a drastic decrease of reverse current is measured in the temperature range from -60 to -40 °C. This seems to indicate the disappearance of a generation-recombination centre, which, however, is only accompanied by a slight increase in the ionized defect density. Since in other samples hardly any low temperature observations were made these data are too less correlated to base a model on it. Moreover, in the temperature interval from -100 to -60 °C sometimes very clear trapping phenomena were detected. In these cases the capacity varied as function of time, with a time constant of several minutes, due to carrier trapping or untrapping in some defect level. A different capacity-voltage curve is then found when measured from low to high, or from high to low values of reverse bias. Some of the lowest temperature data are rather unreliable by this effect.

In view of all these facts only the defect interaction processes which take place near room temperature will be reported on more extensively in the following text. If junctions are left without reverse bias during the recovery process an appreciable increase of space charge is always observed in the room temperature range. This increase may be described reasonably well by the expression:

$$n_{\text{R}}(t) = n_{\text{R}}(\infty) \left\{ 1 - \exp\left(-\frac{t}{\tau_{\text{LiR}}}\right) \right\}, \quad (1)$$

which forms a solution to the differential equation:

$$\frac{dn_{\text{R}}}{dt} = G(t) = G(0) \exp\left(-\frac{t}{\tau_{\text{LiR}}}\right).$$

In these formulae n_{R} represents the observable defect concentration, G the defect generation rate, and τ_{LiR} a time constant involved in the relevant interaction. If, however, reverse bias is applied across the junctions during the recovery time, instead of increase, a decrease of defect concentration is brought about. To take account of this fact a compensating term $-n_{\text{R}}/\tau_{\text{C}}$ is introduced in the above equation for the defect variation rate. The equation then reads as:

$$\frac{dn_{\text{R}}}{dt} = -\frac{n_{\text{R}}}{\tau_{\text{C}}} + G(0) \exp\left(-\frac{t}{\tau_{\text{LiR}}}\right).$$

It has for its general solution:

$$n_R(t) = \left\{ n_R(0) - \frac{G(0)\tau_C\tau_{LiR}}{\tau_{LiR} - \tau_C} \right\} \exp\left(-\frac{t}{\tau_C}\right) + \frac{G(0)\tau_C\tau_{LiR}}{\tau_{LiR} - \tau_C} \exp\left(-\frac{t}{\tau_{LiR}}\right). \quad (2)$$

For the special case $\tau_C = \tau_{LiR}$ this transforms to:

$$n_R(t) = \{n_R(0) + G(0)t\} \exp\left(-\frac{t}{\tau_C}\right). \quad (3)$$

A necessary condition for the space charge compensation in the junction is the application of a reverse bias large enough to deplete the entire junction. If a reverse bias $V < V_m$ is applied only in the

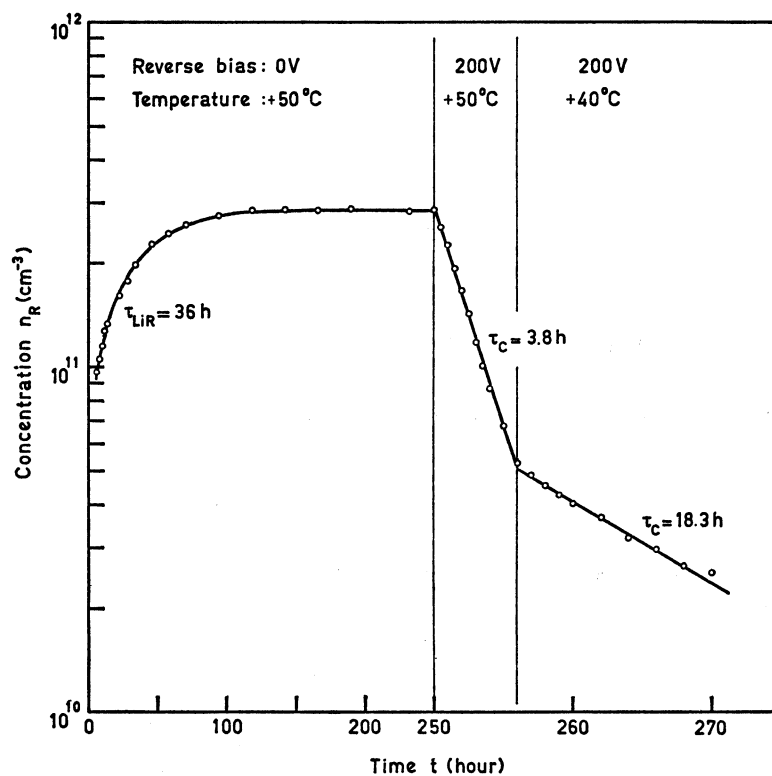


Fig. 27. Variation of defect concentration in sample Texas Instruments, 2, 1 as function of time under various conditions of temperature and reverse bias. Note change of time scale at $t = 250$ hour. Drawn lines are calculated using the formulae (1) or (2), and the stated values for the time constants.

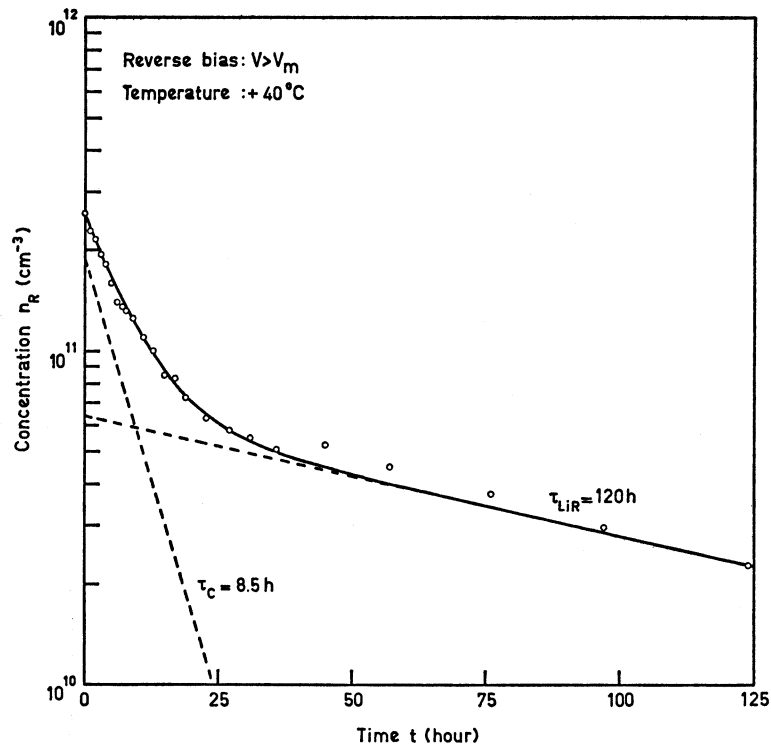


Fig. 28. Variation of defect concentration in sample Texas Instruments, 1, 11 as function of time in the reverse-biased junction. Drawn line is calculated by using formula (2).

depleted volume of the junction, where an electric field is present, the space charge decreases. On the other hand any value of reverse bias above V_m will start the compensation process equally well. This was all verified by experiments.

The figures 27, 28 and 29 are illustrations of the time dependence of the irradiation defect concentration in three slices. In the first figure no reverse bias is applied initially; the space charge rises rapidly and reaches a saturation value in qualitative agreement with formula (1). Having established saturation the defect generation rate has dropped to zero. Application of reverse bias then results in purely exponential decrease of space charge, which is faster at $50\text{ }^\circ\text{C}$ than it is at $40\text{ }^\circ\text{C}$. In the case illustrated in figure 28 the junction is immediately reverse-biased. The observed decrease of n_R is now

analysed in the sum of two exponential functions as dictated by formula (2) and indicated by the dashed lines in the figure. An example of the special case $\tau_c = \tau_{LiR}$ is shown in figure 29. Drawn lines are calculated by using the relevant formula substituting parameter values which give a best fit. Twelve experiments of this type were performed, which differed with regard to the temperature of irradiation, the impurity content of the crystals or the recovery procedure. Frequently, temperature changes were included in the recovery treatment, as is the case in figure 27, to determine an activation energy in one experiment. All results were analysed using the aforementioned formulae. In this way values were obtained for the defect concentration, the generation rate and the time constants. In a later paragraph 3.6 the results are given and discussed quantitatively.

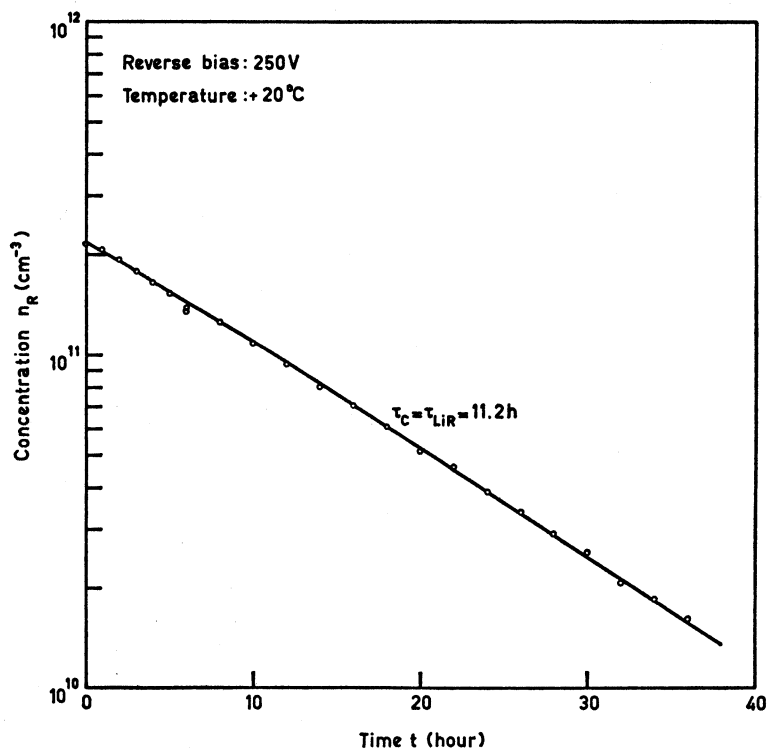


Fig. 29. Variation of defect concentration in sample Wacker, 2, 3 as function of time in the reverse-biased junction. Drawn line according to formula (2) is least squares fitted to the experimental points.

3.3.4 Potential probe measurements

Capacity measurements are, as mentioned, incapable of establishing the donor or acceptor character of the imperfections introduced by the irradiation. To remove this ignorance an experiment was carried out in which the electrostatic potential distribution in a reverse-biased junction was determined. These potential measurements were made along a lateral face of a slice, traversing the junction from the p⁺- to the n⁺-type regions. The principle of the method is easily explained by referring to Poisson's equation: $d^2\varphi/dx^2 = -\rho/\epsilon$. If positive space charge exists in a depleted junction region, $\rho > 0$, the curve φ versus x will be a convex one, showing negative curvature. As opposed to this, for negative space charge a concave curve, with positive curvature, will be observed. An illustration of the method is already given in the figures 24 and 25. Before irradiation, in a well compensated p⁺-i-n⁺ junction no net space charge is present in the intrinsic region ($\rho = 0$) and the potential φ depends linearly on the position x (figure 24). After irradiation the uniform space charge $-n_R e$ in the former i-region gives rise to a quadratic dependence of φ on x (figure 25). Some results of these experiments are shown in figure 30. Curve a is measured before, curve b after a gamma irradiation. From the figure it is concluded that the irradiation produces a curve with positive curvature, therefore negative space charge, a p⁺-p-n⁺ junction, and a net amount of acceptor-like defects.

For these experiments the circular slice, already with the p⁺-i-n⁺ junction prepared in it, was cut into two halves. Potential measurements are made on the flat side face of the semicircular slice following various trajectories and also for various values of reverse bias. A sharp spring loaded needle is used to contact the silicon surface. Because of the high electrical impedance of a reverse-biased junction a compensation method was adopted, with a sensitive galvanometer as the null detecting instrument (Keithly 150 A, Kipp Microva AL 4).

Rather extreme difficulties were encountered in these experiments again due to surface properties. The potential probe method, which essentially measures the potential on the semiconductor surface, proved to be very sensitive to surface conditions. A clear demonstration of surface treatment effects is given by curve c of figure 30, which is measured on a p⁺-i-n⁺ junction after etching in a standard

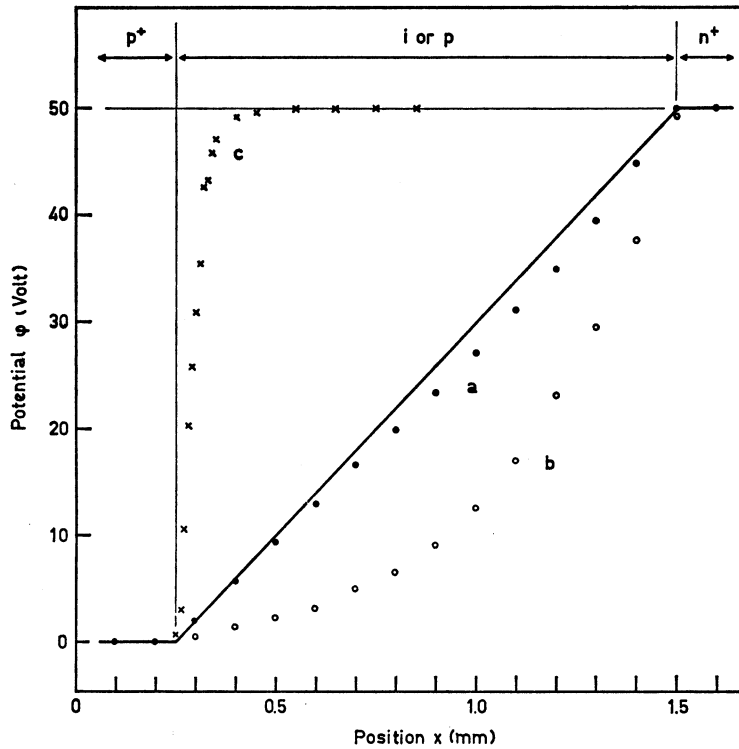


Fig. 30. Potential ϕ against position x in a reverse-biased junction; a: p⁺-i-n⁺ junction before irradiation (\bullet), b: p⁺-p-n⁺ junction after irradiation (\circ), c: p⁺-i-n⁺ junction immediately after etching (\times). Heavy straight lines are theoretical for p⁺-i-n⁺ junction.

mixture HF : HNO₃ : CH₃COOH = 2 : 2 : 5. An n-type surface layer extends over the whole intrinsic junction thickness. Storage of the junction for some weeks in dry oxygen removes the n-type layer and produces a reasonably straight $\phi(x)$ curve. Junctions, which had undergone this rectifying surface treatment, invariably showed conversion to p-type by an irradiation.

The potential measurements also allow a determination of the absolute value of the space charge and a comparison with the results of capacity measurements. Quite distinct results, differing by some factor 2, are then found. It raises the question which of the two methods is to be considered as unreliable. This question is answered, in favour of the capacity measurements, in the next section.

3.3.5 Particle detection by irradiated junctions

For the investigation of particle detection properties of the gamma irradiated junctions a p^+i-n^+ junction was prepared with an intrinsic thickness W_m of 2230 μm . Since the slice thickness of this detector is about 2400 μm , the thickness of the p^+ -type layer in the completed p^+i-n^+ junction is only small and given by (35 ± 10) μm . In all particle detection experiments, particles were incident perpendicular on the p^+ -side of this small-window counter. A determination of the junction character is made possible by these particle detection measurements.

If by the irradiation the p^+i-n^+ junction is converted into a p^+p-n^+ junction, then the transition from p - to n^+ -type silicon is located at the back of the detector. For a reverse bias $V < V_m$ the sensitive detector thickness has decreased to $W = W_m (V/V_m)^{\frac{1}{2}}$. The remaining thickness $W_m - W$ of p -type material is undepleted and represents an additional window layer joining the small p^+ -type window in front of the detector (figure 25). If large reverse bias, $V > V_m$, is applied the junction is fully depleted to the thickness W_m and no extra window exists. On the other hand, when a junction of p^+n-n^+ character is produced by the irradiation, the transition from p^+ to n -type occurs behind the p^+ -type window. Again, for a reverse bias $V < V_m$ the depleted junction thickness is given by $W = W_m (V/V_m)^{\frac{1}{2}}$ and the junction capacity $C = \epsilon A/W$ is equal to the capacity in the case considered above. However, the junction location is different. The insensitive layer of thickness $W_m - W$ is now at the back of the detector and does not add directly to the p^+ -type front window. For large bias, $V > V_m$, the junction thickness is again equal to W_m ; no extra insensitive layer is present and for both junction characters the situation is also indistinguishable by particle detection. On summarizing, for small values of the reverse bias, $V < V_m$, an insensitive region is created in the detector, which, depending on whether the junction has p^+p-n^+ or p^+n-n^+ character, is located in front or in the back of the detector.

Since the existence and location of insensitive layers is open to experimental test by particle detection, such investigations were carried out. In the first type of these experiments we used α -particles from radioactive sources, which were the 5.45 MeV α -particles from ^{241}Am , and the 6.06 and 8.78 MeV α -particles emitted by ^{212}Pb . The

ranges of the particles in silicon, respectively 27, 31 and 55 μm , are small compared to the maximal detector thickness $W_m = 2230 \mu\text{m}$. Before irradiation of the junction the particles could be detected over a large voltage range. When the α -particles do not penetrate directly into the sensitive detector region, their detection is still possible by diffusion of electrons to this region. For large reverse bias, $V > V_m$, particle detection is nearly unaffected by the irradiation. If the junction is converted into a p^+p-n^+ structure by the irradiation, a front window layer will develop as soon as $V < V_m$, which prohibits further particle detection. For a p^+n-n^+ junction also an insensitive layer will exist for $V < V_m$, but then located in the back of the detector. Since the α -particles do not even reach this region this will remain unobserved and no marked peculiarities will occur in passing V_m .

In figure 31 results of measurements before and after irradiation, for all types of mentioned α -particles, are shown. The window

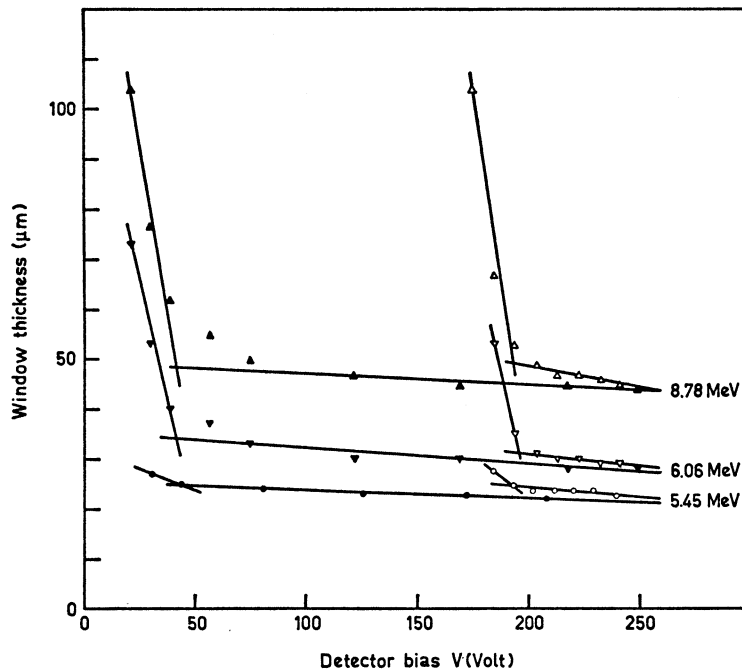


Fig. 31. Window-thickness observed by detection of α -particles from radioactive sources in a p^+i-n^+ junction before irradiation (filled-in graphical symbols) or in a p^+p-n^+ junction after irradiation (open symbols).

thickness is calculated from the detected particle energy using a similar range-energy relation as in paragraph 2.2, but adapted to the present energy range. Corrections were applied for the diffusion contribution to the pulse height, resting on some unpublished data on this subject. From figure 31 the conclusion is drawn that a p^+-p-n^+ junction is produced by the irradiation. If the transition from p^+ to p -type material is not very sharp, which seems to be the case, some arbitrariness is introduced into the determination of V_m . In the present method any small decrease of junction width is readily observed by the much larger relative increase of window layer thickness. A value for V_m on the high side is therefore measured by the α -particle probing method. Also the rather high lower limit for particle detection in the pre-irradiation case is explained by these arguments.

In actual experiments pulses were made visible on an oscilloscope screen (Tektronix 515A), on which pulse heights could be easily read. Linearity was checked, and energy calibration was made by means of a gold-coated surface barrier detector. An integrating and differentiating network, both with a time constant of $0.5 \mu s$, were used for pulse shaping.

A more detailed study, with the same purpose of determining V_m and the junction character, was made by detection of 26 MeV deuterons and 52 MeV α -particles. Because of their large range in silicon, 1960 and 1020 μm respectively, these particles penetrate deeply into the detector volume. This allows measurements to be made of the dependence of detected energy on reverse bias in the interesting range $V < V_m$. Results of such measurements for deuterons are given in figure 32. Drawn lines in this figure are calculated assuming a value for V_m and a p^+-p-n^+ or p^+-n-n^+ junction. Calculations are based on an empirical range-energy relation, from which an expression for dE/dx , the energy loss per unit length, is derived as made clear in paragraph 2.2. To account for a diffusion contribution to the signal height the calculated depleted junction thickness is increased by 60 μm . A best fit of calculations and measurements proves the existence of a p^+-p-n^+ junction, while also V_m is determined within a few percent. In the α -particles measurements the detected energy was up to 20 % too high over part of the voltage range. This is as yet not understood, but in no way invalidates the conclusions based on this work.

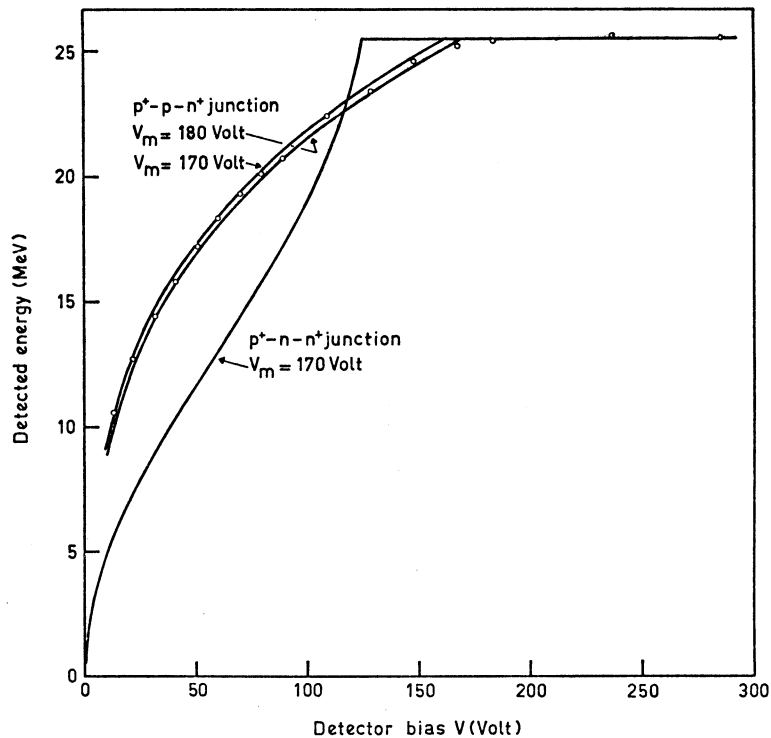


Fig. 32. Detection of 26 MeV deuterons by an irradiated junction. Experimental points: o. Drawn lines are calculated.

Experiments were performed at the "Instituut voor Kernfysisch Onderzoek" with an external beam of the synchrocyclotron. Particles were scattered on the detector by a gold target. A pulse shaping network with a time constant of 1 μ s was used. The detected particle peaks, broadened by the statistical nature of the absorption process, were recorded on a multichannel analyser (Nuclear Data ND 130). The linearity of the detection system was checked and its zero level channel was determined with a mercury pulser.

In conclusion a comparison is made between values of V_m as found by the various methods. In table VIII results are given from measurements performed in a period of 13 hours in a time sequence from top to bottom of the table. The slight increase of V_m is a real effect, due to the fact that space charge increased in the junction, which was left most of that time without bias at room temperature. A rather consistent set of values is obtained, giving support to the

TABLE VIII
Determination of the voltage V_m by various methods.

| Method of measurement | V_m (V) |
|--|-----------|
| Junction capacity | 170 |
| ^{212}Pb α -particles 8.78 MeV | 181 |
| ^{212}Pb α -particles 6.06 MeV | 180 |
| ^{241}Am α -particles 5.45 MeV | 179 |
| Cyclotron deuterons 26 MeV | 175 |
| Cyclotron α -particles 52 MeV | 175 |
| ^{212}Pb α -particles 8.78 MeV | 194 |
| ^{212}Pb α -particles 6.06 MeV | 196 |
| ^{241}Am α -particles 5.45 MeV | 193 |
| Junction capacity | 174 |

validity of these methods. Determinations of V_m by means of potential probe measurements have to be considered as unreliable and were consequently discontinued.

3.4 Gamma irradiation damage in isolated lithium drifted silicon

3.4.1 Method of measurement

To advance the understanding of irradiation effects in lithium drifted silicon, additional investigations were felt to be necessary. In the experiments, which will be described in this paragraph, it was our intention to obtain more information on the gamma irradiation effects by measuring conductivity and carrier concentration. Since the geometrical structure of p-i-n junctions is not suitable for resistance and Hall effect measurements, samples of special shape were prepared for this work. Lithium compensated intrinsic silicon may be produced only by using the lithium ion drift mechanism. As the first step in the preparation of a sample, therefore, a p-i-n junction is made, following the methods outlined in paragraph 1.8. For the present purpose the junctions were drifted to a final intrinsic width of at least 2200 μm , in slices with an approximate total thickness of 2500 μm . After junction preparation the thickness of the p- and n-type extrinsic layers is about 150 μm each. To isolate the intrinsic silicon the n- and p-type material is completely removed, over almost the whole junction area. The geometry after

sample shaping is best made clear by referring to figure 33. On both sides of the slice a layer thickness of at least $300\ \mu\text{m}$ is removed, ensuring the complete disappearance of the low resistivity extrinsic regions. Samples are shaped by grinding off the greater part of the silicon, followed by a final etching treatment, or by etching only,

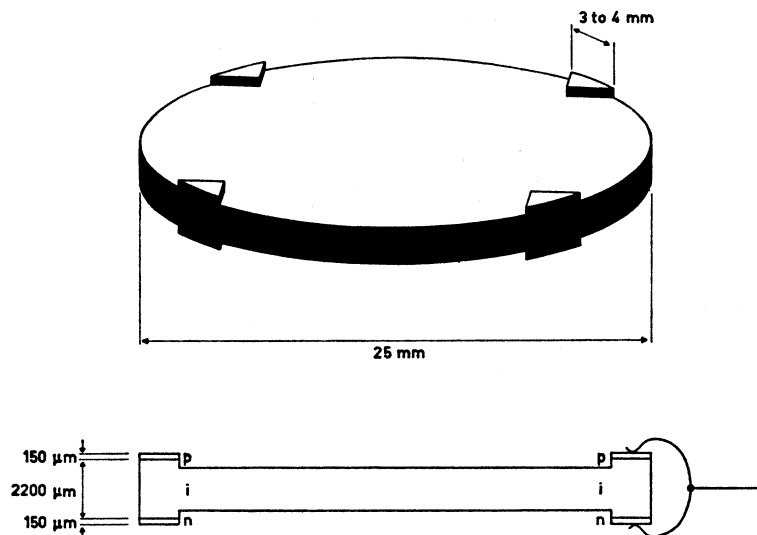


Fig. 33. Illustration of the Van der Pauw method measurements of resistivity and Hall effect on isolated lithium compensated silicon samples.

which avoids any heating during the sample preparation. While etching, the contact areas are protected by covering them with Apiezon wax. As illustrated by figure 33 the p-i and i-n junctions are left at four spots located regularly around the circumference of the slice. These four contacts enable resistivity and Hall effect measurements to be made by the Van der Pauw method. If biased in forward direction the junctions provide good, low resistance electrical contacts to the sample. The present, rather laborious, sample preparation method was adopted to preserve these contacts, which were already made in the early stages using high temperature alloying or diffusion techniques. This was done, since no alternative method was known, by which good contacts could be made to the isolated compensated silicon afterwards.

As mentioned the method developed by VAN DER PAUW⁶ was used for the resistivity and Hall effect measurements. For a discussion

of this method, experimental details and measuring procedure reference is made to the paragraphs 1.3 and 1.4. Samples are electrically connected as indicated in the bottom right hand corner of figure 33. A phosphor bronze spring is clipped around the slice, pressing on both the n- and p-type contacts. Currents will choose the forward biased junction which provides the easiest path to flow into the sample. Measuring currents are taken equal to $1 \mu\text{A}$, or smaller, to avoid carrier injection, which in high resistivity silicon may easily affect the conductivity by raising hole or electron concentration above the thermodynamic equilibrium value. The presence of these phenomena is detected by a dependence of sample resistivity on measuring current, or, in other words, by deviations from Ohm's law. Also to minimize errors due to carrier injection samples of the largest available size were selected for this work. Aside, it may be noticed at this moment, that the conductivity of the p-type region in a forward-biased, 2 mm wide, p^+p-n^+ junction is drastically increased by a double carrier injection process⁴⁶. During all measurements the sample is kept in total darkness.

Immediately after completing the sample preparation always a too low resistance, corresponding to an apparent resistivity of typically $10\,000 \Omega\text{cm}$, is measured. The failure to observe the intrinsic resistivity of $230\,000 \Omega\text{cm}$, is caused by a strongly n-type layer, surrounding the slice, which provides low resistance current paths between the n-type contact spots⁴⁷. As demonstrated by the potential probe measurements, curve c of figure 30, such an n-type surface layer is produced by etching, which is always the last treatment in the sample shaping procedure. Again the surface condition is improved by storage of the slice for some days in dry oxygen. In the same period reverse bias is applied across the sample to accomplish a redrift process. By the combined action of these processes the resistivity of the silicon increases and a final value of $100\,000$ to $300\,000 \Omega\text{cm}$ is achieved. The discrepancy between this final, pre-irradiation, resistivity and the correct value for intrinsic silicon is probably still associated with non-ideal surface conditions and, or, non-uniformity of compensation.

The electrical contacts to the sample have an arc-shaped base width of 3 to 4 mm, and are not very small compared with a slice diameter of 25 mm. Contact width corrections to the resistivity and Hall mobility have therefore to be applied, but unfortunately for

the present geometry no formulae are available. Without contact width correction a Hall mobility is measured at 300 °K, which is 15 to 25 % lower than the correct value of 404 cm²/Vs at this temperature. From this difference a correction factor is obtained, by which the results are modified. The validity of this procedure was verified on a 25 Ωcm p-type silicon slice. On this slice the resistivity was first measured using the small contacts as described in paragraph 1.3. The slice was then shaped according to the present requirements and again measured. Similar large differences in Hall mobility were then observed, which evidently had to be explained by contact size effects.

3.4.2 Time dependence of conductivity

Samples prepared by the method described in the previous section were irradiated by ⁶⁰Co gamma's at a temperature of 40 °C, or of

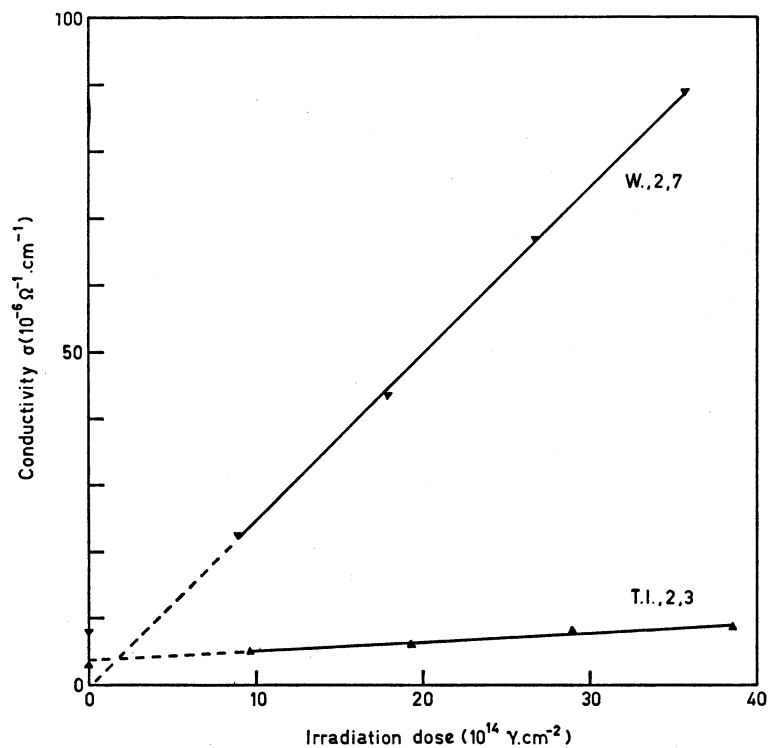


Fig. 34. The increase of room temperature conductivity caused by ⁶⁰Co gamma irradiation at 40 °C of the samples Texas Instruments, 2, 3 and Wacker, 2, 7.

about 0 °C. By the irradiation the near-intrinsic silicon again obtains extrinsic properties. In some of these experiments the irradiation was interrupted a few times to measure the sample conductivity as function of irradiation dose. Results are illustrated by figure 34, which, as anticipated, shows a linear conductivity increase. Since in extrinsic samples the conductivity is given by $\sigma = p e \mu_h$, or by $\sigma = n e \mu_e$, this result implies a constant rate of production of electrically active irradiation defects.

After irradiation, keeping the sample near room temperature, its conductivity continues to increase. This behaviour is similar to the space charge increase, which was observed in junctions left without bias (section 3.3.3). Therefore the present process is described mathematically by the equivalent expressions:

$$\frac{d\sigma}{dt} = \left(\frac{d\sigma}{dt} \right)_{t=0} \exp \left(- \frac{t}{\tau_{\text{LiR}}} \right),$$

$$\sigma(t) = \sigma(\infty) \left\{ 1 - \exp \left(- \frac{t}{\tau_{\text{LiR}}} \right) \right\}.$$

In figure 35 actual experimental results are illustrated by plotting for one sample and for two different recovery temperatures the quantity $p(\infty) - p(t)$ versus time. Carrier concentration is given instead of conductivity to eliminate the temperature dependence of the (hole) mobility. These graphs show the required exponential decrease. Analysis of the results yields the time constant τ_{LiR} at the measuring temperatures, the activation energy of the interaction process, and the saturation defect concentration.

3.4.3 Temperature dependence of hole concentration

To gather more data concerning the irradiation induced conductivity changes, measurements of resistivity and Hall effect were performed over an extended temperature range. As a first immediate result of these measurements the polarity of the Hall effect indicates a p-type conduction in the samples after irradiation. In agreement herewith the Hall mobility μ_H , calculated as the product of Hall coefficient R_H and conductivity σ , and illustrated by figure 36, yields a value characteristic for holes. These results confirm the earlier findings by potential probe measurements (section 3.3.4) and

particle detection (section 3.3.5) in reverse-biased junctions. Little doubt is left therefore that irradiation produces a net amount of defects showing acceptor action.

Calculation of the Hall mobility provides us with a check on the quality of the measurements, which is the reason for plotting this quantity in figure 36. For the expected predominant lattice scattering a temperature dependence of the Hall mobility according to a $T^{-2.3}$ -power law should hold⁹. This temperature dependence, represented by the drawn line in figure 36, is indeed found over the greater part of the temperature range. At the highest temperatures sometimes deviations are observed, which are justified by the onset of intrinsic conductivity. For low temperatures too, the experimental points do not fall on the straight line. In most cases this is caused by ionized impurity scattering, but in some others this is

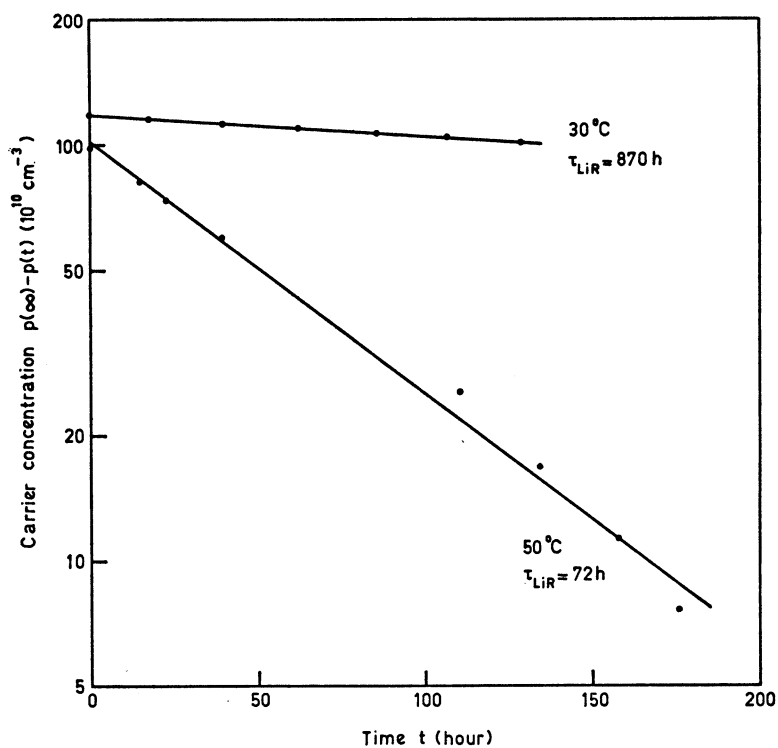


Fig. 35. Variation of carrier concentration in the irradiated sample Texas Instruments, 2, 3 during storage at 30 and 50 °C; $p(\infty) = 130 \times 10^{10} \text{ cm}^{-3}$.

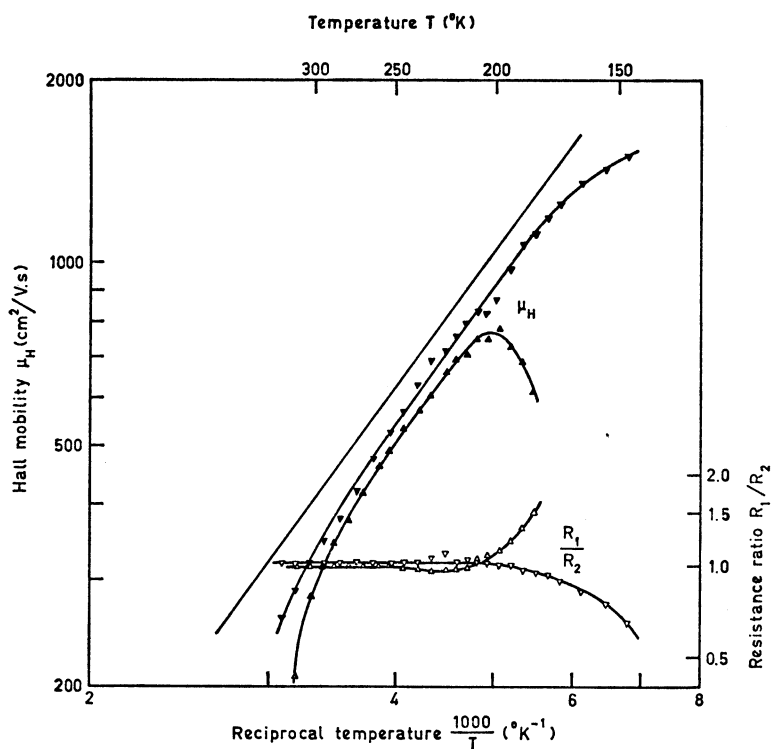


Fig. 36. Hall mobility μ_H before contact width correction in sample Texas Instruments, 2, 3 at some recovery stages after the irradiation (filled-in triangles). The straight line represents $\mu_H = 404 \times (300/T)^{2.3}$. Also the ratio of the Van der Pauw resistances R_1/R_2 is plotted (open triangles).

probably a more serious effect to be explained by a non-uniform impurity distribution. These suspicions are usually confirmed by a plot of the ratio of the Van der Pauw resistances R_1/R_2 , also shown in figure 36. As discussed in paragraph 1.4 any non-uniformity in the sample doping may produce a temperature dependence of this resistance ratio. Low temperature data of doubtful reliability, as indicated by μ_H and R_1/R_2 , were not used in further analysis.

Hole concentrations as function of temperature, derived from the Hall effect, are shown in figure 37. Various curves are given, which belong to different stages in the recovery procedure of one sample. It is amply clear from this figure that electronic energy levels, associated with defects, are introduced by the irradiation. During

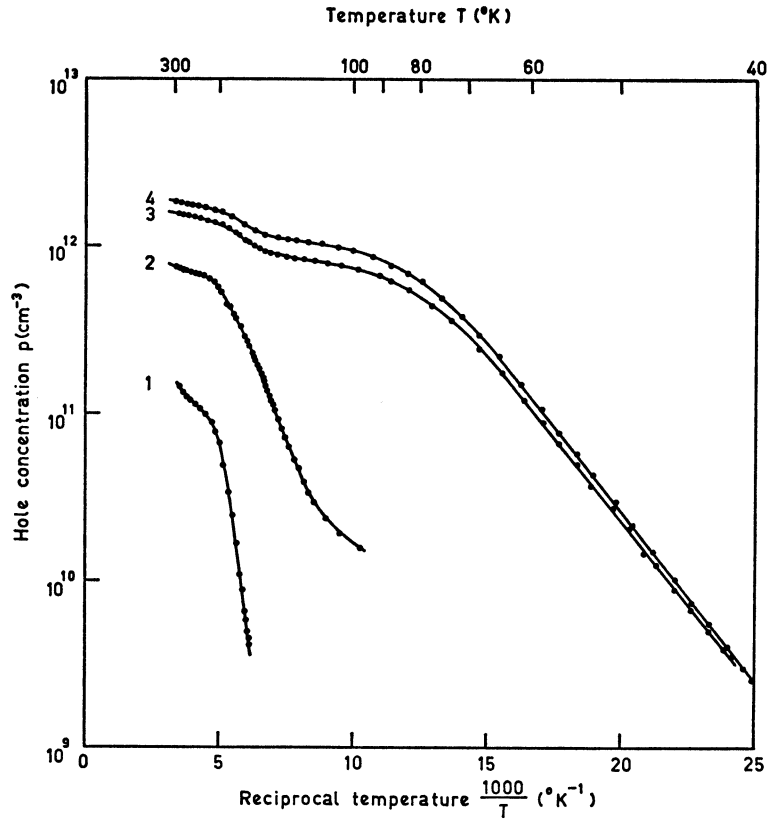


Fig. 37. Temperature dependence of hole concentration after irradiation at 0° C of sample Wacker, 2, 9. Curve 1 is measured immediately after the irradiation, curves 2, 3 and 4 after increasing recovery time.

the recovery treatment the temperature dependence of the electrical properties changes drastically. For the analysis of the measured curves a model was adopted. An electronic level, located E_R above the valence band and associated with an irradiation defect, was introduced as the simplest possible extension of the model considered in paragraph 1.3. To be observable the level at energy E_R , of either donor or acceptor character, should be situated in the lower half of the gap between valence and conduction band. In the p-type silicon, as it exists after irradiation, this part of the zone is probed as the Fermi level moves downwards at decreasing temperature. Electron states in the conduction band will be empty in

p-type silicon; also all lithium donors will be ionized and have given off their electrons. Depending on the position of the Fermi level the boron acceptors may be partly filled. Some electrons will be excited from the valence band, leaving p observable holes in it. Summarizing, in the model we take account of n_{Li} empty donor levels, n_{B} boron acceptor levels at E_{B} , n_{R} irradiation defect levels at E_{R} and p holes in the valence band. To start with, the most likely possibility of conversion of the silicon to p-type by the introduction of acceptor-like irradiation defects is considered. As for the group III chemical acceptors in an elemental semiconductor a spin statistical weight factor $\beta = 2$ is assumed. Applying the condition of electrical neutrality one derives the following equation:

$$p^3 + p^2(n_{\text{Li}} + n'_{\text{R}} + n'_{\text{B}}) + p(n_{\text{Li}}n'_{\text{R}} + n_{\text{Li}}n'_{\text{B}} - n_{\text{R}}n'_{\text{R}} - n_{\text{B}}n'_{\text{B}} + n'_{\text{R}}n'_{\text{B}}) + n'_{\text{R}}n'_{\text{B}}(n_{\text{Li}} - n_{\text{R}} - n_{\text{B}}) = 0, \quad (4a)$$

where, similar as in paragraph 1.3, n'_{R} and n'_{B} are defined by:

$$n'_{\text{R}} = \frac{1}{2}n_{\text{v}} \exp\left(-\frac{E_{\text{R}}}{kT}\right),$$

$$n'_{\text{B}} = \frac{1}{2}n_{\text{v}} \exp\left(-\frac{E_{\text{B}}}{kT}\right).$$

In its general shape this third degree equation is difficult to deal with. However, the fortunate circumstance that the irradiation defect level seems to be located several kT 's above the boron level allows us to bring about useful simplifications.

In a high temperature range, above about 100 °K, the Fermi level will be high enough in the gap to ensure a complete filling of boron levels. Introducing this fact, formulated mathematically by the inequality $p \ll n'_{\text{B}}$, into equation (4a) reduces it to the quadratic expression:

$$p^2 + p(n_{\text{Li}} - n_{\text{B}} + n'_{\text{R}}) + n'_{\text{R}}(n_{\text{Li}} - n_{\text{R}} - n_{\text{B}}) = 0. \quad (5a)$$

For the high temperature end of the high temperature region, which is near 300 °K, also the condition $p \ll n'_{\text{R}}$ will hold. Equation (5a) then further reduces to:

$$p = n_{\text{B}} + n_{\text{R}} - n_{\text{Li}}. \quad (6)$$

In this case the Fermi level is even substantially above the irradiation

tion acceptor level, and both acceptors are ionized. This leads to the above-mentioned constant hole concentration, as is easily visualized by the model. In the p-type irradiated samples the total amount of acceptors exceeds the donor concentration, which means $n_B + n_R > n_{Li}$. On the low temperature end of the high temperature region the situation is more complicated. For the condition $n_{Li} > n_B$, but still $n_{Li} < n_B + n_R$, the Fermi level will be pinned near the irradiation defect level at E_R . Fermi levels may always be calculated from the measured hole concentrations in a straightforward manner by using the equation:

$$E_F = kT \ln \frac{n_v}{p}$$

Because of their illustrative value such a Fermi plot, corresponding with the results presented in figure 37, is given in figure 38. Fermi

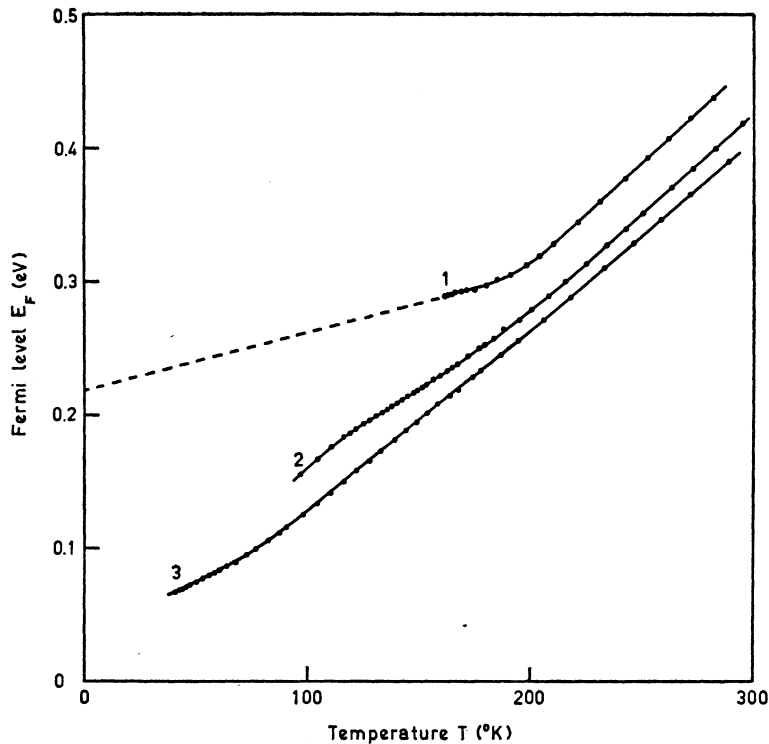


Fig. 38. Temperature dependence of the Fermi level in sample Wacker, 2, 9. Curves correspond to those of figure 37. Curve 4, not shown, nearly coincides with curve 3.

level pinning is observed in curve 1, measured immediately after irradiation, and indicates a defect energy level of $E_R = 0.22$ eV. In the special case $n_{Li} = n_B$ Fermi level pinning will occur at half the irradiation level value. Curve 2 of the figures 37 and 38 is near this condition. Finally for $n_{Li} < n_B$ the low temperature condition may be simply introduced by putting $n'_R = 0$ in formula (5a). One then again obtains a constant hole concentration:

$$p = n_B - n_{Li}. \quad (7)$$

A step-like variation of hole concentration between an upper constant value given by (6) and a lower constant value given by (7) is demonstrated by the curves 3 and 4 in figure 37. Introducing the abbreviations

$$p_{\max} = n_B + n_R - n_{Li} \quad (6a)$$

and

$$p_{\min} = n_B - n_{Li}, \quad (7a)$$

the irradiation defect density is expressed as

$$n_R = p_{\max} - p_{\min}. \quad (8a)$$

Formula (5a) may be rewritten to yield an explicit expression for n'_R ; it then transforms to:

$$n'_R = \frac{1}{2} n_v \exp\left(-\frac{E_R}{kT}\right) = \frac{p(p - p_{\min})}{p_{\max} - p}. \quad (9a)$$

If in the cases 3 and 4 values for p_{\max} and p_{\min} are read directly from the curves, the right hand side of equation (9a) may be calculated for the intermediate temperature interval. Eliminating the $T^{\frac{3}{2}}$ dependence of n_v , one arrives at the result $E_R = (0.23 \pm 0.03)$ eV, in the way as illustrated by figure 39. In the figure the drawn or dashed straight lines represent the theoretical expression $n'_R/T^{\frac{3}{2}}$, calculated by assuming the indicated value for E_R and a density of states hole mass $m_{dh} = 0.55 m_e$.

No pinning of the Fermi level occurs for the curves 3 and 4, and in this case the Fermi level approaches the boron level E_B in a low temperature region, below about 100 °K. For $n_{Li} < n_B$ the low

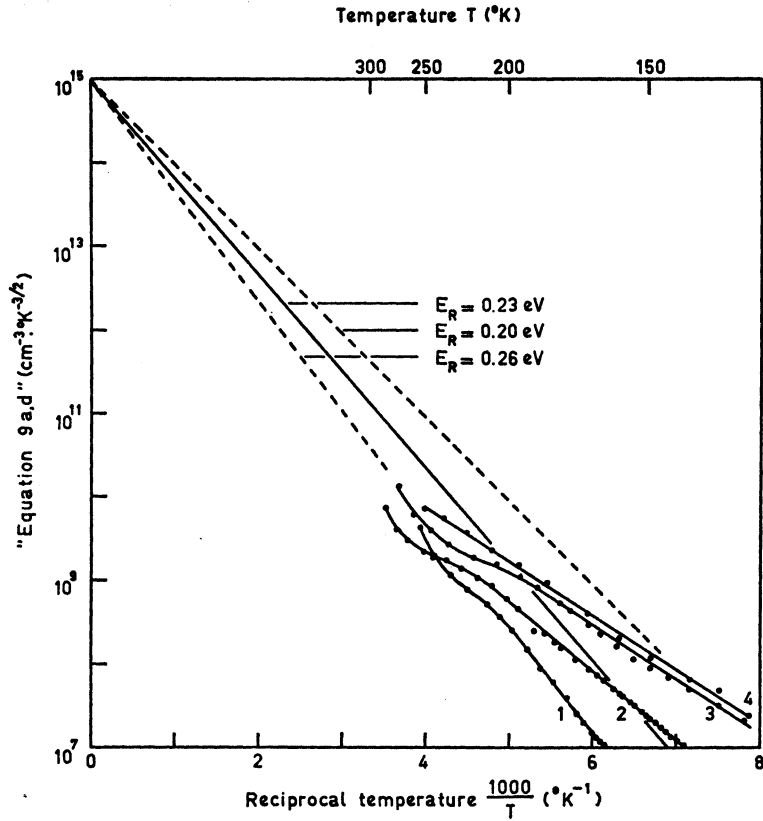


Fig. 39. Illustration of the analysis by equation (9a,d) of hole concentration data in the high temperature range. Curves 1 to 4 are calculated from the expression $p(p-p_{\min})/(p_{\max}-p)T^{3/2}$. Straight lines represent $n'_R/T^{3/2}$ for some values of E_R .

temperature condition $n'_R = 0$ may be substituted at once in equation (4a), which then yields:

$$p^2 + p(n_{Li} + n'_B) + n'_B(n_{Li} - n_B) = 0. \quad (10a)$$

This expression is equivalent to the one given in paragraph 1.3 and fully discussed there. The present case is rather unusual in that the degree of compensation is extremely high. Analysis of the low temperature tails of the curves 3 and 4 indeed yield the boron acceptor level and reasonable values for n_{Li} and n_B . At the high temperature end $p \ll n'_B$, and one obtains $p = n_B - n_{Li}$. Of course,

the curves for the low and high temperature regions join continuously.

In continuing the analysis of the Hall effect data a model was considered in which the irradiation defect level at E_R had donor character. To avoid a lengthy discussion we merely state the result that such phenomena as pinning of the Fermi level if $p_{\min} \leq 0$, the stepwise variation of p in the curves 3 and 4 where $p_{\min} > 0$, and the appearance of the boron level in these cases, are equally well explained by the new model. Formulae were derived on the basis of the donor model. It turned out that, by the introduction of the quantities p_{\max} and p_{\min} , these formulae may be written in a form which applies to both the donor and acceptor case. Results in this donor-acceptor invariant form are given below; the corresponding stage in the previously discussed acceptor model is indicated by the figure in parenthesis:

$$p^3 + p^2(n_B - p_{\min} + n'_B + n'_R) + p(n_B n'_R - p_{\min} n'_B - p_{\max} n'_R + n'_B n'_R) - p_{\max} n'_B n'_R = 0 \quad (4a,d)$$

$$p^2 + p(n'_R - p_{\min}) - p_{\max} n'_R = 0 \quad (5a,d)$$

$$p_{\max} = n_B + n_R - n_{Li} \quad (6a)$$

$$p_{\max} = n_B - n_{Li} \quad (6d)$$

$$p_{\min} = n_B - n_{Li} \quad (7a)$$

$$p_{\min} = n_B - n_R - n_{Li} \quad (7d)$$

$$n_R = p_{\max} - p_{\min} \quad (8a,d)$$

$$n'_R = \frac{p(p - p_{\min})}{p_{\max} - p} \quad (9a,d)$$

$$p^2 + p(n_B - p_{\min} + n'_B) - p_{\min} n'_B = 0 \quad (10a,d)$$

As regards the formal analysis of the p versus $1/T$ curves the donor and acceptor model are not distinguishable. Any decision concerning the donor or acceptor character of the irradiation defect level has to be based on more physical arguments.

There is some indication that the above models are not fully adequate. For instance in curve 1 of figure 37 the hole concentration near room temperature is not very well constant as it should be

according to the formulae (6a) or (6d). Also graphs representing the right hand side expression of (9a,d) point out some errors. If the graphs, shown in figure 39, are extrapolated to the intersection with the $1/T = 0$ axis rather bad values for the effective hole mass are found in many cases. These discrepancies are not very surprising in view of the simplicity of our model, which assumes only one, or at least only one dominant, irradiation defect level. To improve the model a second defect level could be introduced; this however does not seem to be very useful at the present state of the art.

3.5 Electron irradiation damage in heavily lithium doped silicon

3.5.1 Sample preparation

A specific investigation into the interaction between the primary irradiation defects and the chemical impurity lithium was made. For this purpose silicon slices, strongly doped with this impurity, were prepared, following the methods described in this section. In these samples the defect formation capabilities of other impurities are outweighed by the much larger amount of lithium atoms. In the original p-type silicon, supplied by MonoSilicon, the dominant boron acceptor concentration equals $2.3 \times 10^{14} \text{ cm}^{-3}$, corresponding to a sample resistivity of about $58 \text{ } \Omega\text{cm}$. The slices have a diameter of 16 mm; their thickness is 0.25 mm. To start with, a low resistivity n-type skin is produced around the slice by phosphorus diffusion. To this end the silicon slice together with a small phosphorus grain is sealed in an evacuated quartz tube, which is then heated to $1000 \text{ } ^\circ\text{C}$ for 24 hours. By this treatment a very thin, strongly phosphorus doped surface layer is created, which enables better electrical contacts to be made. After this, lithium is introduced into the samples also by a diffusion technique, which employs molten lithium in tin solutions⁴⁸. Our systems were prepared by adding about 1 weight percent of pure lithium (99.9 %, Lithium Corporation of America) to pure tin (99.999 %, Johnson and Matthey). Silicon slices immersed into the melt are n-type counterdoped by a lithium indiffusion at $460\text{--}500 \text{ } ^\circ\text{C}$ during at least two hours, in an argon atmosphere. Depending on the Li-Sn solution composition and the diffusion temperature the slices are then very nearly uniformly doped with 5×10^{16} to 2×10^{17} lithium atoms per cm^3 , which

corresponds to an n-type resistivity of about $0.1 \Omega\text{cm}$. Pyrex tubes⁴⁸ were not found suitable for this work, since they always broke due to a recrystallization process caused by the molten tin. Cylindrical crucibles of pure graphite were taken instead to contain the melt. Next an adherent plate of nickel is deposited on the silicon slice by an electroless method⁴⁹. Four spots near the circumference of the slice are then covered with Apiezon wax. These four spots, shown in figure 40, will provide the electrical contacts in the resistivity and

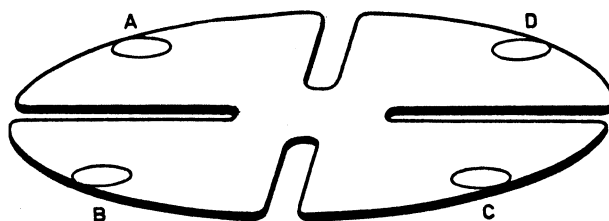


Fig. 40. Illustration of a four leaf clover shaped sample with contact spots at A, B, C and D.

Hall effect measurements by the Van der Pauw method. On the remaining area the nickel plate and also the phosphorus doped skin layer is subsequently removed by etching. To reduce the corrections for the rather large-sized contacts on these small slices, the samples are given a four leaf clover shape. Four radial incisions between the contacts are made by etching away these parts, having protected the other area by Apiezon wax. An illustration of a sample in its final shape is given by figure 40; the thickness of the slices has decreased to about 0.2 mm.

3.5.2 Resistivity and Hall effect

Measurements of resistivity and Hall effect were carried out on these samples both before and after electron irradiation. A discussion on the Van der Pauw method of measurement, details of equipment and measuring procedure is already given in paragraph 1.3. Figure 41 is presented as an illustration of some results. Before irradiation the temperature dependence of the electron concentration is analysed using a model which takes account of electron states in the conduction band, lithium donor levels and compensating acceptors. Since this model is the n-type counterpart of the p-type

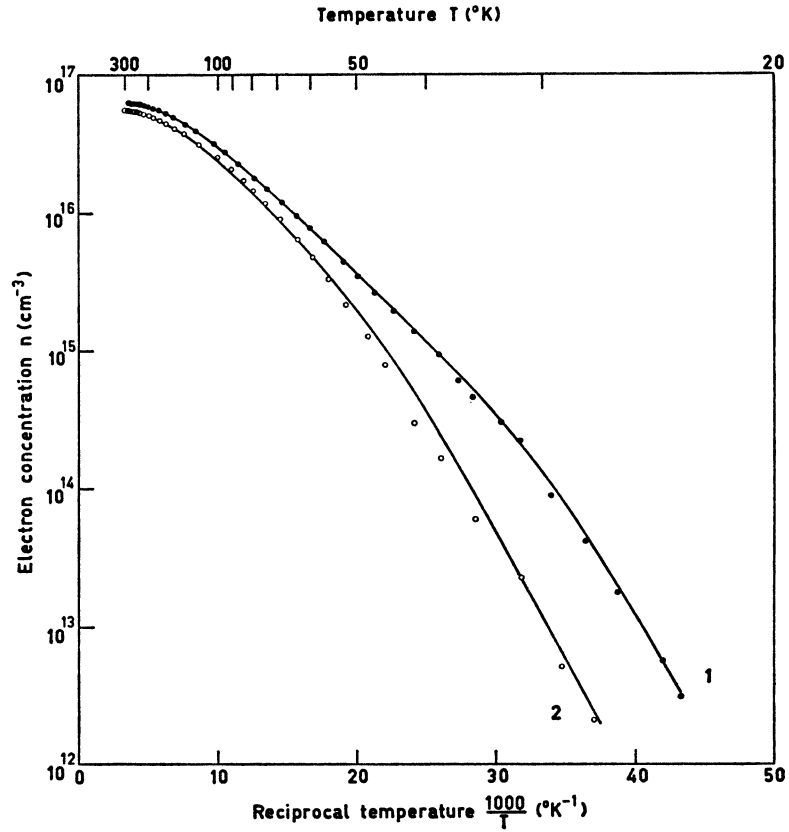


Fig. 41. Temperature dependence of electron concentration before (curve 1) and after (curve 2) irradiation of sample MonoSilicon, 1, 30. Experimental points: •, ◦. Drawn lines are least squares adjusted by computer calculations.

case considered in paragraph 1.3, equivalent mathematical expressions are produced. Consequently, the computer program, mentioned in that paragraph, could be used to perform the analysis on the X8 of the "Mathematisch Centrum". Results are given in table IX. From an examination of the table one concludes that our result for the ionization energy E_{Li} of the lithium donors agrees quite well with the value 33 meV, reported in the literature⁵⁰. In the samples MS, 1, 33 and MS, 1, 34, containing the highest amount of lithium, a slightly lower value for E_{Li} is found. This is explained by some overlap of electron wave functions, by which the donor level broadens to a band. As an other result the table shows a

TABLE IX

Lithium concentration n_{Li} , concentration n_{a} of compensating acceptors, electron energy level of the lithium donor and density of states effective mass $m_{\text{d,e}}$ of electrons for some heavily lithium doped samples before and after electron irradiation.

| Sample | Irradiation dose | n_{Li} | n_{a} | E_{Li} | $m_{\text{d,e}}/m_{\text{e}}$ |
|-----------|-----------------------------|----------------------------|----------------------------|-----------------|-------------------------------|
| — | 10^{16} e/cm ² | 10^{16} cm ⁻³ | 10^{14} cm ⁻³ | meV | — |
| MS, 1, 30 | — | 6.67 | 2.75 | 31.6 | 0.56 |
| | 1.10 | 5.99 | 20.5 | 32.9 | 0.50 |
| MS, 1, 34 | — | 21.2 | 2.97 | 28.7 | 0.58 |
| | 3.08 | 15.6 | 1.07 | 35.4 | 0.79 |
| MS, 1, 37 | — | 11.2 | 2.47 | 31.6 | 0.63 |
| | 1.99 | 9.3 | 2.65 | 36.2 | 0.68 |
| MS, 1, 33 | — | 21.0 | 2.13 | 30.6 | 0.69 |

compensating acceptor concentration around 2.6×10^{14} cm⁻³, independent of the amount of lithium doping. This value nearly equals the boron concentration in the original p-type silicon, stated before as 2.3×10^{14} boron atoms per cm³. However, in the strongly lithium doped samples the boron acceptors perhaps have disappeared by the process of lithium-boron complex formation, discussed in paragraph 1.7. If the KRÖGER-PELL^{30,31} results for the equilibrium constant of this reaction are applicable almost all boron forms part of these complexes. Also according to the values of SPITZER and WALDNER³² the greater part of the free boron acceptor levels is cancelled by this process. Yet, because of the remarkable equality of boron density before, and compensating acceptor density after lithium doping, it is tempting to assume that boron is involved in the creation of the latter acceptor levels. To verify this hypothesis future experiments will be carried out starting from lower resistivity p-type silicon.

By comparing the curves 1 and 2 of figure 41 one concludes that carriers are removed by the irradiation. A rather inevitable element of any explanation for this phenomenon is the disappearance of lithium donors, for instance if by capture of a vacancy a substitutional neutral lithium atom will be formed. In case this explanation holds the old model and formula will still be valid. Also, the samples were relatively lightly irradiated to avoid the formation of complex

defect structures and to favour the applicability of the simple model. Nevertheless, the analysis of measurements of irradiated samples are not as good; the RMS-errors are larger and the best fit parameters apparently have less physical significance. Results obtained on samples after irradiation are also given in table IX.

3.5.3 *Electron spin resonance*

An investigation to the electron irradiation effects on strongly lithium doped silicon, made by the method of electron spin resonance absorption, is briefly discussed now. Lithium impurities, if not ionized, have unpaired electrons and behave as paramagnetic centres in the silicon crystal. Indeed, at 77 and 4.2 °K, electron spin resonance was observed. Our result for the g -factor, $g = 1.9986 \pm 0.0005$, is in agreement with the value to be expected for a shallow donor⁵¹. Consistent with the symmetry of the possible sites of lithium in a silicon lattice an isotropic g -factor was found. Samples used for this work contained near to 7×10^{17} atoms lithium per cm^3 and showed conduction even at liquid helium temperature. It must be admitted therefore, that we are not completely sure whether the observed resonance is due to electrons in bound donor states or to conduction electrons. The small difference in g -factor for these two cases is within experimental error⁵¹. By electron irradiation the intensity of the resonance is drastically reduced. Only partly a related increase in line width is responsible for the reduction in amplitude. The present result is in qualitative agreement with the carrier removal observed by the Hall effect. The experiments were carried out on a X-band superheterodyne spectrometer. A DPPH-sample was used as g -marker and as a reference for the absorption intensities.

3.6 Discussion of the results

3.6.1 *Time constant τ_{LiR}*

In this section we want to prove the hypothesis that the time constant τ_{LiR} is associated with capture of lithium ions by irradiation defects, called R. For this type of diffusion limited pairing reactions, schematically given by $\text{Li}^+ + \text{R} \rightarrow \text{LiR}$, a general expression for the time constant is already mentioned in section 1.7.3. Repeating this

formula in notation adapted to the present situation yields:

$$\tau_{\text{LiR}} = \frac{1}{4\pi\{(n_{\text{Li}}+n_{\text{R}}+K)^2-4n_{\text{Li}}n_{\text{R}}\}^{\frac{1}{2}}D_{\text{Li}}R_{\text{capt}}}$$

Within a certain capture radius R_{capt} the lithium ion is trapped by the irradiation defect, whereas beyond this distance it diffuses around freely. No indications of the trapping process being an equilibrium reaction were observed. Experimentally this was verified by carrying the reaction into saturation and then raising the temperature. It was found that no lithium ions again dissolve in the silicon lattice by the reverse reaction: $\text{LiR} \rightarrow \text{Li}^+ + \text{R}$. In the expression for the time constant τ_{LiR} this fact is entered by putting the equilibrium constant K equal to zero. After every irradiation the density of irradiation defects is lower than $3 \times 10^{12} \text{ cm}^{-3}$, as may be checked by examining the tables XII and XIV. This is much smaller than the total concentration of lithium impurities n_{Li} in all samples. Thus: $n_{\text{R}} \ll n_{\text{Li}}$. Introduction of both these simplifying circumstances into the formula for τ_{LiR} reduces it to:

$$\tau_{\text{LiR}} = \frac{1}{4\pi n_{\text{Li}} D_{\text{Li}} R_{\text{capt}}}$$

In many of the samples, in which investigations of the irradiation effects were carried out, appreciable amounts of boron or oxygen were present. In these cases complex formation of the type $\text{Li}^+ + \text{B}^- \rightleftharpoons \text{LiB}$ or $\text{Li}^+ + \text{O} \rightleftharpoons \text{LiO}^+$ takes place. Only a fraction $\alpha < 1$ of unpaired lithium ions is then free to move through the silicon crystal. This increases the time spent on LiR complex formation and the formula for τ_{LiR} under these conditions reads:

$$\tau_{\text{LiR}} = \frac{1}{4\pi\alpha n_{\text{Li}} D_{\text{Li}} R_{\text{capt}}}$$

where n_{Li} is the sum of the concentrations of Li^+ , LiO^+ and LiB . An experimental verification of the above-mentioned formula for the time constant may be carried through in several ways by variation of the quantities α , n_{Li} or D_{Li} . In various experiments on samples with different lithium, boron and oxygen concentration, and at various recovery temperatures, this dependence was thoroughly checked. Values for τ_{LiR} were obtained from the experi-

ments with lithium drifted junctions, described in section 3.3.3. Also some values for τ_{LiR} resulted from the time dependence of conductivity in the isolated lithium compensated silicon, as discussed in section 3.4.2. It was set forth in detail in preceding discussions how n_{Li} (paragraphs 1.3 and 1.4), the diffusion constant D_{Li} at the relevant temperature (section 1.7.1 and references 26, 27 and 52), and α (sections 1.7.2 to 1.7.4) were determined. As the single unknown parameter the capture radius R_{capt} may be calculated. In table X a survey of the various results is given.

TABLE X
Summary of data on the time constant τ_{LiR} .

| Sample | n_{Li} | Temperature | D_{Li} | α | τ_{LiR} | R_{capt} | Method of measurement |
|-----------|---------------------------|--------------------|----------------------------------|----------|---------------------|----------------------|-----------------------|
| — | 10^{14} cm^{-3} | $^{\circ}\text{C}$ | $10^{-14} \text{ cm}^2/\text{s}$ | — | hour | 10^{-8} cm | — |
| M, 7, 6 | 1.41 | 19 | 1.27 | 0.8 | 450 | 3.4 | cap |
| M, 7, 11 | 1.42 | 30 | 3.26 | 0.84 | 183 | 3.1 | cap |
| M, 7, 13 | 1.39 | 30 | 3.26 | 0.8 | 150 | 4.0 | cap |
| | | 40 | 7.27 | 0.8 | 65 | 4.2 | |
| M, 7, 14 | 1.41 | 50 | 15.4 | 0.8 | 22 | 5.9 | cap |
| | | 30 | 3.26 | 0.8 | 143 | 4.2 | |
| TI, 1, 11 | 1.61 | 50 | 15.4 | 0.8 | 31 | 4.1 | cap |
| | | 40 | 7.27 | 0.48 | 120 | 3.3 | |
| TI, 2, 1 | 6.78 | 20 | 1.39 | 0.026 | 1850 | 4.9 | cap |
| | | 30 | 3.26 | 0.044 | 500 | 4.5 | |
| | | 40 | 7.27 | 0.071 | 160 | 3.9 | |
| TI, 2, 3 | 6.8 | 50 | 15.4 | 0.109 | 36 | 5.4 | cond |
| | | 30 | 3.26 | 0.047 | 870 | 2.4 | |
| TI, 2, 6 | 6.77 | 50 | 15.4 | 0.116 | 72 | 2.5 | cap |
| | | 30 | 3.26 | 0.047 | 700 | 3.0 | |
| W, 2, 3 | 17.4 | 50 | 15.4 | 0.123 | 42 | 4.1 | cap |
| | | 20 | 1.39 | 0.17 | 11.2 | 48 | |
| W, 2, 9 | 16 | 20 | 1.39 | 0.2 | 68 | 7.3 | cond |
| | | 30 | 3.26 | 0.3 | 23 | 6.1 | |

It is seen in this table that fairly large variations in the parameters n_{Li} , D_{Li} and α were introduced. Comparing extreme cases both the lithium concentration and the diffusion constant differed by a factor 12, while α varied by a factor 30. This together resulted

in a variation of the time constant τ_{LiR} by about two orders of magnitude. Leaving aside for the moment some results obtained on Wacker silicon, we notice that in spite of these large variations a rather constant value for the capture radius is found. It follows from this constancy of the capture radius that the applied formula is valid and that the assumed mechanism of precipitation of lithium ions on irradiation defects is really effective. Most results are expressed by $R_{\text{capt}} = (4 \pm 1) \times 10^{-8}$ cm, which is quite reasonable for an interaction process lacking Coulomb attraction. Since the lithium ion carries positive charge the defect R has to be neutral. In the exceptional case Wacker, 2, 3 a rather much larger capture radius is observed. This value may be identified with the Coulomb capture radius, and points to an electrostatic interaction between the Li^+ -ion and a negatively charged R^- irradiation defect.

3.6.2 Time constant τ_c

Continuing the discussion on the time dependence of irradiation induced phenomena we now deal with the time constant τ_c . Observation of this time constant was confined to the experiments with reverse-biased junctions, where it governed the rate of space charge compensation. In this section the proof will be given that τ_c is involved in a space charge neutralization process which operates via the lithium ion drift mechanism. To this object we proceed by deriving a formula for the time constant τ_c in quantitative mathematical terms. Reference is made to figure 25 for an illustration of the behaviour of electrical quantities in a reverse-biased irradiated junction. In a depleted junction region the space charge ρ is related to the electric field E by a Maxwell equation. In our one-dimensional treatment for planar structures this equation, the Poisson equation, reads:

$$\frac{dE}{dx} = \frac{\rho}{\epsilon}. \quad (11)$$

Through their high mobility μ_{Li} lithium ions will acquire a drift velocity $\mu_{\text{Li}}E$ in the electric field existing in the depleted junction region. Since the ions carry unit positive charge this drift motion sets up an electric current, with density J_{Li} , given by the equation

$J_{\text{Li}} = n_{\text{Li}} e \mu_{\text{Li}} E$. Only currents arising from drift in the electric field, and no diffusion contributions are considered in the transport equation. The n- and p-type boundaries of the junction act as source and sink for lithium ions respectively and may be called injecting contacts. Differentiation of the transport equation yields:

$$\frac{dJ_{\text{Li}}}{dx} = n_{\text{Li}} e \mu_{\text{Li}} \frac{dE}{dx}. \quad (12)$$

It has been tacitly assumed that n_{Li} is constant with respect to x . This implies, since n_{Li} is supposed to be equal to n_{B} throughout the junction region, the assumption of uniformly doped material. However, in some experiments it turned out that this requirement is not always sufficiently fulfilled. This then gives rise to observable deviations from equation (14) governing space charge compensation in a reverse-biased uniform junction region. In these cases also no exact compensation of space charge is achieved by the lithium ion drift process. Conservation of lithium ions is expressed by the continuity equation:

$$\frac{dJ_{\text{Li}}}{dx} + \frac{d\rho}{dt} = 0. \quad (13)$$

By elimination of J_{Li} and E from equations (11) to (13) we obtain:

$$\frac{d\rho}{dt} = - \frac{n_{\text{Li}} e \mu_{\text{Li}}}{\varepsilon} \rho. \quad (14)$$

The space charge ρ is due to ionized impurities and is given by $\rho = e(n_{\text{Li}} - n_{\text{B}} - n_{\text{R}})$, where n_{R} represents the net amount of irradiation produced negatively charged acceptors. Any time dependence of the space charge essentially is caused by variation of the lithium concentration n_{Li} . Since however $n_{\text{R}} \ll n_{\text{Li}}$ and $n_{\text{Li}} \approx n_{\text{B}}$, the inequality $\rho = e(n_{\text{Li}} - n_{\text{B}} - n_{\text{R}}) \ll e n_{\text{Li}}$ holds. Therefore, the variations of n_{Li} during the compensation process are relatively small and the factor $\varepsilon/n_{\text{Li}} e \mu_{\text{Li}} \equiv \tau_{\text{C}}$ is almost a constant. After substitution of τ_{C} the differential equation (14) reads:

$$\frac{d\rho}{dt} = - \frac{\rho}{\tau_{\text{C}}}. \quad (15)$$

It has for its solution:

$$\rho(t) = \rho(0) \exp\left(-\frac{t}{\tau_c}\right).$$

In section 1.6.3 the ionic relaxation time τ_c was already met. In that section the time constant τ_c appeared in an expression equivalent to:

$$\frac{dC}{dt} = -\frac{C}{3\tau_c}.$$

This equation controlling the capacity variation of p-n junctions caused by space charge compensation via the lithium ion drift mechanism, is virtually the same as equation (15), valid for p-i-n junctions. The numerical factor 3 is characteristic for the linear impurity distribution in the p-n junction case.

To illuminate the significance of the time constant τ_c two comments will be made. In the first place the expression for τ_c may be rewritten as follows:

$$\tau_c = \frac{W}{An_{Li}e\mu_{Li}} \times \frac{\epsilon A}{W},$$

where A stands for the area, and W for the width of the junction. The leading factor on the right hand side equals the resistance of the junction for electric conductance by lithium ion currents. The second factor is the capacity of the junction. Thus, τ_c is the ionic RC -time of the junction volume, which is the ionic analogue of the dielectric relaxation time, which in electronic processes governs the transient return to equilibrium after any perturbation. For this reason τ_c is designated as the ionic relaxation time.

Secondly, by application of the Einstein relation $eD_{Li} = \mu_{Li}kT$, the mobility may be eliminated from the expression for τ_c , yielding:

$$\tau_c = \frac{kT}{n_{Li}e^2D_{Li}}.$$

Introduction of the Coulomb capture radius R_C , defined by

$$\frac{e^2}{4\pi\epsilon R_C} = kT,$$

modifies the formula to:

$$\tau_c = \frac{1}{4\pi n_{\text{Li}} D_{\text{Li}} R_c}.$$

Evidently, this result is very similar to that obtained for τ_{LiR} in the previous section. An important distinction however is, that in the present case the value of the capture radius R_c is known from theory. If electrostatic attraction exists between interacting impurities Li^+ and R^- , the capture radius R_{capt} is equal to the Coulomb capture radius R_c and also $\tau_{\text{LiR}} = \tau_c$. For this reason this special case was already considered explicitly in section 3.3.3.

For a qualitative check on the validity of the space charge neutralization model we note that the presence of an electric field is indispensable to effect the compensation. To achieve compensation in the whole junction region, $V \geq V_m$ is a necessary and sufficient condition. Application of a lower reverse bias only effects compensation in the depleted junction zone. These predictions, following from the proposed space charge neutralization mechanism, were verified and confirmed by experiments.

To carry through a quantitative check on the validity of the formula for the time constant τ_c , we first incorporate in the formula the retarding effect of impurities to which lithium ions may get bound. If, as in the preceding section, in consequence of LiB or LiO^+ complex formation, only a fraction $\alpha < 1$ of lithium ions diffuses freely through the silicon lattice, the time scale on which space charge compensation occurs is enlarged and τ_c becomes:

$$\tau_c = \frac{\epsilon}{\alpha n_{\text{Li}} e \mu_{\text{Li}}}.$$

As before, from discussions given earlier the lithium concentration n_{Li} (paragraphs 1.3 and 1.4), the unpaired fraction α (sections 1.7.2 to 1.7.4) and the lithium mobility (section 1.7.1 and references 26, 27 and 52) are known. There is therefore no problem in calculating τ_c directly from these data and comparing the results with the experimental values. It may be inferred from table XI, where results obtained on a number of samples are grouped together, that agreement between calculated and measured values of the time constant τ_c is always very good. Variations dictated by changing

the lithium concentration by a factor 12, the fraction of free lithium ions by a factor 20, or the mobility by a factor 20, resulting in a variation of the theoretical τ_c by some factor 30 are always correctly reflected in the experimental result. It is concluded therefore that the formula for τ_c is valid, and that actually the lithium ion drift mechanism is the basic process for the observed space charge compensation.

TABLE XI
Summary of data on the time constant τ_c .

| Sample | n_{Li} | Temperature | μ_{Li} | α | τ_c calculated | τ_c measured |
|-----------|---------------------------|--------------------|-----------------------------------|----------|---------------------|-------------------|
| — | 10^{14} cm^{-3} | $^{\circ}\text{C}$ | $10^{-12} \text{ cm}^2/\text{Vs}$ | — | hour | hour |
| M, 7, 6 | 1.41 | 19 | 0.50 | 0.8 | 32 | 30 |
| M, 7, 11 | 1.42 | 30 | 1.25 | 0.84 | 12.2 | 11.7 |
| M, 7, 12 | 1.42 | 30 | 1.25 | 0.84 | 12.2 | 12.4 |
| M, 7, 13 | 1.39 | 40 | 2.69 | 0.8 | 6.1 | 6.7 |
| M, 7, 14 | 1.41 | 60 | 10.9 | 0.9 | 1.31 | 1.35 |
| TI, 1, 4 | 1.56 | 30 | 1.25 | 0.38 | 24.5 | 22.0 |
| TI, 1, 11 | 1.61 | 40 | 2.69 | 0.48 | 8.6 | 8.5 |
| TI, 2, 1 | 6.78 | 40 | 2.69 | 0.07 | 14.2 | 18.3 |
| | | 50 | 5.53 | 0.11 | 5.2 | 3.8 |
| | | 30 | 1.25 | 0.047 | 45.6 | 48 |
| TI, 2, 6 | 6.77 | 40 | 2.69 | 0.081 | 12.2 | 11.5 |
| | | 50 | 5.53 | 0.123 | 3.9 | 3.6 |
| | | 30 | 1.25 | 0.047 | 45.6 | 48 |
| W, 2, 3 | 17.4 | 20 | 0.55 | 0.17 | 11.1 | 11.2 |
| W, 2, 5 | 15.0 | 20 | 0.55 | 0.25 | 8.8 | 7.9 |

3.6.3 Recovery behaviour of irradiation effect

Having established the significance of the time constants τ_c and τ_{LiR} , the time dependence of the irradiation effect may be discussed now in more detail. To this end we return to the experiments described in section 3.4.3, results of which are illustrated by the curves 1 to 4 of figure 37. In curve 1, measured very shortly after an irradiation at 0 $^{\circ}\text{C}$, pinning of the Fermi level occurs. As shown by figure 38 this points to an irradiation defect level located 0.22 eV above the valence band. Curves 3 and 4 measured after keeping the

sample at 20 °C during 120 hours, and an additional 200 hours at 30 °C respectively. From these curves p_{\max} and p_{\min} are read directly and plots based on equation (9a,d) may be made. As illustrated in figure 39 a level E_R at (0.23 ± 0.03) eV is then found. We conclude that the same irradiation defect level as observed in curve 1 is still present. Moreover, the density of the defect level calculated by application of equation (8a,d) : $n_R = p_{\max} - p_{\min}$, is equal in the recovery stages corresponding to the curves 3 and 4. Taking together these results, it is suggested that n_R is a constant during the whole recovery procedure. Building on this assumption, also for the curves 1 and 2 p_{\min} is then known by equation (8a,d) : $p_{\min} = p_{\max} - n_R$. Since for the situation corresponding to curve 1, p_{\max} is small and in fact $p_{\max} < n_R$, a negative p_{\min} is calculated. For $p_{\min} < 0$ the actually observed Fermi level pinning is prescribed by the model discussed in section 3.4.3. For curve 2 the equalities $p_{\max} = n_R$ and $p_{\min} = 0$ approximately hold. In agreement herewith at low temperatures the Fermi level settles about halfway the valence band and the irradiation defect level. Knowing both p_{\max} and p_{\min} belonging to curves 1 and 2, the right hand side of equation (9a,d) may be calculated also for these stages. Again the result, as shown in figure 39, indicates an irradiation defect level given by $E_R = (0.23 \pm 0.03)$ eV.

In conclusion we note that the results of the measurements are consistent with the direct production by the irradiation of a defect level at $E_R = (0.23 \pm 0.03)$ eV. During the recovery treatment the concentration of this level does not change. Evidently this irradiation defect is not involved in the reaction: $\text{Li}^+ + \text{R} \rightarrow \text{LiR}$, and the defect R must be a different irradiation produced defect. The time dependence of the lithium precipitation process is governed by the time constant τ_{LiR} . As a consequence of the lithium precipitation the lithium concentration decreases, and both p_{\max} and p_{\min} increase, as follows from the equations (6a) and (7a), or (6d) and (7d). This time dependence of p_{\max} and p_{\min} fully accounts for the observed behaviour of the hole concentration as given in figure 37 and discussed in section 3.4.3.

In accordance with these conclusions our next considerations will be concerned with two irradiation defect types. With the first of these the electronic level at 0.23 eV above the valence band is associated. On the second defect, called R, lithium ions precipitate by the reaction $\text{Li}^+ + \text{R} \rightarrow \text{LiR}$. To avoid confusion it must be

remarked, that the symbol R, now specifically set apart for the second type of defect, was used in a looser sense in the preceding text, where it often referred to the total irradiation effect without further definition.

3.6.4 Defect level at 0.23 eV

Concerning this first type of irradiation defect the available information is presented in the tables XII and XIII. In table XII experimentally determined concentrations, called $n_{0.23}$, are stated, as well as their cross sections of introduction $\sigma_{0.23}$. Data from literature

TABLE XII
Introduction of 0.23 eV levels by ^{60}Co gamma irradiation.

| Sample | Irradiation temperature | Irradiation dose | $n_{0.23}$ | $\sigma_{0.23}$ |
|----------|-------------------------|--------------------------------|----------------------------|----------------------------|
| — | °C | 10^{14} γ/cm^2 | 10^{10} cm^{-3} | 10^{-4} cm^{-1} |
| W, 2, 7 | +40 | 36 | 90 | 2.5 |
| W, 2, 9 | 0 | 35 | 60 | 1.7 |
| TI, 2, 3 | +40 | 39 | 90 ± 15 | 2.3 ± 0.4 |

concerning irradiation defects with a detected level in the range (0.23 ± 0.05) eV are summarized in table XIII. By cross section or introduction rate is meant the concentration of defects divided by the incident radiation dose per unit area. This is the parameter of most physical significance, since at our low irradiation doses the concentration of introduced defects is expected to be proportional to the total dose. As illustrated by figure 34 a constant introduction rate was actually observed.

To start a discussion on the donor or acceptor character of the 0.23 eV level, we first note that to curve 1 of figure 37 a value $p_{\text{max}} \approx 10 \times 10^{10} \text{ cm}^{-3}$ belongs. From the tables XII and XIV it is seen that irradiation defect concentrations $n_{0.23}$ and n_{R} range from 60 to $200 \times 10^{10} \text{ cm}^{-3}$. Compared to relevant concentrations, the value of p_{max} , measured immediately after irradiation, is therefore small. For convenience sake we put $p_{\text{max}} = 0$ in the next discussion.

TABLE XIII

Summary of data on irradiation defects with a level in the range (0.23 ± 0.05) eV.

| Level position | Donor (D) or Acceptor (A) | Introduction rate | Type of radiation | Defect assignment | Reference |
|----------------|---------------------------|---------------------------|--------------------------|-----------------------------|-----------|
| eV | — | 10^{-4} cm^{-1} | — | — | — |
| 0.18 | D | | 0.7 MeV e | | 53 |
| 0.19 | | | 1 MeV e | | 54 |
| 0.21 | | | $^{60}\text{Co } \gamma$ | | 55 |
| 0.21 | D | | 1 MeV e | | 56 |
| 0.21 | D | 0.2–0.5 | $^{60}\text{Co } \gamma$ | centre including boron | 57 |
| 0.21 | | | 0.9 MeV e | | 58, 59 |
| 0.23 | | 0.6 | $^{60}\text{Co } \gamma$ | | 60 |
| 0.23 | A | 9 | $^{60}\text{Co } \gamma$ | lithium-vacancy complex | 61 |
| 0.25 | D | | 1.5 MeV e | divacancy | 62 |
| 0.27 | D | 2 | $^{60}\text{Co } \gamma$ | divacancy | 55 |
| 0.27 | | | 1 MeV e | | 63 |
| 0.27 | D | | 1 MeV e | oxygen-interstitial complex | 56 |
| 0.27 | | | 0.5 MeV e | | 53 |
| 0.28 | D | 0.1 | $^{60}\text{Co } \gamma$ | divacancy | 57 |
| 0.28 | | | 0.9 MeV e | | 58, 59 |

Considering first the acceptor case the above statement leads to:

$$p_{\max} = n_{\text{B}} + n_{0.23} - n_{\text{Li}} = 0,$$

or $n_{\text{B}} + n_{0.23} = n_{\text{Li}}$ immediately after irradiation. This is to be compared with the conditions before irradiation, when in the well compensated samples $n_{\text{B}} = n_{\text{Li}}$. A simple model which explains these results is ready at hand. In this model boron acceptor levels are converted into 0.23 eV acceptor levels by the irradiation, while the lithium concentration remains unchanged. From experiments reported in the sections 3.5.2 and 3.5.3 we however do know that primary irradiation defects interact with lithium ions. In conclusion, the explanation given above does not hold and the 0.23 eV defect is probably not an acceptor.

By arguing the same way for the case of a donor type

irradiation defect level we obtain:

$$p_{\max} = n_{\text{B}} - n_{\text{Li}} = 0,$$

or $n_{\text{B}} = n_{\text{Li}}$, both before and after the irradiation. If we assume the cross section for capture of a primary defect by boron and lithium ions to be nearly equal, this result follows at once. It guides us to propose a model in which boron plus a captured primary defect gives rise to the 0.23 eV donor level, whereas the lithium ion by capture of the primary defect is converted into a neutral atom. Some comments to elucidate this particular choice of model are still to be made.

By assigning the 0.23 eV defect level to a complex including boron agreement is established with results obtained by SONDER and TEMPLETON⁵⁷. Equal removal rate of B⁻-acceptors and Li⁺-donors is plausible if these centres are eliminated by vacancy capture. In the present case vacancies are neutral since the Fermi level is near midgap. No Coulomb attraction therefore exists between the interacting species and comparable capture radii of 4 to 5×10^{-8} cm may be anticipated for both processes. If lithium and boron removal is effected by capture of interstitials, for which no level scheme is known, these also have to be neutral. Nearly the same amount of 0.23 eV levels is created in the Wacker and Texas Instruments samples. But it is known that the Texas Instruments silicon is strongly contaminated with oxygen. In these samples less vacancies will be available for capture by Li⁺ and B⁻, since there is a severe competition for vacancies by oxygen atoms for the A-centre formation. This argument favours the assumption that an interstitial silicon atom is captured. Some authors^{56,64} propose the existence of stable oxygen-interstitial pairs; it invalidates our present reasoning and raises new questions if they are right. The somewhat lesser defect production rate in sample Wacker, 2, 9, compared to sample Wacker, 2, 7, is justified by the difference in irradiation temperature and is in quantitative agreement with results of DJERASSI, MERLO-FLORES and MESSIER⁵⁵. This temperature dependence, also apparent in table XIV, is associated with the probability of escape of vacancies and interstitials from a close pair, for which a quantitative model has been developed by WERTHEIM⁶⁵, and MACKAY and KLONTZ⁶⁶. Observation of this temperature dependence lends support to the efforts of explaining results in terms of vacancies and interstitials. The assumption of the neutral state of the proposed

lithium-interstitial complex is in agreement with the results given in section 3.5.2 for strongly lithium doped samples. No clear indication of new donor or acceptor levels was obtained in these experiments. A rather high yield of defects is measured since the cross section $\sigma_{0.23}$ is about $2.5 \times 10^{-4} \text{ cm}^{-1}$, and, according to our model, the same number of unobserved complexes including lithium is created. The largest cross section for ^{60}Co irradiation defect formation, $10 \times 10^{-4} \text{ cm}^{-1}$ at 40°C , was reported by SONDER and TEMPLETON⁶⁷ for quartz crucible grown oxygen containing silicon. Our results demonstrate that the greater part of the created interstitials has been captured by boron and lithium ions, and that their major irradiation effect thus has been measured. The role of vacancies, still available in equal amount, in producing precipitation centres, is discussed in the next section. In Wacker samples pairing between lithium and boron ions takes place to a considerable extent. It is credible that this process is immaterial to the present discussion, since lithium and boron concentrations remain equal. In Texas Instruments samples, however, lithium ions are specifically removed by LiO^+ -formation. To take this effect into account our previous assumption on the equal trapping cross section of interstitials by lithium and boron has to be generalized to include also the LiO^+ complex. One is inclined to the belief that interstitial silicon atoms may be captured by many impurities having all about the same capture radius. In view of the substantial body of experimental information available on defects with a level near 0.23 eV, reviewed in table XIII, the ambiguity in the foregoing discussion is rather disappointing. In our opinion it would be most helpful if by improving the accuracy of measurements and their analysis, the spectral resolution could be raised by one order of magnitude.

3.6.5 Defect R

Starting a discussion on the defect R it must be reminded that at the end of section 3.6.1 some properties of this defect were already deduced. From the value of the capture radius for trapping of lithium ions, except for the case of Wacker silicon, it followed that R is a neutral defect, if the Fermi level is near the middle of the gap. Measurements of the temperature dependence of the hole concentration revealed no level associated with the defect R located in the

lower half of the gap. Also the reaction product LiR is likely to be neutral and no level corresponding to it was detected. Since both species, R and LiR, are therefore invisible, their presence is only established indirectly via the loss of positive lithium ions.

To facilitate a further discussion all available data concerning the defect introduction rate are collected in table XIV. The striking difference in defect production for room temperature and liquid nitrogen temperature irradiations was mentioned and commented upon in the previous section. There is also a difference to be noted

TABLE XIV

Introduction of precipitation centres by gamma irradiation, determined by junction capacity (cap) or conductivity (cond) measurements. Sample M, 7, 13 is irradiated by ^{137}Cs gamma rays.

| Sample | Irradiation temperature | Irradiation dose | n_{LiR} | σ_{LiR} | Method of measurement |
|-----------|-------------------------|---------------------------------------|---------------------------|---------------------------|-----------------------|
| — | °C | $10^{14} \text{ } \gamma/\text{cm}^2$ | 10^{10} cm^{-3} | 10^{-4} cm^{-1} | — |
| M, 7, 11 | + 40 | 10.5 | 70 | 6.6 | cap |
| M, 7, 14 | + 40 | 3.3 | 20 | 6.1 | cap |
| TI, 1, 11 | + 40 | 25.5 | 100 | 3.9 | cap |
| TI, 2, 6 | + 40 | 19.5 | 80 | 4.1 | cap |
| TI, 2, 3 | + 40 | 38.6 | 130 | 3.4 | cond |
| W, 2, 5 | + 40 | 9.3 | 80 | 8.6 | cap |
| W, 2, 7 | + 40 | 35.7 | 220 | 6.2 | cond |
| W, 2, 9 | 0 | 35.3 | 140 | 4.0 | cond |
| M, 7, 12 | -196 | 23.9 | 70 | 2.9 | cap |
| TI, 1, 4 | -196 | 22.9 | 40 | 1.8 | cap |
| TI, 2, 1 | -196 | 23.9 | 29 | 1.2 | cap |
| W, 2, 3 | -196 | 24.2 | 27 | 1.1 | cap |
| M, 7, 13 | -196 | 138 | 6.4 | 0.04 | cap |

in the defect yield in identical slices. Such an ununderstood effect, also observed by other experimenters⁵⁵, forces one to be cautious and prohibits any analysis based on subtle variations. Concerning the Texas Instruments slices no choice is left, since these samples contain a dominating amount of oxygen. This impurity is known to capture a vacancy, creating a substitutional oxygen atom, the so-called A-centre, with an acceptor level at $E_{\text{C}} - 0.16 \text{ eV}$. A correlated loss of lithium donors and A-centre acceptor levels was observed in pulled crystals by VAVILOV and co-workers^{59, 68}. This interaction, $\text{Li}^+ + \text{O}_{\text{subst}} \rightarrow \text{LiO}_{\text{subst}}$, also explains our results. So

there is little doubt that, in the case of Texas Instruments crystals, the precipitation centre R has to be identified with the substitutional oxygen atom. In Merck slices the impurity oxygen is present in much lower concentration. Nevertheless the phenomenon of lithium precipitation takes place to a comparable extent. Clearly also precipitation centres are created by the capture of a vacancy by boron or lithium ions. It is not possible on the basis of the available information to express any preference for one of these impurities to be involved in this process. The Wacker silicon is rather exceptional, since only in these samples a large capture radius, equal to the Coulomb capture radius, was observed. This indicates the presence of negatively charged precipitation centres, which by electrostatic forces attract a lithium ion over a larger distance. It is tempting to attribute the exceptional behaviour of the Wacker samples to the lithium-boron complex, only present in this lowest resistivity silicon. Indeed, REISS, FULLER and MORIN³³ attach acceptor character to the LiB complex after capture of a vacancy. However, if this explanation holds, one would expect the observation of the large capture radius in all Wacker samples, which was actually not the case. The slightly larger negative defect yield in the samples Wacker, 2, 5 and Wacker, 2, 7 also reflects the existence of the negatively charged precipitation centre. On summarizing, gamma irradiation produces a variety of defects, neutral or negatively charged, on which lithium ions precipitate. The introduced amount of precipitation centres is larger, although not twice as large, as the amount of 0.23 eV defects. This again proves that the absorption of the major fraction of the vacancies has been observed. In all these discussions no mention has been made of dislocations, which possibly act as a sink for vacancies and interstitial atoms. If these processes happen a higher defect yield is expected for the dislocation poor materials, where the smallest number of primary defects is lost. Since such a dependence was not observed, dislocations, at the densities as occurring in our crystals, are considered as being of no importance.

3.7 Application to lithium drifted junction detectors

As was shown in previous discussions, ⁶⁰Co gamma irradiation of lithium drifted p-i-n junctions produces negative space charge in

the lithium compensated intrinsic region. Mainly responsible for this creation of space charge is the loss of positive lithium ions, which precipitate on irradiation defects, thereby becoming neutral atoms. Some of the junction characteristics undergo important changes by the conversion of the p^+i-n^+ junction into a p^+p-n^+ junction. After irradiation the potential distribution $\varphi(x)$ is a quadratic function of position x , with positive curvature, while the electric field depends linearly on x . Potential probe measurements, described in section 3.3.4, showed these variations which result in slower detector pulses of modified shape. The junction capacity for low reverse voltages increases by irradiation. As demonstrated by the experiments discussed in section 3.3.2, below a certain marginal value the capacity C depends inversely proportional on the square root of the reverse bias V . Increased junction capacity, also therefore increased amplifier input capacity, deteriorates resolving power of the detection system. Corresponding with an increased capacity the depleted junction width decreases by irradiation. For low reverse voltages an insensitive region develops adjacent to the p^+ -type region. Its direct consequences on particle detection, decreasing pulse heights and introducing statistical broadening, is shown by the experiments reported on in section 3.3.5. All of these effects adversely affect the operation of a junction as particle detector.

It turned out that the total amount of precipitation centres introduced by the irradiation hardly depends on the impurity content of the crystals. Clearly in all cases the primary defects are absorbed by impurities, creating precipitation centres, of which a diversity exists. The introduction rate σ , 5×10^{-4} to 10^{-3} cm^{-1} at room temperature, is about 3 times higher than at the boiling point of liquid nitrogen.

Lithium drifted junctions possess self-healing properties, which counteract the above-mentioned deterioration of detector performance. The lithium ion drift mechanism tends to restore the space charge compensation in the initial intrinsic region. By this process no anneal in carrier lifetime is necessarily effected. In a reverse-biased junction in a steady irradiation flux equilibrium conditions will develop. If the incident intensity, photons per unit time and unit area, is ϕ , and the introduction rate of precipitation

centres is σ , then the equation:

$$\frac{dn_R}{dt} = \sigma\phi,$$

expresses the generation of a net ionized defect density n_R . For the lithium drift compensation mechanism it is known that:

$$\frac{dn_R}{dt} = -\frac{\alpha n_R}{\tau_C},$$

where the time constant τ_C is the ionic relaxation time, introduced and discussed in sections 1.6.3 and 3.6.2. The factor α , which is the fraction of free lithium ions, is smaller than one, if too much boron or oxygen is present in the crystals. Under steady state conditions space charge generation and compensation will be equal. Thus:

$$n_R = \frac{\sigma\phi\tau_C}{\alpha} = \frac{\sigma\phi\epsilon}{\alpha n_{Li}e\mu_{Li}}.$$

On the other hand we quote from the discussion in section 3.3.2:

$$n_R = \frac{2C_m^2 V_m}{e\epsilon A^2} = \frac{2eV_m}{eW_m^2}.$$

Equating the right hand side expressions we obtain:

$$V_m = \frac{\sigma\phi W_m^2}{2\alpha n_{Li}\mu_{Li}},$$

for the value V_m above which the p⁺-p-n⁺ junction is still depleted to the maximum width W_m . Full depletion of the junction ensures complete collection of ionized carriers, a lowest capacity and no insensitive layers. Imposing this as the only criterion the junction may be operated at a bias V_m under a steady irradiation of intensity ϕ , given by:

$$\phi = \frac{2\alpha n_{Li}\mu_{Li}V_m}{\sigma W_m^2}.$$

For example, if $V_m = 100$ V, $\alpha = 1$, $n_{Li} = 10^{14}$ cm⁻³ (starting from 100 Ω cm p-type silicon), $\mu_{Li} = 5 \times 10^{-13}$ cm²/Vs (at 20 °C), $W_m = 1$ mm, and $\sigma = 10^{-3}$ cm⁻¹ the allowed radiation intensity is $\phi = 10^9$ γ /cm²s, corresponding to 0.6 Röntgen/second of ⁶⁰Co

radiation. The above formula indicates that a radiation resistant detector should be thin, operated at high bias and temperature, and made of low resistivity silicon. Concerning the latter factor it is to be kept in mind that in low resistivity silicon, containing much boron, the effect of $\text{Li}^+\text{-B}^-$ ion pairing, which decreases α , becomes of importance. In the extreme of highly doped silicon α is given by $\alpha = (K/n_{\text{Li}})^{\frac{1}{2}}$, where K is the equilibrium constant of the pairing reaction. In this case the allowed radiation flux is calculated from:

$$\phi = \frac{2(Kn_{\text{Li}})^{\frac{1}{2}}\mu_{\text{Li}}V_{\text{m}}}{\sigma W_{\text{m}}^2}.$$

APPENDIX

TREATMENT OF P-N JUNCTION WITH COMPLEMENTARY ERROR FUNCTION IMPURITY DISTRIBUTION

In paragraph 1.6 expressions were derived for the capacity of a p-n junction and also for the lithium ion drift rate in such a junction. All these derivations were based on the assumption that the impurity concentration in the junction region is adequately represented by a line arfunction. In this Appendix we leave out this assumption and base our calculations on a complementary error function distribution, which after the applied diffusion procedure is expected to hold.

A.1 p-n Junction capacity

As before the lithium concentration is given by

$$n_{\text{Li}}(x) = n_{\text{Li}}(0) \operatorname{erfc} \frac{x}{2(D_{\text{Li}}t)^{\frac{1}{2}}}.$$

The quantity $2(D_{\text{Li}}t)^{\frac{1}{2}}$ is a characteristic length involved in all diffusion problems. It will prove to be convenient to introduce a dimensionless reduced length by defining:

$$\xi \equiv \frac{x}{2(D_{\text{Li}}t)^{\frac{1}{2}}}.$$

The net acceptor concentration $n_{\text{a}} - n_{\text{d}}$ is assumed to be constant in the junction region. A p-n junction is formed at $x = c$, or, in reduced units, at $\xi = \gamma$, where $\gamma = c/2(D_{\text{Li}}t)^{\frac{1}{2}}$. The value of γ is found from:

$$n_{\text{a}} - n_{\text{d}} = n_{\text{Li}}(c) = n_{\text{Li}}(0) \operatorname{erfc} \gamma$$

The space charge ρ , set up by positive donors and negative acceptors is given by:

$$\rho(\xi) = en_{\text{Li}}(0)(\operatorname{erfc} \xi - \operatorname{erfc} \gamma).$$

Substitution into the Poisson equation yields:

$$\frac{d^2\varphi}{dx^2} = -\frac{dE}{dx} = -\frac{en_{Li}(0)(\operatorname{erfc} \xi - \operatorname{erfc} \gamma)}{\epsilon}.$$

Integration of this equation yields an expression for the electric field E . At the boundaries of the depleted junction width the electric field is zero. Therefore $E(\xi_1) = E(\xi_2) = 0$, where ξ_1 and ξ_2 represent begin and end position of the junction width respectively. Carrying out the above integration, then after minor rearrangements this condition is formulated by $f(\xi_1) = f(\xi_2)$, where

$$f(\xi) = \xi \operatorname{erfc} \gamma - \xi \operatorname{erfc} \xi + \frac{1}{\sqrt{\pi}} \exp(-\xi^2).$$

After series expansion one finds:

$$\xi_2 - \gamma = -(\xi_1 - \gamma) + \frac{2\gamma}{3} (\xi_1 - \gamma)^2 - \frac{4\gamma^2}{9} (\xi_1 - \gamma)^3 \dots$$

Essentially the condition $f(\xi_1) = f(\xi_2)$ expresses the equality of total space charge in both sides of the junction. A second integration, an integration of the electric field over the junction width, yields the reverse voltage V for a junction extending from ξ_1 to ξ_2 . The result is:

$$V = \frac{en_{Li}(0)D_{Li}t}{\epsilon} \{2\xi_2 f(\xi_2) + \operatorname{erfc} \xi_2 - 2\xi_1 f(\xi_1) - \operatorname{erfc} \xi_1\}.$$

Again, after series expansion this reads as:

$$V = \frac{en_{Li}(0)D_{Li}t}{\epsilon} \frac{2}{\sqrt{\pi}} \exp(-\gamma^2) \frac{1}{3} (\xi_2 - \xi_1)^3 \left\{ 1 - \frac{4\gamma^2 + 3}{60} (\xi_2 - \xi_1)^2 \dots \right\}.$$

A practical procedure is now the following. Choose a value ξ_1 and calculate $f(\xi_1)$. Find another ξ , called ξ_2 , with $f(\xi_2) = f(\xi_1)$. The search for an approximate ξ_2 is facilitated by making a graph of $f(\xi)$, which looks like a distorted parabola, with a minimum for $\xi = \gamma$. After ξ_2 has been found the junction width $W = 2(D_{Li}t)^{\frac{1}{2}}(\xi_2 - \xi_1)$ is known and also the reverse voltage V may be calculated. In this way, starting from a suitable series of ξ_1 -values, a whole $W-V$, or $C-V$, curve may be constructed.

The results of such calculations show that for high V the capacity

indeed deviates from the $V^{-1/3}$ power law. However, even for a junction width equal to L , where the linear junction approximation is certainly of doubtful nature, the deviation is small. It is therefore concluded that the slower increase of junction width on the n-type side of the junction, accidentally is compensated very well by the faster increase in the p-type side. Figure A1 shows some results calculated for our standard diffusion conditions in $100 \Omega\text{cm}$ silicon. The main variation of the junction capacity according to $V^{-1/3}$ is eliminated by plotting $CV^{1/3}$ on the vertical scale. This was done in order to be able to present in a pronounced way the special features characteristic for the complementary error function distribution. In spite of the small difference between the calculated curves the tendency of the experimental curve to follow the complementary error function calculations is evident.

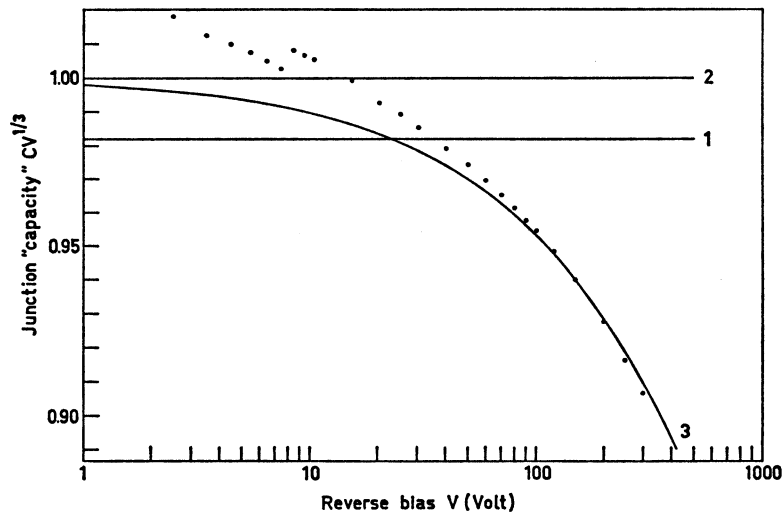


Fig. A1. Capacity of p-n junction as function of reverse voltage. Vertical axis in arbitrary units. Curve 1: According to linear junction approximation, using L . Curve 2: According to linear junction approximation, using L^* . Curve 3: According to complementary error function distribution. \bullet : Experimental points measured on sample Texas Instruments, 1, 11.

For the low values of reverse bias only the first term in the approximate formula for V needs to be considered and one obtains:

$$V = \frac{2en_{\text{Li}}(0)D_{\text{Li}}t}{3\epsilon\sqrt{\pi}} \exp(-\gamma^2)(\xi_2 - \xi_1)^3.$$

It follows then that the formula given in section 1.6.2 remains valid, except for a replacement of L by another quantity of dimension length L^* . From a comparison of both formulae it is seen that the latter is given by:

$$L^* = (\pi D_{Li} t)^{\frac{1}{2}} \exp(\gamma^2) \operatorname{erfc} \gamma.$$

L^* and L are related by:

$$L^* = L\sqrt{\pi} \gamma \exp(\gamma^2) \operatorname{erfc} \gamma.$$

Using the asymptotic series expansion for $\operatorname{erfc} \gamma$, retaining only the first two terms of it, one obtains:

$$L^* \approx L \left(1 - \frac{1}{2\gamma^2} \right).$$

In our circumstances the difference between L^* and L amounts to about 10 %.

A.2 Lithium drift

After application of a reverse bias the junction width will increase because of space charge neutralization in the drift region. During the drift process the total space charge in the depleted junction region remains zero, and also there is no change in the voltage across the junction. From these two conditions one derives an expression for the initial rate of junction width increase. The factor giving the space charge compensation is found by applying the continuity equation:

$$\left(\frac{d\rho(x)}{dt} \right)_{t=0} + \left\{ \frac{d}{dx} \left(n_{Li}(x) e \mu_{Li} E(x) \right) \right\}_{t=0} = 0$$

A contribution to the ionic current arising from diffusion is neglected. The formula at which one arrives contains integrals of the type $\int \xi (\operatorname{erfc} \xi)^2 d\xi$ and similar ones, which by partial integration may be reduced to a sum of complementary error functions and its derivative $-2 \exp(-\xi^2)/\sqrt{\pi}$. After straightforward but tedious calculations the result finally reads:

$$\left(\frac{d \ln C}{dt} \right)_{t=0} = - \left(\frac{d \ln W}{dt} \right)_{t=0} = - \frac{P}{3\tau_C}.$$

$$P = \frac{3(\operatorname{erfc} \xi_1 - \operatorname{erfc} \xi_2) \{2\xi_2 f(\xi_2) + \operatorname{erfc} \xi_2 - 2\xi_1 f(\xi_1) - \operatorname{erfc} \xi_1\}}{4(\xi_2 - \xi_1)^2 (\operatorname{erfc} \xi_1 - \operatorname{erfc} \gamma) (\operatorname{erfc} \gamma - \operatorname{erfc} \xi_2)}$$

Series expansion yields:

$$P = 1 + \frac{4\gamma^2 + 3}{90} (\xi_2 - \xi_1)^2 - \frac{20\gamma^4 + 3\gamma^2 - 216}{5670} (\xi_2 - \xi_1)^4 \dots$$

Comparing with the corresponding formula of section 1.6.3 one infers that the factor P accounts for the modifications introduced by the complementary error function distribution.

Actual calculations of this drift rate factor P were made using existing tables of the complementary error function and its derivative²⁵. In figure A2 a plot of P as function of bias V is given for two values of the resistivity. One observes that P deviates only slightly from unity, especially of course for low reverse voltage. Again the linear junction approximation is surprisingly good and may be used without causing substantial errors.

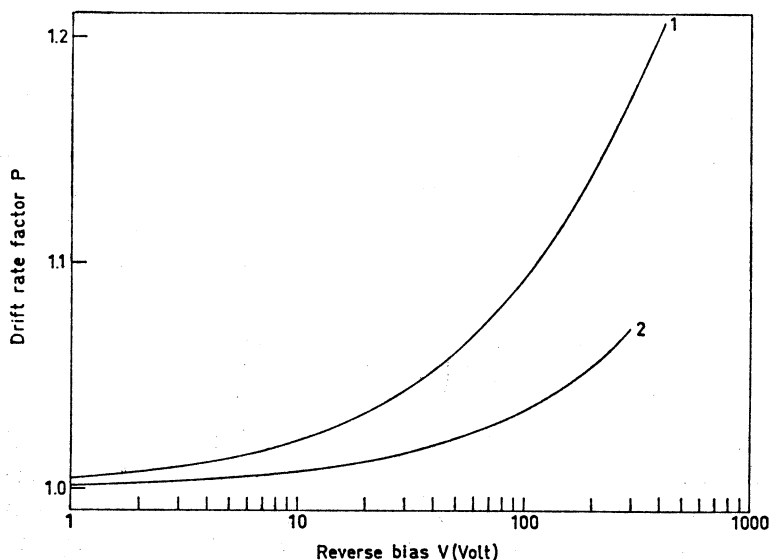


Fig. A2. Factor P of the lithium ion drift rate expression as function of reverse voltage. Curve 1: $n_{L1}(c) = 1.25 \times 10^{14} \text{ cm}^{-3}$, $\rho \approx 100 \text{ } \Omega\text{cm}$. Curve 2: $n_{L1}(c) = 5 \times 10^{14} \text{ cm}^{-3}$, $\rho \approx 25 \text{ } \Omega\text{cm}$.

SUMMARY

Chapter 1 is a survey of all experiments, performed to examine the impurity content of silicon crystals. Dislocation densities are determined by counting the etch pit density on preferentially etched crystal surfaces. Hall effect and resistivity measurements, based on the Van der Pauw theorem, are carried out using accurate equipment and careful measuring techniques. Analysis of the results by a donor-acceptor model also yields the concentration of the compensating dopant. Thus a powerful method is developed for future research on irradiation effects. Crystals from one of the "Lopex" batches turned out to be strongly compensated. The absorption of infrared radiation near $9 \mu\text{m}$ revealed oxygen contamination in "Lopex" silicon, correcting current views on this matter. A treatment is given of lithium diffused p-n junctions by dealing with the sheet resistance of the n-type layer, the junction capacity and lithium ion drift in the junction region. Formulae, which are exactly valid for the actual complementary error function impurity distribution, are derived in the Appendix. The improvement of the latter results over the usual linear approximation is demonstrated by capacity measurements. Lithium drift rate was exploited to investigate lithium-impurity reactions. The presence of oxygen in "Lopex" crystals is confirmed by a reduced drift rate. Studies were made of the time constants involved in the pairing reactions between Li^+ and O or B^- . A capture radius of about 5×10^{-8} cm is associated with the Li^+ -O interaction. Results obtained by Spitzer and Waldner for the equilibrium constant of the reaction $\text{Li}^+ + \text{B}^- \rightleftharpoons \text{LiB}$ were found to be inapplicable. In conclusion the method of preparation of lithium drifted p-i-n junctions is summarized.

Chapter 2. Reverse-biased p-i-n junctions are used as solid state ionization chambers for the detection of protons, deuterons and α -particles in the range from 5 to 50 MeV. Pulse heights are proportional to the particle energy. An analysis, for particles incident on

the p-type surface of a junction, shows that the pulse shape is exclusively determined by the particle range. Theoretical pulse shapes, given in mathematical and graphical form, are confirmed by experimental recordings. A particle identification system, based on the available information on energy and range, is described. Results of experiments are given, and are shown to compare quite nicely with a theoretical analysis. Separation between deuterons and α -particles above 8 MeV is demonstrated, but at about 22 MeV the curves representing the distinct particle types do intersect. Experiments with particles incident on the n-type side of a detector are of great significance, since a theoretical analysis forecasts considerable improvement of separation performance for this case.

Chapter 3. In an introduction some general aspects of irradiation effects in silicon, stressing the role of impurities, are discussed. Space charge creation by a gamma irradiation increases the capacity of reverse-biased junctions. The uniform concentration of charged defects is calculated from the low voltage branch of the capacity curve, where $C \sim V^{-1/2}$. As demonstrated by potential probe measurements, the linear potential distribution is changed by the irradiation into a quadratic one with positive curvature. Detection of α -particles from radioactive sources and of 26 MeV deuterons and 52 MeV α -particles from a cyclotron show a decreased depleted junction width. These observations also confirm the negative sign of irradiation produced space charge. Isolated lithium compensated silicon is converted by irradiation into extrinsic p-type silicon. The annealing behaviour is described by two time constants τ_C and τ_{LiR} . The time constant τ_C is only observed in experiments with reverse-biased junctions and governs the rate of space charge neutralization by the lithium drift mechanism. A formula for τ_C is derived which is applicable for the compensation process in both p-n and p⁺-p-n⁺ junctions. The time constant τ_{LiR} is associated with precipitation of lithium ions on irradiation defects. In most cases the capture radius, $R_{capt} = (4 \pm 1) \times 10^{-8}$ cm, is consistent with an interaction lacking Coulomb attraction. Introduction cross sections near 10^{-3} cm⁻¹ at room temperature are about three times higher than at -196 °C, and prove that all primary defects are absorbed by impurities, hardly dependent on the impurity content of the silicon crystals. A defect level, located 0.23 eV above the valence band, is tentatively attributed to a boron-interstitial complex with donor character. No

interactions between this centre and lithium exist. The nature of the precipitation centres is not very well established; presumably there is a variety of such centres. Lithium donor removal, by interaction with electron irradiation produced primary defects, is demonstrated by some experiments with heavily lithium doped crystals.

SAMENVATTING

Hoofdstuk 1 bevat een overzicht van de experimenten waarmee het gehalte aan verontreinigingen van silicium kristallen werd onderzocht. Dislocatiedichtheden werden bepaald door de dichtheid van etsputten te tellen. Hall effect- en soortelijke weerstand-metingen werden uitgevoerd volgens een methode die berust op het Van der Pauw-theorema, met gebruikmaking van nauwkeurige apparatuur. Analyse van de meetgegevens op basis van een donor-acceptor model levert als resultaat ook de concentratie van de compenserende verontreinigingen. Op deze wijze is een waardevolle mogelijkheid geschapen voor toekomstige onderzoek van bestralingseffecten. Silicium van een der „Lopex” partijen bleek in sterke mate gecompenseerd te zijn. Metingen van de absorptie van infrarood-straling bij ongeveer 9 μm toonden de aanwezigheid aan van zuurstofverontreiniging in „Lopex” silicium, waardoor gangbare meningen hieromtrent dienen te worden herzien. Op de eigenschappen van door middel van lithium-diffusie vervaardigde p-n overgangen wordt nader ingegaan door een discussie van de oppervlakteweerstand van de n-type laag, de capaciteit van de overgang en drift van lithium ionen in het overgangsgebied. In de Appendix worden formules afgeleid die exacte geldigheid bezitten voor de in werkelijkheid bestaande verdeling van verontreinigingen volgens een complementaire waarschijnlijkheidsfunctie. De verbetering die deze formules geven ten opzichte van de gebruikelijke benadering met een constante gradiënt wordt aan de hand van capaciteitsmetingen aangetoond. Het lithium-drift proces werd benut om reacties tussen lithium en verontreinigingen te bestuderen. Een verlaagde driftsnelheid in „Lopex” kristallen bevestigt de aanwezigheid van zuurstof in dit materiaal. De tijdconstanten van de paar-vormende reacties tussen Li^+ -ionen en zuurstof of B^- -ionen werden in een aantal gevallen gemeten. Bij de Li^+ -O wisselwerking behoort een vangststraal van ongeveer 5×10^{-8} cm. Gegevens van Spitzer en

Waldner voor de evenwichtsconstante van de reactie $\text{Li}^+ + \text{B}^- \rightleftharpoons \text{LiB}$ blijken niet van toepassing te zijn. De methode voor de vervaardiging van p-i-n overgangen volgens de lithium-drift methode wordt ten slotte in het kort besproken.

Hoofdstuk 2. Van onder tegenspanning geschakelde p-i-n overgangen werd gebruik gemaakt voor de detectie van protonen, deutronen en α -deeltjes in het gebied van 5–50 MeV. De hoogte der spanningsstoot is evenredig met de energie-afgifte van het deeltje. Een analyse, voor deeltjes die op de p-type zijde van de overgang invallen, toont aan dat de vorm van de spanningsstoot volledig door de dracht van het deeltje wordt bepaald. Theoretische beschouwingen over de vorm van de spanningsstoot, waarvan de uitkomsten in mathematische en grafische gedaante worden gegeven, vinden bevestiging in enkele experimenteel verkregen resultaten. Een systeem wordt beschreven, dat uitgaande van de beschikbare informatie over dracht en energie, de aard van een deeltje vaststelt. De experimentele resultaten blijken zeer goed met een theoretische analyse overeen te stemmen. Boven 8 MeV worden deutronen en α -deeltjes van elkaar gescheiden, maar bij ongeveer 22 MeV is er een snijpunt van de krommen die de afzonderlijke soorten van deeltjes weergeven. Berekeningen voor het geval van deeltjes invallend op de n-type zijde van een overgang voorspellen een aanzienlijk verbeterd deeltjes-scheidend vermogen en benadrukken de wenselijkheid van een experimentele verificatie.

Hoofdstuk 3. In een inleidende bespreking van de algemene aspecten van stralingsbeschadiging in silicium wordt enige nadruk op de functie van verontreinigingen gelegd. De vorming van ruimtelading door een gamma bestraling doet de capaciteit van een onder tegenspanning staande overgang toenemen. De concentratie van de homogeen verdeelde geladen puntfouten is berekenbaar uit de capaciteit in het lage-spanningsgebied, waar $C \sim V^{-\frac{1}{2}}$. Metingen met een sonde geven aan dat het lineaire verloop van de potentiaal door de bestraling is gewijzigd in een kwadratisch verloop met positieve kromming. Door middel van detectie van α -deeltjes van radioactieve preparaten, en van 26 MeV deutronen en 52 MeV α -deeltjes van een cyclotron, wordt de verminderde dikte van een bestraalde overgang vastgesteld. Deze metingen bevestigen bovendien het negatieve teken der ruimtelading. Door bestraling wordt geïsoleerd, met lithium gecompenseerd, silicium omgezet in

extrinsiek p-type silicium. Twee tijdconstanten, τ_c en τ_{LiR} , beheersen het gedrag van het bestralingseffect tijdens een herstelbehandeling. De tijdconstante τ_c wordt uitsluitend waargenomen in experimenten met onder tegenspanning staande overgangen en beschrijft de snelheid van ruimteladingscompensatie door het lithium-drift mechanisme. Voor τ_c wordt een betrekking afgeleid die zowel voor compensatie-processen in p-n als in p⁺-p-n⁺ overgangen toepassing vindt. De tijdconstante τ_{LiR} hangt samen met precipitatie van lithium ionen op stralingsfouten. De vangstraal, $R_{capt} = (4 \pm 1) \times 10^{-8}$ cm, die voor de meeste gevallen wordt berekend, heeft de goede grootte voor een wisselwerking waarbij elektrische aantrekkingskrachten ontbreken. Werkzame doorsneden van ongeveer 10^{-3} cm⁻¹ bij kamertemperatuur zijn 3 tot 4 maal hoger dan bij -196 °C, en bewijzen dat alle gevormde primaire stralingsfouten door verontreinigingen zijn ingevangen, vrijwel onafhankelijk van de zuiverheid der silicium kristallen. Een electronentoestand, die 0.23 eV boven de valentieband ligt, wordt door bestraling ingevoerd. Voorgesteld wordt dit niveau het karakter van een donor toe te kennen en toe te schrijven aan een complex bestaande uit borium en interstitieel silicium. Wisselwerkingen tussen dit centrum en lithium blijken niet plaats te vinden. De aard van de precipitatiecentra kon niet in alle gevallen worden vastgesteld; waarschijnlijk is dat er een verscheidenheid van deze centra bestaat. Experimenten met preparaten die in sterke mate met lithium verontreinigd waren, toonden aan dat lithium donoren worden weggenomen door wisselwerking met de primaire stralingsfouten.

REFERENCES

1. C. A. J. AMMERLAAN and K. MULDER, Nucl. Instr. and Meth. **21** (1963) 97.
2. F. L. VOGEL, W. G. PFANN, H. E. COREY and E. E. THOMAS, Phys. Rev. **90** (1953) 489.
3. W. C. DASH, J. Appl. Phys. **27** (1956) 1193.
4. W. C. DASH, J. Appl. Phys. **30** (1959) 459.
5. E. SIRTIL and A. ADLER, Z. Metallk. **52** (1961) 529.
6. L. J. VAN DER PAUW, Philips Res. Repts. **13** (1958) 1.
7. R. BERMAN, J. C. F. BROCK and D. J. HUNTLEY, Cryogenics **4** (1964) 233.
8. E. H. PUTLEY, The Hall Effect and Related Phenomena, Butterworths, London, 1960.
9. R. A. SMITH, Semiconductors, Cambridge University Press, Cambridge, 1961.
10. W. R. RUNYAN, Silicon Semiconductor Technology, McGraw-Hill, New York, 1965.
11. H. J. VAN DAAL, W. F. KNIPPENBERG and J. D. WASSCHER, J. Phys. Chem. Solids, **24** (1963) 109.
12. F. J. MORIN and J. P. MAITA, Phys. Rev. **96** (1954) 28.
13. H. BROOKS, Advances in Electronics and Electron Physics, Vol. VII, Academic Press, New York, 1955.
14. C. ERGINSOY, Phys. Rev. **79** (1950) 1013.
15. W. KAISER, P. H. KECK and C. F. LANGE, Phys. Rev. **101** (1956) 1264.
16. H. J. HROSTOWSKI and R. H. KAISER, Phys. Rev. **107** (1957) 966.
17. H. J. HROSTOWSKI and B. J. ALDER, J. Chem. Phys. **33** (1960) 980.
18. W. KAISER and P. H. KECK, J. Appl. Phys. **28** (1957) 882.
19. L. B. VALDES, Proc. Inst. Radio Engrs. **42** (1954) 420.
20. F. M. SMITS, Bell System Tech. J. **37** (1958) 711.
21. G. BACKENSTOSS, Bell System Tech. J. **37** (1958) 699.
22. E. M. PELL, J. Appl. Phys. **31** (1960) 291.
23. J. W. MAYER, J. Appl. Phys. **33** (1962) 2894.
24. F. A. LEHRER and H. REISS, J. Appl. Phys. **33** (1962) 2353.
25. Tables of Probability Functions, Vol. I, Federal Works Agency, Work Projects Administration for the City of New York, 1941.
26. E. M. PELL, Phys. Rev. **119** (1960) 1222.
27. E. M. PELL, Phys. Rev. **119** (1960) 1014.
28. E. M. PELL, J. Appl. Phys. **32** (1961) 1048.
29. T. R. WAITE, J. Chem. Phys. **32** (1960) 21.
30. F. A. KRÖGER, The Chemistry of Imperfect Crystals, North-Holland Publishing Company, Amsterdam, 1964.
31. E. M. PELL, J. Appl. Phys. **31** (1960) 1675.
32. W. G. SPITZER and M. WALDNER, Phys. Rev. Letters **14** (1965) 223.
33. H. REISS, C. S. FULLER and F. J. MORIN, Bell System Tech. J. **35** (1956) 535.
34. P. A. TOVE and K. FALK, Nucl. Instr. and Meth. **12** (1961) 278, Nucl. Instr. and Meth. **29** (1964) 66.

35. C. A. J. AMMERLAAN, Extrait des Mémoires de la Société Royale des Sciences de Liège, **10** (1964) 211.
36. F. UDO, R. F. RUMPHORST and L. A. Ch. KOERTS, Nuclear Electronics II, I.A.E.A., Vienna, 1962.
37. G. D. WATKINS, J. Phys. Soc. Japan **18**, suppl. II (1963) 22.
38. G. D. WATKINS, Effets des Rayonnements sur les Semiconducteurs, p. 97, Dunod, Paris, 1965.
39. G. D. WATKINS, Colloque sur l'Action des Rayonnements sur les Composants à Semiconducteurs, Toulouse, 1967.
40. J. J. LOFERSKI and P. RAPPAPORT, Phys. Rev. **111** (1958) 432.
41. G. G. GEORGE and E. M. GUNNERSEN, Effets des Rayonnements sur les Semiconducteurs, p. 385, Dunod, Paris, 1965.
42. J. H. CAHN, J. Appl. Phys. **30** (1959) 1310.
43. O. JÄNTSCH, Solid-State Electronics **5** (1962) 249.
44. C. P. COCKSHOT and E. L. G. WILKINSON, Brit. J. Appl. Phys. **16** (1965) 45.
45. P. BARUCH, J. Appl. Phys. **32** (1961) 653.
46. J. W. MAYER, R. BARON and O. J. MARSH, Phys. Rev. **137** (1965) A286.
47. T. M. BUCK, Semiconductor Nuclear Particle Detectors, Publication 871, N.A.S.-N.R.C., 1961.
48. H. REISS and C. S. FULLER, J. Metals **8** (1956) 276.
49. M. V. SULLIVAN and J. H. EIGLER, J. Electrochem. Soc. **104** (1957) 226.
50. J. A. BURTON, Physica **20** (1954) 845.
F. J. MORIN, J. P. MAITA, R. G. SHULMAN and N. B. HANNAY, Minneapolis Meeting Am. Phys. Soc., June 1954.
51. G. FEHER, Phys. Rev. **114** (1959) 1219.
52. B. PRATT and F. FRIEDMAN, J. Appl. Phys. **37** (1966) 1893.
53. J. A. BAICKER, Phys. Rev. **129** (1963) 1174.
54. V. S. VAVILOV, G. N. GALKIN, V. M. MALOVETSKAYA and A. F. PLOTNIKOV, Fiz. Tverd. Tela **4** (1962) 1969, (English transl.: Soviet Phys.-Solid State **4** (1963) 1442).
55. H. DJERASSI, J. MERLO-FLORES and J. MESSIER, J. Appl. Phys. **37** (1966) 4510.
56. V. M. MALOVETSKAYA, G. N. GALKIN and V. S. VAVILOV, Fiz. Tverd. Tela **4** (1962) 1372, (English transl.: Soviet Phys.-Solid State **4** (1962) 1008).
57. E. SONDER and L. C. TEMPLETON, J. Appl. Phys. **36** (1965) 1811.
58. V. S. VAVILOV, V. A. CHAPNIN and I. V. SMIRNOVA, J. Phys. Soc. Japan **18**, suppl. III (1963) 236.
59. I. V. SMIRNOVA, V. A. CHAPNIN and V. S. VAVILOV, Fiz. Tverd. Tela **4** (1962) 3373, (English transl.: Soviet Phys.-Solid State **4** (1963) 2469).
60. N. A. VITOVSKII, T. V. MASHOVETS and S. M. RYVKIN, Fiz. Tverd. Tela **4** (1962) 2845, (English transl.: Soviet Phys.-Solid State **4** (1963) 2085).
61. M. PERSIN and N. B. URLI, Colloque sur l'Action des Rayonnements sur les Composants à Semiconducteurs, Toulouse, 1967.
62. G. D. WATKINS and J. W. CORBETT, Phys. Rev. **138** (1965) A543.
63. G. K. WERTHEIM, Phys. Rev. **110** (1958) 1272.
64. K. MATSUI and P. BARUCH, Colloque sur l'Action des Rayonnements sur les Composants à Semiconducteurs, Toulouse, 1967.
65. G. K. WERTHEIM, Phys. Rev. **115** (1959) 568.
66. J. W. MACKAY and E. E. KLONTZ, J. Appl. Phys. **30** (1959) 1269, Effets des Rayonnements sur les Semiconducteurs, p. 11, Dunod, Paris, 1965.
67. E. SONDER and L. C. TEMPLETON, J. Appl. Phys. **31** (1960) 1279.
68. V. S. VAVILOV, I. V. SMIRNOVA and V. A. CHAPNIN, Fiz. Tverd. Tela **4** (1962) 1128, (English transl.: Soviet Phys.-Solid State **4** (1962) 830).

SLOTWOORD - ACKNOWLEDGEMENTS

Het in dit proefschrift beschreven werk is uitgevoerd in het kader van het programma van de „Stichting voor Fundamenteel Onderzoek der Materie (F.O.M.)”, die geldelijke steun ontvangt van de „Nederlandse Organisatie voor Zuiver Wetenschappelijk Onderzoek (Z.W.O.)”.

Met het ontwikkelingswerk aan p-i-n overgangen, vervaardigd volgens de lithium-drift methode, werd begonnen op het „Instituut voor Kernfysisch Onderzoek”, op initiatief van Dr. L. A. Ch. KOERTS, met Drs. K. MULDER en J. JOOSTEN als kundige medewerkers. Ir. W. K. HOFKER en medewerkers van de Philips halfgeleider stralingsdetectoren-groep stonden ons vaak met raad en daad terzijde. In samenwerking met Dr. L. A. Ch. KOERTS en R. F. RUMPHORST werd het in hoofdstuk 2 vermelde onderzoek aan identificatie van deeltjes uitgevoerd. Van de zijde der directie, Prof. Dr. P. C. GUGELOT en in later stadium Prof. Dr. R. VAN LIESHOUT, bestond steeds stimulerende belangstelling.

De bestudering van stralingsbeschadigingseffecten, uitgevoerd op het „Natuurkundig Laboratorium van de Universiteit van Amsterdam”, zou zonder de bekwame en daadkrachtige medewerking van drs. J. P. WOERDMAN, J. J. GOEDBLOED, P. G. SCHIPPER en W. H. KOOL niet op deze wijze tot stand gekomen zijn. Voor bestralingen kon worden gebruik gemaakt van de op het „Antoni van Leeuwenhoekhuis” aanwezige ^{60}Co bron. Prof. Dr. K. BREUR en medewerkers van de afdeling radiotherapie verleenden daarbij steeds alle hulp. Electronenbestralingen en een ^{137}Cs gamma bestraling werden verricht op het „Instituut voor Toepassing van Atoomenergie in de Landbouw”. In overleg met Prof. Dr. N. J. TRAPPENIERS, directeur van het „Van der Waals-Laboratorium”, en Prof. Dr. H. GERDING, directeur van het „Anorganisch-Chemisch Laboratorium”, werden zuurstof concentratie-bepalingen met behulp van infrarood-absorptie in gewaardeerde samenwerking met Drs. R. VETTER en

Drs. R. ELST uitgevoerd. Voor enkele berekeningen werd van de rekenmachines X1 en X8 van het „Mathematisch Centrum” gebruik gemaakt. Voor de electron spin resonantie-metingen stelde Dr. H. W. DE WIJN apparatuur ter beschikking. Gedurende alle fasen van het werk is de adviserende en daadwerkelijke hulp van technische en administratieve staven van het „Natuurkundig Laboratorium” en het „Instituut voor Kernfysisch Onderzoek” van onmisbare betekenis geweest. Het immer gewaardeerde contact met collega’s werkzaam in beide laboratoria was van grote vormende waarde. Door bemiddeling van Dr. Ir. C. L. BEUKEN werd al het teken- en fotografisch werk voor de samenstelling van dit proefschrift op voortreffelijke wijze verzorgd door personeel van de N.V. „Provinciale Limburgse Electriciteits-Maatschappij”. Prof. Dr. F. A. MULLER, coreferent, heeft het manuscript van het proefschrift aan een critische beoordeling willen onderwerpen. Allen die op bovengenoemde wijze of anderszins tot de voltooiing van dit werk hebben bijgedragen zeg ik graag van harte dank.

Jegens mijn promotor Prof. Dr. G. DE VRIES gevoel ik mij zeer erkentelijk voor de steeds ondervonden vertrouwensvolle begeleiding, die tot in laatste instantie een voorspoedige ontwikkeling van het werk ten zeerste heeft bevorderd.

By timely and exhaustively making his know-how available to us, Dr. J. W. MAYER of “Hughes Research Laboratories” advanced very much the progress in our development of p-i-n junctions.

